Bend-Twist Coupling Effects in Wind Turbine Blades

Vladimir Fedorov
Department of Wind Energy
Technical University of Denmark
Kgs. Lyngby, Denmark

July 10, 2012

Preface

This thesis is submitted in partial fulfillment of the requirements for obtaining the degree of Ph.D. at the Technical University of Denmark. The Ph.D. project was carried out at the Department of Wind Energy during three years from 2008 to 2012 with a one year break when I was employed as a Research Assistant in the same department. The project was equivalently funded by the Department of Wind Energy, by Vestas Wind Systems A/S and by the Danish Energy Authority through the EFP-project titled "Anisotropic beam model for analysis and design of passive controlled wind turbine blades" with journal no. 33033-0075.

I would like to thank my main supervisor Associate Professor Christian Berggreen from the Department of Wind Energy for great help and support throughout the entire project. I would also like to thank my supervisor Professor Steen Krenk from the Department of Mechanical Engineering for the guidance and invaluable help in writing this thesis. Thanks to my supervisor Senior Scientist Kim Branner from the Department of Wind Energy for help with practical issues and to visiting Professor Leif Carlsson for help with writing this Thesis. Valuable advises from Peter Berring and Nicolai Dimitrov on testing and modeling of a wind turbine blade are appreciated. Great thanks also goes to Yusuke Hara – an exchange MSc student in the Department of Mechanical Engineering, who was actively involved in design of the test rig for composite beams.

I would like to thank all the MSc students, PhD students, Postdocs and colleagues from the Departments of Wind Energy and Mechanical Engineering for a very friendly environment.

Finally, I would like to thank my family. My sister and brother with their families and especially my parents, who support me in any situation. It helped me a lot and it would be much harder to go through the project without it.

Vladimir Fedorov
Kgs. Lyngby, Denmark
July 10, 2012

This page is intentionally left blank.

Summary

The present PhD Thesis is devoted to theoretical and practical aspects of implementation and evaluation of bend-twist elastic coupling in wind turbine blade structures.

Insight into the nature of the coupling governed by anisotropy of composite materials is given in the first chapter of the thesis. Potential benefits of application of the bend-twist coupling in modern large wind turbine blades for passive control and load mitigation are described there as well.

A pure experimental investigation on bend-twist coupling effects in a commercial wind turbine blade, modified as an attempt to implement bend-twist coupling to it, is presented in the second chapter. Advanced methods of load application and measurements on the coupled blade section response are utilized during the experimental investigation. The coupling effect is demonstrated as bending of the modified blade section in torsion.

A number of approaches to develop detailed 3D finite element models of the blade section implying utilization of different finite element configurations such as shell elements with and without nodal offsets or combination of shell and solid elements are considered in Chapter 3. Validation of the results against the experimental data demonstrated that only the models built of combination of shell and solid elements are able to accurately predict complex coupled blade section response. Development complexities and accuracies of the models built according to each approach are thoroughly discussed.

Chapter 4 concerns numerical and experimental investigations on uniform composite beams of constant open and closed cross-sections with bend-twist coupling. Different approaches for development of finite element models of the composite beams are discussed here. Validation of the developed models against the experimental data for uniform beams demonstrated very low accuracy of the finite element models built of shell elements with nodal offsets and high accuracy of

the models built of shell elements without nodal offsets. Warping of the beam cross-sections predicted by the FE models was successfully validated against the experimentally measured warping deformations.

Chapter 5 presents a simple bend-twist coupling analysis method developed for direct evaluation of bending and torsional stiffnesses as well as bend-twist coupling coefficient in beam structures by processing numerical results of highly detailed finite element models or experimental results obtained using digital image correlation technique. The method is successfully applied to the experimental and numerical results for the composite beams and variations of the stiffness and coupling parameters along the beams are obtained and discussed.

Chapter 6 is devoted to a numerical investigation on the limits of bend-twist coupling in the wind turbine blade structures. Four representative cross-sections of a commercial wind turbine blade are selected for the investigation. The results demonstrate a potential bend-twist coupling limit for a pure glass-fiber blade design. For a hybrid glass-carbon fiber blade design, the limit could be nearly twice higher.

General conclusions on the Thesis and recommendations for future work are presented in Chapter 7.

Resumé (in Danish)

Ph.d.-afhandlingen adresserer teoretiske og praktiske aspekter i forbindelse med implementering og evaluering af elastiske bøjnings-torsions-koblinger i vindmøllevinger.

En generel indføring i elastiske stivheds-koblinger styret af anisotropi i kompositmaterialer er givet i det første kapitel af afhandlingen. Potentielle fordele ved udnyttelse af bøjnings-torsions-koblinger i moderne store vindmøllevinger i forbindelse med passiv kontrol og belastningsstyring er ligeledes beskrevet i dette kapitel.

En ren eksperimentel undersøgelse af bøjning-torsions-koblings-effekter i en specielt modificeret kommerciel vindmøllevingesektion, er præsenteret i det andet kapitel. Avancerede eksperimentelle metoder til belastnings-påføring og målinger på den bøjnings-torsions-koblede vingesektionen er blevet udviklet som en del af den eksperimentelle undersøgelse. Koblingsopførslens virkning påvises ved hjælp af bøjnings- og torsions-belastning på den modificerede vingesektion.

Et antal metoder til at opbygge detaljerede 3D finite element modeller af vingesektioner med bøjnings-torsions-koblinger er i kapitel 3 blevet udviklet ved anvendelse af forskellige finite element typer såsom skalelementerne med og uden knudeforskydninger eller en kombination af skal- og solid-elementer. Validering af resultaterne fra disse modeller er udført imod det eksperimentelle data fra tests på ovennævnte vingesektion og viste, at kun de modeller opbygget med en kombination af skal- og solid-elementer er i stand til præcist at forudsige opførslen af komplekse bøjnings-torsions-koblede vingesektioner. Udviklingen, kompleksiteten og nøjagtighed af de opbyggede modeller bliver endvidere grundigt diskuteret.

Kapitel 4 vedrører numeriske og eksperimentelle undersøgelser på ensartede kompositbjælker med konstante åbne og lukkede tværsnit med ilagte bøjnings-torsions-koblinger. Forskellige tilgange til udvikling af finite element modeller af kompositbjælkerne diskuteres. Valideringen af de udviklede modeller imod eksperimentelle resultater fra tilsvarende tests på ensartede bøjnings-torsions-koblede

bjælker viste lav nøjagtigheden for finite element modeller bygget af kun skalelementer med knudeforskydnings-modifikationer og høj nøjagtighed for modeller bygget af skalelementer uden disse forskydningsmodifikationer. Vridning af bjælketværsnittet forudsagt af finite element modellerne blev succesfuldt valideret mod eksperimentelt målte vridningsdeformationer.

Kapitel 5 indeholder en enkel bøjnings-torsions-koblings analysemetode udviklet til direkte vurdering af bøjnings- og torsions-stivheder samt bøjning-torsions-koblingskoefficienter i bjælkekonstruktioner ved at behandle numeriske resultater fra detaljerede finite element modeller eller eksperimentelle resultater opnået ved hjælp af digital billedbehandling. Analysemetoden er blevet anvendt til at analysere de eksperimentelle og numeriske resultater for kompositbjælker, og variationer af beregnede stivheder og koblings-parametre langs bjælkerne bliver diskuteret.

Kapitel 6 er dedikeret en numerisk undersøgelse af mulighederne for indbygning af bøjning-torsions-koblinger i vindmøllevinge-strukturer. Fire repræsentative tværsnit fra kommercielle vindmøllevinge er blevet udvalgt til undersøgelsen. Resultaterne viser en potentiel bøjning-torsions-koblingsgrænse for et rent glasfiber vingedesign, mens for et hybrid glas-kulfiber vingedesign, kan grænsen være næsten dobbelt så stor.

Generelle konklusioner og anbefalinger for fremtidigt arbejde er præsenteret i kapitel 7.

Contents

Chapter 1

Introduction

1.1 Background

The global cumulative installed wind capacity demonstrated rapid, nearly exponential growth during the past decade according to the reports by the Global Wind Energy Council, GWEC (2011) and World Wind Energy Association, WWEA (2012). The fast growth is supported not only by a large number of installed new mills, but especially by increased power output of modern wind turbines. Increase in the wind turbine power outputs, at the same time, reduces the wind energy costs, which is one of the most important factors in wind energy production. Nowadays, very large wind turbines with nominal power of up to 6-7 MW are available on the market, with blades reaching 75 m in length. Yet, future wind turbines are aimed at even larger blades with lengths up to 120 m.

Modern large wind turbine blades are long slender structures mainly produced of high stiffness-to-weight ratio composite materials such as glass fiber or carbon fiber reinforced plastics (GFRP or CFRP) with e.g. epoxy or polyester as matrix, in combination with other materials like Polyvinyl chloride (PVC) foam, Polyvinylisobutyl ether (PVI) foam, Polymethacrylimide (PMI) foam or balsa wood, which are typically used as core material in sandwich components in the blades. Detailed overview and selection of the materials common for application to wind turbine blades are well covered by Brøndsted et al. (2005).

In industry, fiber reinforced composite materials are typically used in form of laminates, that is structures built up layer by layer out of single laminae. Thus, the overall structure of a modern wind turbine blade is built up layer by layer

and mechanical properties of the blade are fully determined by material properties of the laminae. Therefore, a lamina can be considered as a building block for composite structures and particularly for wind turbine blades.

1.1.1 Elastic couplings in composite materials

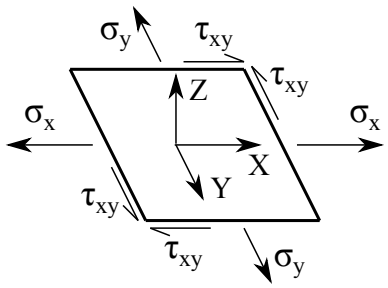

Figure 1.1: Stresses in a lamina

Consider a layer of fiber reinforced composite material - a lamina. It consists of combination of stiff fibers and relatively soft matrix material and thus generally possesses different mechanical properties in different directions. Generally, a fiber reinforced lamina can be with good approximation treated as an orthotropic material due to symmetry of its mechanical properties with respect to several directions. In a particular case, when all the fibers are directed equivalently (so-called unidirectional layer or lamina), the lamina can be well treated as transversely isotropic material.

Mechanical properties of a lamina are well described using the Classical Laminate Theory, see e.g. Jones (1999) or Zenkert and Battley (2006). The relation between the principle lamina in-plane stresses σ_x, σ_y and τ_{xy} and the corresponding strains ϵ_x, ϵ_y and γ_{xy} (Fig. 1.1) can be written in matrix form:

$$\begin{bmatrix} \sigma_x \\ \sigma_x \\ \tau_{xy} \end{bmatrix} = \begin{bmatrix} Q_{11} & Q_{12} & Q_{16} \\ Q_{12} & Q_{22} & Q_{26} \\ Q_{16} & Q_{26} & Q_{66} \end{bmatrix} \begin{bmatrix} \epsilon_x \\ \epsilon_x \\ \gamma_{xy} \end{bmatrix} \tag{1.1}$$

When the fibers are oriented so that they are parallel to one of the principal axes X or Y, elements Q_{16} and Q_{26} of the stiffness matrix (1.1) become zero. This situation corresponds to the shear stresses and strains being fully uncoupled from the two other principal stresses/strains in the lamina. In contrast, if the fibers are biased from the principal axes, the shear stresses and strains become coupled

to either stress σ_1 or σ_2 in the two principal directions or to both of them. For instance, when a composite plate with fibers biased from the longitudinal axis is pulled along one of the principal axes as it is shown in Fig. 1.2, it deformes not only by extension but also by shear deformation, which leads to side movement of the pulled edge, shown by the dashed arrow.

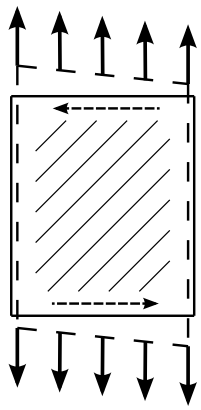

Figure 1.2: Coupled response of a composite plate with biased fibers

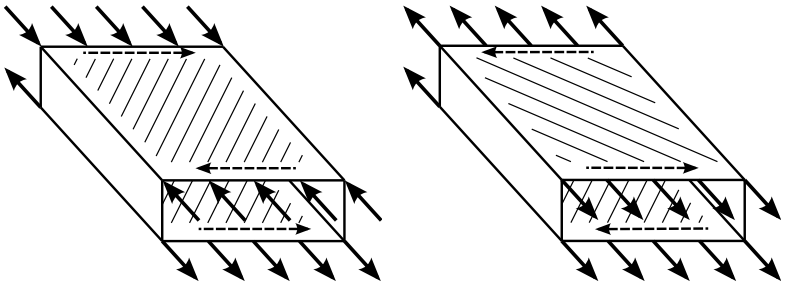

(a) Bend-twist coupling (b) Extension-twist coupling

Figure 1.3: Coupling mechanisms in composite beams.

By utilizing the orthotropic properties of composite fiber reinforced materials in a smart manner, it is thus possible to design components and structures with coupling effects similar to the one demonstrated for a lamina. Two well known examples of coupled beam designs are bend-twist coupled and extension-twist coupled beams, see Fig. 1.3. In the bend-twist coupled beam, the fibers in the horizontal walls (flanges) are offset in a symmetrical way, so that bending moment applied to the beam causes compression of the top flange and tension of the bottom flange. Following the lamina example, shear deformations of both flanges result in a twist response of the beam. By analogy, in the extension-twist coupled beam the fibers

are placed in an asymmetric manner, so that twist occurs when the beam is subject to tension load.

1.1.2 Bend-twist coupling in wind turbine blades

It is possible to utilize the described above coupling effects in wind turbine blades so that the blades, when loaded, deform in a desired coupled manner, and thus potentially improving the wind turbine performance and increasing its lifetime. In the present work the effects of only bend-twist coupling in wind turbine blades are studied. Introduction of bend-twist coupling into a wind turbine blade is basically aimed at two types of the coupled blade response under bending load: twist of the blade decreases its angle of attack (twist towards feather), see Fig. 1.4(a); and twist of the blade increases its angle of attack (twist towards stall), see Fig. 1.4(b).

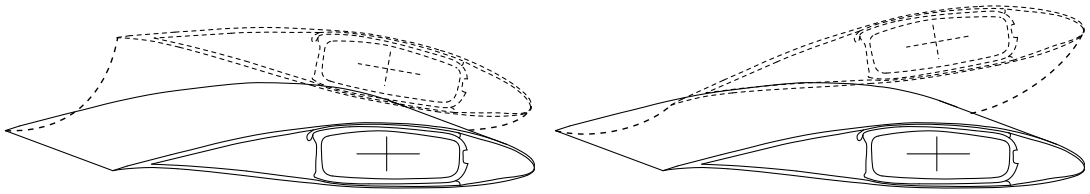

(a) Twist towards feather (b) Twist towards1 stall

Figure 1.4: Response of a bend-twist coupled wind turbine blade to bending load

It has been demonstrated that blades possessing bend-twist coupling can potentially improve the overall performance of a wind turbine by several means. Lobitz et al. (1996) showed that a stall controlled, fixed pitch system can be operated with a larger rotor to achieve net energy enhancements without increasing the maximum power rating. Though it was later found by Lobitz and Veers (2003) that this approach can suffer from flutter, substantial fatigue damage reductions were revealed in low wind speed conditions when adaptive coupled blades are used.

Lee and Flay (2000) demonstrated that large pitch angles (here correspond to blade twist angles), up to $30° - 40°$ at the coupled blade tip, are to be induced for full passive control of a 50kW wind turbine with blades twisting towards feather. Such large pitch angles can unlikely be achieved by using only bend-twist coupling effects. However, modeling of 9 m long coupled blades by Berry and Ashwill (2007) exposed limited load mitigation effect in case of a stall controlled wind turbine in

fixed-speed fixed-pitch operation (2.4-8.6%) but significant load reduction (20-30%) in a modern variable-speed variable-pitch operation mode.

Aeroelastic behavior of large MW-sized wind turbine blades was studied by Lobitz (2004) who demonstrated 12% flutter speed increase for the bend-twist coupled blades. Therefore, analysis of the bend-twist coupling effects in the wind turbine blades is an important problem for design of large bend-twist coupled blades.

A number of design codes are available nowadays for modeling of dynamic behavior of wind turbine blades, see e.g. Schepers et al. (2001), Rasmussen et al. (2003) and Buhl et al. (2006). In some of the codes the blade structure is described using multi-body formulation (e.g. ADAMS/WT) or using assumed deformation mode shapes (e.g. FLEX5). The codes based on the finite element method using beam elements (such as HAWC2) can account for coupled blade behavior by introducing the coupling effects into the beam formulation and thus analyze the performance of large wind turbines with coupled blades.

A wide overview and an assessment of beam models that are applicable for the analysis of wind turbine blades are given by Hodges (2006), Jung et al. (1999) and Volovoi et al. (2001). The models can be conventionally divided in to two groups: The beam models of the first group are purely analytical, involving certain assumptions and considerations regarding e.g. beam geometry or stress distributions; The beam models of the second group involve two-dimensional cross-sectional analysis using finite elements, see for instance VABS by Yu et al. (2002) or BECAS by Blasques and Lazarov (2011).

A somewhat different approach to create a beam finite element model for a wind turbine blade was developed by Malcolm and Laird (2003, 2007) and called the Beam Property Extraction method. Here the beam element stiffness matrices are recovered from global response of a blade subject to six unique load cases, generated by a detailed 3D finite element model of the blade. Later, Branner et al. (2007) made an attempt to apply this method to a section of a commercial wind turbine blade and to study the coupling effects in the blade structure.

1.2 Objectives

The main objective of the present study is to investigate the bend-twist coupling effects in composite beam-like structures and particularly in wind turbine blades. Magnitudes of the bend-twist coupling effects which are possible to achieve in

modern blades are of particular interest in this study. Investigations on the bend-twist coupling use both numerical and experimental methods.

In the numerical part of this study, performance of several finite element (FE) modeling techniques that allow for relatively easy and fast development of detailed FE models are thoroughly analyzed to select most suitable ones for investigations on the coupled response of composite beams and wind turbine blade structures. Particular attention is paid to the problem of inaccurate prediction of the torsional response by FE models consisting of shell elements with nodal offsets, highlighted by Laird et al. (2005) and Branner et al. (2007). The results of the experimental investigations to be performed on composite structures in the present study are to be used for validation of the numerical models.

1.3 Thesis overview

The Thesis is divided into seven chapters and includes several appendices.

Chapter 2: The chapter is devoted to a purely experimental study on the bend-twist coupling effects in a commercial wind turbine blade section which was modified in order to intensify its originally limited coupled response. The blade section is treated as a general composite non-homogeneous beam, which, however, requires a number of assumptions to simplify the experimental study.

Chapter 3: Problems in connection with development of detailed 3D FE models of modern wind turbine blades are discussed. Two FE models of the wind turbine blade section studied in Chapter 2 are considered. Comparison of the results of the FE models against each other and validation against the experimental data is presented.

Chapter 4: A set of detailed 3D FE models of uniform composite beams of simple geometry and layup is considered. For validation of the numerical models against the experimental results, a number of beams of open (I-shaped) and closed (box-shaped) cross-sections and possessing different levels of the bend-twist coupling effects are designed and manufactured. An advanced test setup, built to carry out experiments on the composite beam specimens is described.

Chapter 5: A simple method for analysis of bend-twist coupling effects in a general beam is presented. The advantages of the method, such as applicability to the experimental results obtained by using a digital image correlation system and to the results of detailed beam FE models are demonstrated.

Chapter 6: The effects of the modifications numerically introduced to the wind turbine blade section, considered in chapters 2 and 3, as an attempt to implement the bend-twist coupling effects in the blade structure, are studied. The bend-twist coupling magnitudes feasible to achieve by the considered modifications are presented by application of the developed simple bend-twist coupling analysis method.

Chapter 7: Conclusions and suggestions for considerations for future work are presented.

Appendix A: Detailed information on geometry and layup of the wind turbine blade section considered in chapters 1, 2 and 6 is given.

Appendix B: Geometry of the composite beams studied in Chapter 4 is presented.

Appendix C: Information on mechanical properties of the composite materials of the beams studied in Chapter 4 is given in details.

This page is intentionally left blank.

Chapter 2

Experimental study of a coupled wind turbine blade section

2.1 Background and objectives

Blades of modern MW-sized wind turbines are made of composite materials such as glass fiber reinforced plastics (GFRP). The use of composites is mainly dictated by their high stiffness-to-weight ratios allowing for manufacturing of lighter and stiffer structures. In spite of the fact that nowadays the anisotropic properties of the fiber reinforced composite materials are well known, they are not widely exploited in the present wind turbine blades.

The anisotropy of composite materials can be utilized in design of new large blades by controlling the ply orientations in the structural layup in a smart manner so that effects of certain elastic couplings occur in the structure. The bend-twist coupling is one of the most relevant for the wind turbine blades addressed in the present study. The effect of the bend-twist coupling appears in a blade structure as a link between its two basic deformation states – bending and torsion. Thus, when bended, the blade experiences twist and vice versa – when twisted, it bends, see Fig. 2.1. de Goeij et al. (1999) provided a review on incorporation of the bend-twist coupling to wind turbine blades and the associated coupling effects.

Though, many researchers performed numerical evaluations of the bend-twist coupling effects in wind turbine blades or similar structures, see e.g. Kooijman (1996), Griffin (2002) or Capellaro and Kuhn (2010), only few experimental investigations

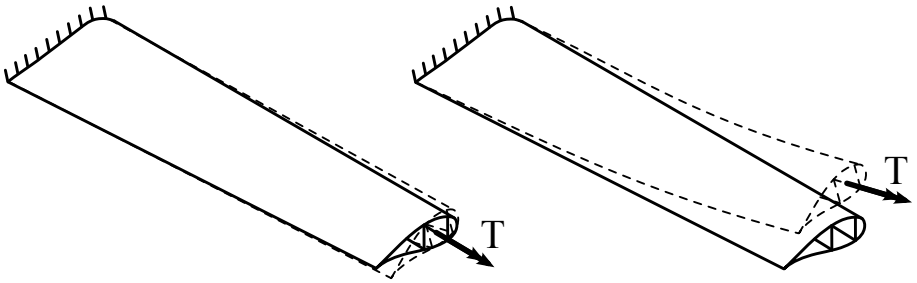

Figure 2.1: Torsion of a traditional design (left) and bend-twist coupled design (right) wind turbine blade sections

can be found in the literature. One objective of the present study is to experimentally investigate the effects of bend-twist elastic coupling in a commercial wind turbine blade section.

For the purpose of investigation, the structure of a traditional wind turbine blade section provided for the study is modified by application of extra GFRP layers in order to introduce a noticeable effect of the coupling. To simplify the analysis, a number of assumptions are adopted based on the design characteristics, geometry and layup of the examined wind turbine section. An advanced hydraulic system is used in the study for specific load application and the Digital Image Corellation techniqe is utilized for 3D displacement measurements on coupled structural response of the modified blade section.

2.2 Problem definition

In this section, a simple case of a uniform beam is discussed first to present the way the bend-twist elastic coupling effects are considered in beam models. Then, a detailed description of the subject examined in the present experimental study – a commercial wind turbine blade section, is given. Finally, an approach for evaluation of the bend-twist coupling effects in the blade section and the assumptions considered in the approach are presented.

2.2.1 Bend-twist coupling in uniform beams

Consider the case of a uniform beam fixed at one end and loaded at the other end, see Fig. 2.2. The beam is oriented with respect to the reference coordinate system

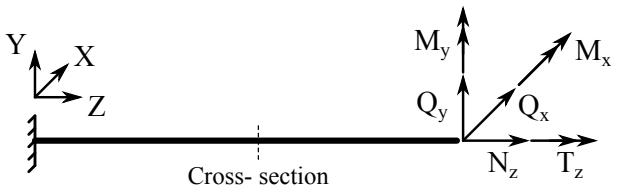

Figure 2.2: Case of a loaded beam

XYZ so that the beam axis is aligned with Z axis and perpendicular to the XY plane. The beam can in general be loaded by six independent load cases: Tensile force N_z, transverse shear forces in two principal directions Q_x and Q_y, torque T_z and bending moments M_x and M_y. According to Timoshenko beam theory and St. Venant's principle, a cross-section far enough from the constrained and loaded ends of the beam can experience six independent deformation states corresponding to: beam elongation ϵ_z, shear deformations in two principal directions γ_x and γ_y, twist κ_z and bending in two principal directions κ_x and κ_y. Relation between the generalized section forces gathered in the vector $\mathbf{F} = [Q_x\, Q_y\, N_z\, M_x\, M_y\, T_z]^T$ and the cross-section deformations in form of a vector $\mathbf{U} = [\gamma_x\, \gamma_y\, \epsilon_z\, \kappa_x\, \kappa_y\, \kappa_z]^T$ can be described by a 6x6 cross-section stiffness matrix $\mathbf{K}$:

$$\mathbf{F} = \mathbf{K}\mathbf{U} \tag{2.1}$$

Alternatively, the inverse relation can be written using a compliance matrix $\mathbf{S}$ which is inverse of the stiffness matrix: $\mathbf{S} = \mathbf{K}^{-1}$:

$$\begin{bmatrix} \gamma_x \\ \gamma_y \\ \epsilon_z \\ \kappa_x \\ \kappa_y \\ \kappa_z \end{bmatrix} = \left[\begin{array}{ccc|ccc} S_{11} & S_{12} & S_{13} & S_{14} & S_{15} & S_{16} \\ & S_{22} & S_{23} & S_{24} & S_{25} & S_{26} \\ & & S_{33} & S_{34} & S_{35} & S_{36} \\ \hline & Symm. & & S_{44} & S_{45} & S_{46} \\ & & & & S_{55} & S_{56} \\ & & & & & S_{66} \end{array}\right] \begin{bmatrix} Q_x \\ Q_y \\ N_z \\ M_x \\ M_y \\ T_z \end{bmatrix} \tag{2.2}$$

In the compliance matrix formulation, the bend-twist elastic coupling conserning bending around X axis is defined by the coefficient S_{46} (S_{56} – for bending around the Y axis). It specifies the two following relations: between the applied generalized torque T_z and the generated cross-section bending rotation κ_x as well as between the applied generalized bending moment M_x and the generated cross-section twist κ_z.

To define the cross-section stiffness or compliance matrices in the given format, a reference coordinate system has to be selected, which can actually be done in

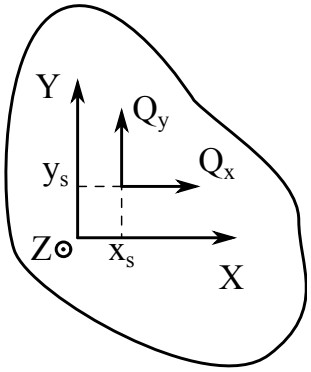

Figure 2.3: Application of transverse shear forces in the plane of an arbitrary cross-section.

several ways. It is demonstrated by e.g. Kosmatka (1994) or Hodges (2006) that for uniform beams with no bend-twist elastic coupling it is possible to locate a point in the cross-section plane with certain unique properties. Consider two transverse shear forces Q_x, Q_y applied at the beam tip at a point $\{x_s\, y_s\}$ in the cross-secion plane as depicted in Fig. 2.3. With the beam length L, the forces produce the following bending and torsion moments distributions along the beam:

$$M_x = -Q_y(L-z); \quad M_y = Q_x(L-z); \quad T_z = -Q_x y_s + Q_y x_s \tag{2.3}$$

Distribution of the corresponding cross-section twist deformation is therefore:

$$\kappa_z(z) = [S_{16} - S_{56}(L-z) + y_s S_{66}]Q_x + [S_{26} - S_{46}(L-z) - x_s S_{66}]Q_y \tag{2.4}$$

A condition of zero twist generated by any applied shear force may be set. For a beam with no bend-twist coupling ($S_{46} = S_{56} = 0$), the point where the force has to be applied to fullfil the condition of zero twist is called shear center and is determined as:

$$x_s^u = -\frac{S_{26}}{S_{66}} \qquad y_s^u = \frac{S_{16}}{S_{66}} \tag{2.5}$$

For uncoupled beams, selection of the shear center as the reference coodinate system origin allows uncoupling of the applied transverse shear forces from the beam twist as $S_{16} = S_{26} = 0$. In other words, a transverse shear force applied at the shear center position will not cause twist of the beam, and a torque applied to the beam will not couse displacement of the shear center.

However, it is also demonstrated that for the beams with non-zero bend-twist coupling, shear center cannot be treated as a cross-section property, as the beam twist in this case is coupled to the applied transverse shear forces through the bending moments generated along the beam by these shear forces. From (2.4), the shear center position for a coupled beam is determined as:

$$x_s^c = -\frac{S_{26} + S_{46}(L-z)}{S_{66}} \qquad y_s^c = \frac{S_{16} + S_{56}(L-z)}{S_{66}} \tag{2.6}$$

Therefore, for a coupled beam, generally it is not possible to uncouple transverse shear forces from twist simply by selecting a certain reference point. Nevertheless, it is possible to select the shear center position so that the beam loaded by shear forces will undergo twist only due to the bend-twist coupling but not due to the direct coupling between shear forces and twist. The position of this point is calculated according to (2.6), where the bend-twist coupling coeffitients S_{46} and S_{56} are set to zero. Consequently, the expressions for the shear center position will be equivalent to (2.5).

When the cross-section compliance matrix is recalculated wtih the reference point placed at the shear center, the elements S_{16} and S_{26} will vanish, indicating no direct coupling between transverse shear forces and twist. Therefore, any shear force applied at the shear center position at the beam tip will cause twist of the beam only due to the bend-twist elastic coupling and vice-versa – torque applied to the beam will cause deflection of the shear centers along the beam due to bending induced by the bend-twist coupling. The latter case is of a particular interest for the following experimental investigations.

2.2.2 Wind turbine blade section

An experimental investigation is carried out on an 8.4 meter wind turbine blade section. The section is cut out of a 23 meter long commercial wind turbine blade manufactured by Vestas Wind Systems A/S, see Fig. 2.4. It possesses simplified geometry (no internal reinforcements), simplified layup (minimum number of ply-drops) and moderate to low wall thicknesses. The cross-section dimensions vary from 695 mm in chord with 16% airfoil thickness at the section tip to 1490 mm in chord with 21% airfoil thickness at its root. In addition to the tapering of the blade section, it has a very slight pretwist, effect of which is beleived to be insignificant.

The wind turbine blade section itselft is a lightweight composite structure. It consists of three major parts: the pressure and the suction side outer shells and

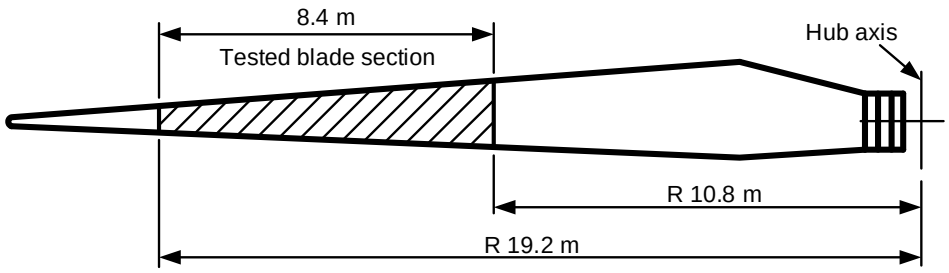

Figure 2.4: 23 meter wind turbine blade provided by Vestas Wind Systems A/S and a section chosen for experimental investigations

a load carrying spar. All the parts are glued together by a relatively thick layer of epoxy adhesive, see Fig. 2.5. The pressure and the suction sides are two shell structures with precisly defined outer shape forming the blade airfoil. Both shells are sandwich structures with glass-fiber reinforced plastics (GFRP) in the face sheets and PMI foam in the core. The thickness of the sandwich structure is maximum at the trailing edge area and minimun at the leading edge and the spar shear webs. The ratio wall thickness, t, to profile height, h, for the blade section varies from less then 0.02 at the leading edge near the root and up to 0.25 at the trailing edge of the blade section tip.

The outer surface of the shells is covered by gelcoat which is a usual way to protect composite materials from exposure to moisture, direct UV radiation etc. The load carrying spar is a nearly rectangular box-beam with relatively thin to moderate walls made from GFRP. In the root part of the blade section, where the spar cross-section is larger, the vertical walls of the spar are made as sandwich structures with a PVC foam core, see Fig. 2.5. Details on the blade section materials and layup are given in Appendix A.

The blade section has been previously investigated by Berring et al. (2007), where it was modified as an attempt to introduce substantial bend-twist coupling to the strucutre. The modification was done by removing the gelcoat and applying extra GFRP layers of uniform 4.4 mm thickness on both pressure and suction sides of the section. All the fibers of the extra layers on both sides have the same direction of 25° with respect to the blade longitudinal (pitch) axis. The fiber direction was selected after a series of preliminary numerical analyses to provide highest bend-twist coupling effect in the blade section. Details regarding the preliminary analyses and the modifications can be found in Berring and Knudsen (2006). The modified blade section is shown in Fig. 2.6.

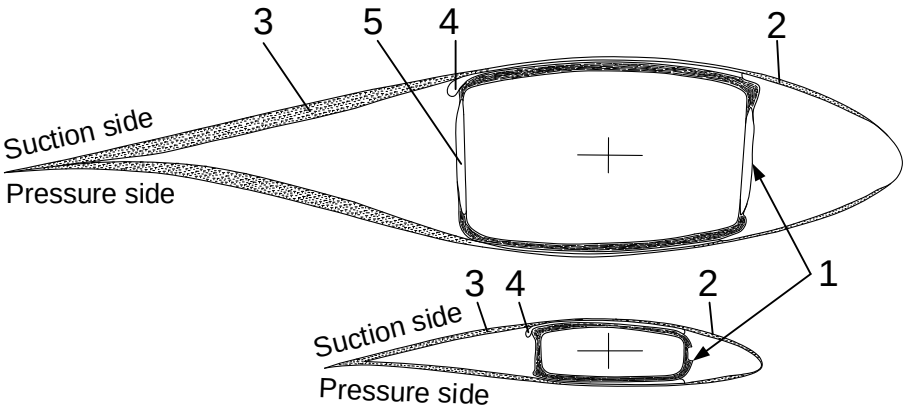

Figure 2.5: The root and the tip cross-sections of wind turbine blade section. In proportions. 1 – spar, 2 – sandwich structure in the leading edge, 3 – sandwich structure in the trailing edge, 4 – adhesive, 5 – sandwich structure in the spar.

2.2.3 Bend-twist coupling in the blade section

Initially, the wind turbine blade section is considered a general case of a composite beam. The blade section possesses complex cross-section shapes, tapering and slight pretwist. It is built of composite materials with significant level of anisotropy and has several ply drops in the layup along its length. Therefore, the stiffness matrix composed according to the Timoshenko beam theory for a cross-section selected along the blade section can be fully populated. These factors make the pure experimental investigation problem very complex and several assumptions are required for a simpler study of the bend-twist coupling effects in the blade section.

In connection with the design of the blade section, the purpose of the spar is to carry the major part of the aerodynamic loads generated by the airfoil. For this reason the spar consisns of a large amount of unidirectional layers of GFRP material with fibers aligned with the blade pitch axis to provide necessary bending stiffness, torsional stiffness, etc. It can be therefore assumed that contribution of the spar to the overall blade section stiffnesses is much higher than of the outer shell, and the spar configuration mainly determines the coefficients of the cross-section stiffness matrices along the blade section. Hence, it also determines the elastic couplings, if any, in the original blade section.

The load carrying spar is a beam with nearly rectangular cross-sections, see Fig. 2.5. Due to symmetrical configuration of the spar cross-sections with respect to the flap-wise principal bending direction, the couplings between the axial force

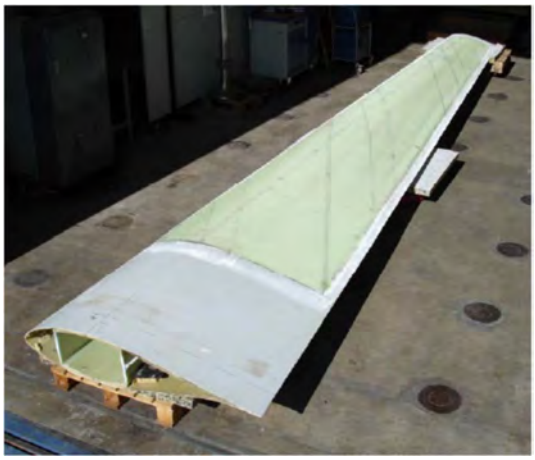

Figure 2.6: Wind turbine blade section after its modification. The extra GFRP UD layers are seen as a light-green layer on top of the blade section with the fiber direction shown by dark lines.

and bending and twist as well as the couplings between transverse shear forces and bending and twist are negligible. In addition, the coupling between the edge-wise bending and twist is also very small. This can be easily demonstrated by application of the Classical Laminate Theory to symmetric laminates, see e.g. Zenkert and Battley (2006).

As the fibers in the spar flanges are aligned with the blade pitch axis, the elastic coupling between the flap-wise bending and twist in the original blade section configuration is considered to be insignificant. Pollock et al. (1995) demonstrated that for a closed cross-section the shear center is lying in the cross-section centroid and does not deviate significantly from this position, thus the shear centers of the spar cross-sections are lying in the center of symmetry of the spar and therefore form a straight shear center line. To estimate the shear center positions along the entire blade section due to basically unknown influence of the outer shell strucure to the shear center position, the shear center line of the blade section is assumed to be straight and parallel to the pitch axis but not necessarily coinciding with the pitch axis (the same as the spar center line).

The above assumptions lead to a situation, where a torque applied to the free end of the clamped blade section generates only a constant torsion moment along the blade section and produces no deflection of the shear center line in the flap-wise principal bending direction, see Fig. 2.7. Thus, the best approximation of the shear center line position as a line with minimal bending displacements can be evaluated based on the results of the experiments where torque is applied to the

original blade section.

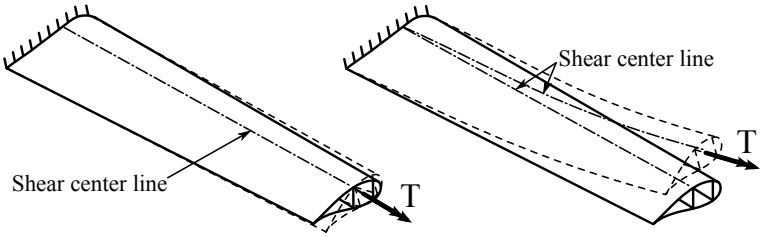

Figure 2.7: Torsion of the original (left) and modified (right) blade section.

The modification of the blade section by application of extra UD GFRP layers on its pressure and suction sides lead to increased blade section bending and torsional stiffnesses. It could as well affect the distribution of the shear center positions along the blade section. However, to keep the problem of the modified blade section simple enough for a pure experimental study, it is assumed that the shear center positions for the modified blade section are the same as those for the original blade section. It is demonstrated by Pollock et al. (1995) that the variation of material parameters produce insignificant deviation of the shear center position for closed section beams. This effect can hereby be adopted to the case of the modified blade section if the the applied extra layers of GFRP material are considered as part of the very stiff load carrying box spar flanges.

The set of the adopted assumptions allows for a simple experimental investigation on the bend-twist coupling effect in the modified blade section in torsion load case by demonstration of the bending deflection of the shear center line determined experimentally for the original blade section, see Fig. 2.7. Presently, the torsion load case is implemented by clamping the blade section at the thicker root end and applying a torque in the form of a couple of forces at its free tip.

2.3 Test setup

In this section the utilized experimental setup is presented. The reader will become acquaint with a test rig for the blade section, tools and methods utilized for load application. A description of the exploited measurement system with the data post processing algorithm developed in the present study will be finally given.

2.3.1 Test rig

A test rig designed by Berring et al. (2007) is exploited in the present study. The concept of the test rig is to apply fully clamped boundary condition to the blade section root end by mean of two specially designed clamps. These clamps, called "root clamps", are mounted at the root part of the blade section with a distance of 1.63 m apart. Each root clamp is made as a pair of standard steel U-beams with ply-wood inserts between them. The ply-wood inserts have the same shape as the airfoil of the blade section at the clamping position. Rubber stripes are placed between the blade section and the wooden inserts of the clamps for better contact. Further, the root clamps are mounted to the strong floor in the test facilities through a set of steel columns, see Fig. 2.8.

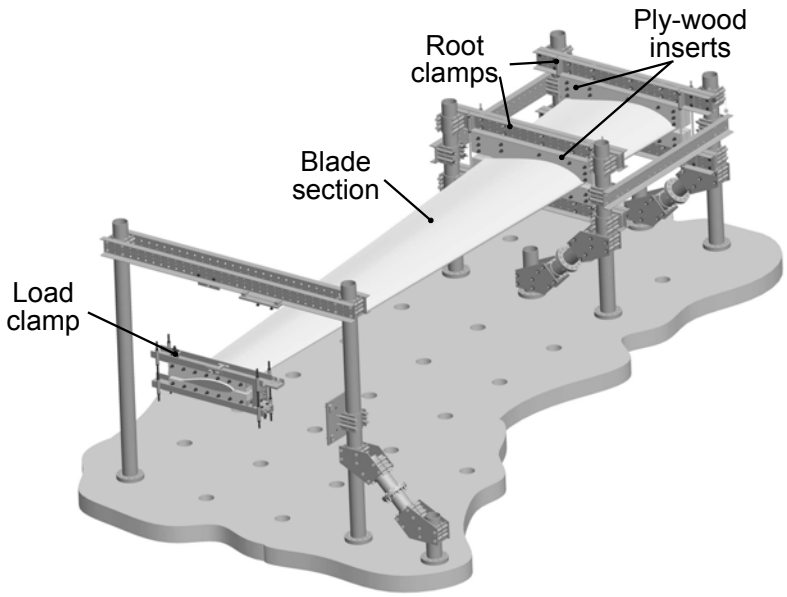

Figure 2.8: 3D drawing of test rig. The blade section is clamped by two "root clamps" while the load is applied through the third "load clamp".

At the free end of the clamped blade section there is mounted a third clamp, called "load clamp" and designed similar to the root clamps. The function of the load clamp is to provide an interface for load application at the free end of the blade section. For mounting of the loading equipement, a system of columns is built

around the blade section free end with the mounted load clamp. Thus, with 8.4 m of the total length of the blade section, the tested length (mounting excluded) is only 5.96 m. A 3D drawing of the test setup with the clamped blade section can be seen of Fig. 2.8. Fig. 2.9 shows a photo of the entire setup for the present experimental study.

Figure 2.9: Test setup for blade section in test hall.

2.3.2 Load cases and load application

Four load cases are applied to the modified blade section in the present study. The first two load cases are the torsion cases, where torque is applied to the free end of the blade section as a pair of opposite equivalent forces acting a certain distance apart (the arm of the force) so that the resultant load consists only of a torque at the tip – neither axial or transverce forces and no bending moments are presented. In the first torsion load case (clamp torsion) torque is applied to the blade section through the load clamp, and thus the load is distributed along the outer surface of the blade section. In the second torsion load case (spar torsion) torque is applied through the handle directly to the inner surface of the load carrying spar. Illustration of both torsion load cases can be seen in Fig. 2.10.

Loading of blades by mean of clamps is a common approach for experimental studies. However, the outer shell of the examined wind turbine blade is much weaker than the load carrying box spar. Hence, the clamp loading can lead to significant local deformation of the outer shell and can therefore influence the measurement results near the blade section tip (details on the measurements are given in the next section). To investigate the dependence of the blade section measured response to different torque application approaches, an extra torsion load case is applied in the experimental study. The extra torsion load case concerns application of torque directly to the blade section spar without utilization of the

clamp. It is expected that the application of torque directly to the spar can reduce the local outer shell deformations near the blade section loaded end.

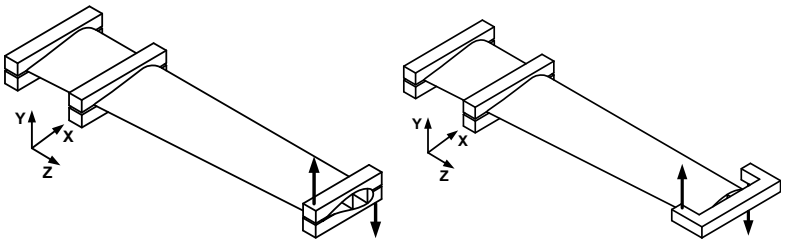

(a) Clamp torsion (b) Spar torsion

Figure 2.10: Torsion load cases

A special steel handle is designed for the spar torsion load case. According to the load case, a pair of equivalent forces are to be applied directly to the blade section spar. Therefore, the handle is designed as a steel box to fit the inner dimensions of the blade section spar at its loaded end. A couple of steel bars are welded to the steel box to provide an interface for the loading equipement. In the experiments the handle is placed so that the steel box is inside the spar. Fixation of the handle is made by means of thin rubber inserts between the steel box and the spar. The rubber inserts also protect the inner surface of the spar from local stress concentrations by providing larger contact area between the steel box and the spar, see Fig. 2.11.

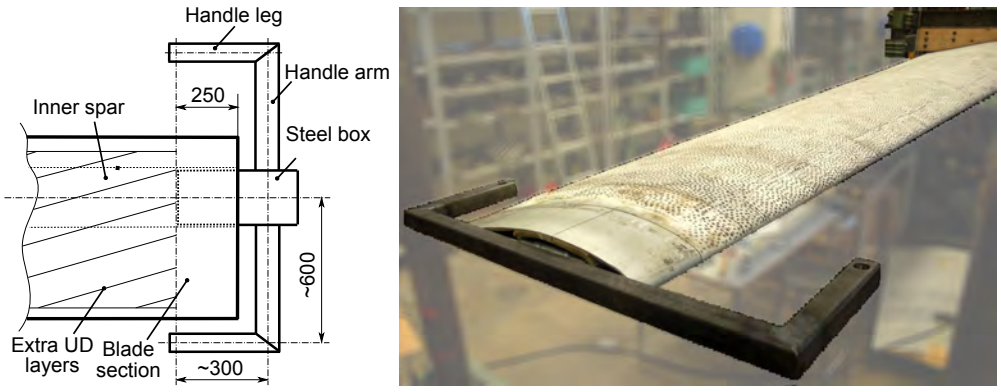

Figure 2.11: Handle for the spar torsion load case. Left: Drawing of the handle. Right: The handle mounted in the blade section

According to the problem definition, the shear center line is to be defined from the

experiments on the original blade section. Such results have been generated by Berring et al. (2007). Between his work and this study the modified blade section was subject to very high load levels by Dimitrov (2008). Therefore, to verify that the modified blade section structure is still intact and has no serious deviations from its original mechanical properties, the second pair of load cases is presently applied. The two load cases are the flap-wise shear force bending and the flap-wise shear force bending with torsion. In both cases the load is applied as a single shear force acting in the former case at the spar center position and in the latter case ca. 0.7 m away from the spar center position, Fig. 2.12.

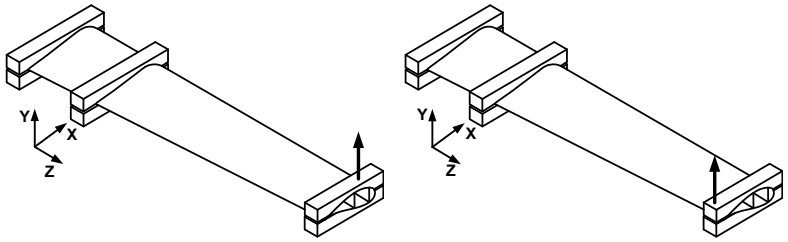

(a) Flap-wise bending (b) Flap-wise bending and torsion

Figure 2.12: Flap-wise shear force bending load cases

All the load cases of the present study are applied by mean of an advanced multi-axial servohydraulic system. The system consits of two 250 kN compact hydraulic actuators operated either in displacement or load control, automatically or manually through a control panel for each actuator and a main PC connected to the servohydraulic controller, see Fig. 2.13. Each of the actuators is equipped with a position sensor (linear variable differential transformer - LVDT) and a load sensor (force transducer), thus it can deliver both displacement and force signals. The PC in the hydraulic system setup stores the displacement and force signal values into a log file at a chosen sampling rate.

In the two shear force bending load cases, Fig. 2.12, a single actuator is operating in the displacement control mode. The actuator is following a linear ramp signal and the displacement and force signals are recorded every second. The two bending load cases are the most safe and easy to perform.

The load levels considered in the present investigation are chosen to be of the same magnitudes as for the corresponding loads previously applied to the original blade section by Berring et al. (2007). It facilitates exposing the differences appeared in the mechanical behavior of the original blade section after the modifications.

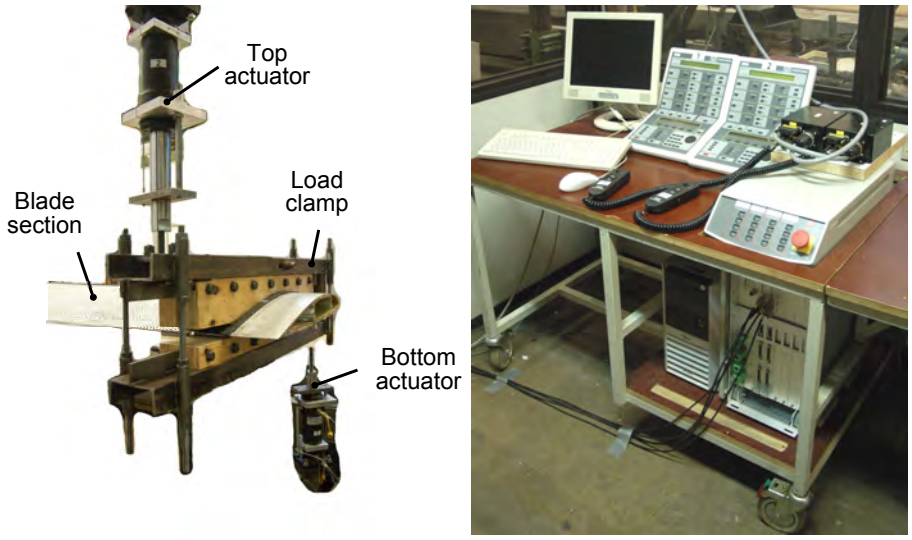

Figure 2.13: Left: Hydraulic actuators at load clamp in the clamp torsion load case. Right: Hydraulic system controller with control panels and PC

Thus, in the shear force bending load cases, forces of 4.0 kN are applied, and in the torsion load cases torques of 2.5 kNm are applied.

At the first attempt both actuators were utilized in the load control mode. One of the actuators was chosen as a "master" actuator, while the second one was a "slave" actuator. The idea behind the slave actuator is to operate so that it copies the behavior of the master actuator providing equal force. As both actuators were intended to run in the load control mode, they were to follow the required load path. But the interconnection of the actuators through a stiff load clamp or the handle in both torsion load cases led to instability of the entire system. As a result, the actual loading did not comply with the required path, see Fig. 2.14. To overcome the instability problem, the loads were successfully applied by manual step-wise load control of the actuators via the displacement control mode.

2.3.3 Measurement system and processing algorithm

Full field 3D measurements on the wind turbine blade section top surface are performed in the present experimental study by utilization of a Digital Image Correlation (DIC) system ARAMIS developed by GOM MbH, see GOM (2008). The DIC measurement technique consists of digital processing of stereo pictures

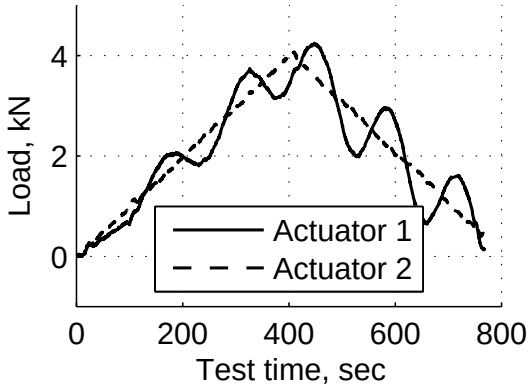

Figure 2.14: Example of load history in case of hydraulic system instability in the clamp torsion load case applied in load control.

taken by a pair of rigidly fixed digital cameras. As a result, 3D coordinates of a number of points composing the measured surface and the spatial displacements of the points can be obtained.

The DIC system ARAMIS exploited in the present work consists of two digital cameras mounted on a very rigid carbon-fiber reinforced camera bar and a personal computer for control of the cameras and post processing of the acquired images, see Fig. 2.15. The DIC system is capable of providing accurate measurements of a full 3D displacement field of a visible surface of the blade section in form of 3D displacement vectors of the points constituting the measured blade section surface. The DIC system ARAMIS also has a set of built-in tools for advanced post processing and analysis of the results. However, there is a possibility to export the measured data in comma separated files for further processing by MATLAB.

The DIC system has following configuration: A setup of two 4 megapixels digital cameras installed on a very stiff 1.6 m CFRP camera bar is mounted on special platform built about 2 m above the clamped blade section. The measurement volume (i.e. a volume where accurate measurements are possible for the current configuration) is about 4 x 4 x 4 meter. Taking into account the expected blade section deformation, the DIC system is able to measure a 2.0 - 2.5 m blade section part at a time. A schematic view of the DIC system setup is depicted in Fig. 2.16.

Due to limited size of the measurement volume, in each load case the entire surface of the blade section is measured in three steps. At each step the blade section is loaded and deformation of a 1/3 of its surface is measured. Thus, a full picture of the blade section response in each experiment on the blade section is obtained by

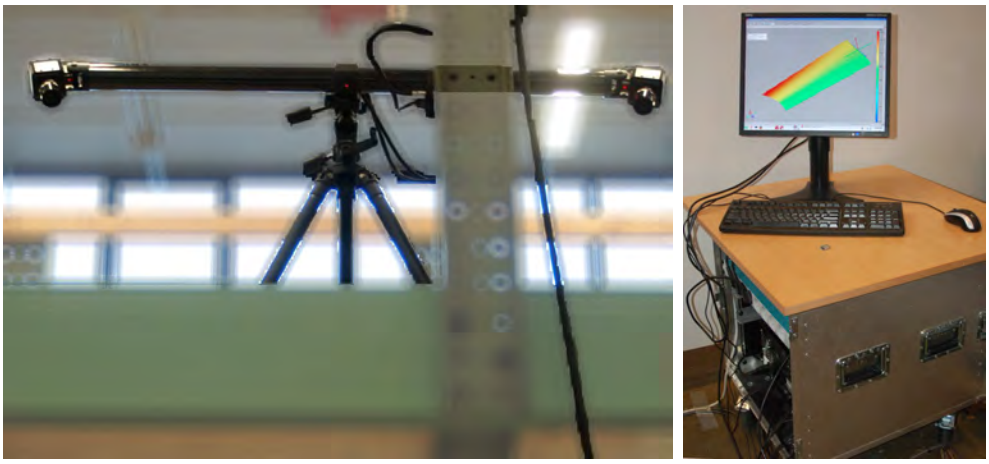

(a) Digital cameras on CFRP bar (b) PC

Figure 2.15: DIC system ARAMIS.

three loading sequencies. At each measurement the readings of the displacement and the force signals for both hydraulic actuators are logged. An example of the results for the three step measurements by the DIC system is given in Fig. 2.17.

To extract the wind turbine blade section response in form of parameter variations along its length, eleven cross-sections are selected from the measured top surface. The cross-sections are evenly distributed along the blade section length with a distance of 0.5 meter between each other and numbered from 1 to 11 starting from the cross-section closest to the blade section root. The first cross-section is only 0.456 m away from the root clamp and the eleventh cross-section is 0.52 m away from the tip clamp, see Figure 2.18.

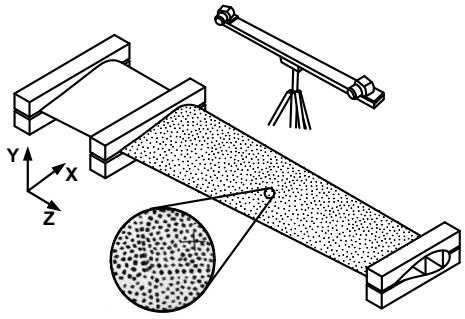

Figure 2.16: Scheme of DIC system ARAMIS setup with an example of stochastic pattern applied to the blade section for better surface recognition.

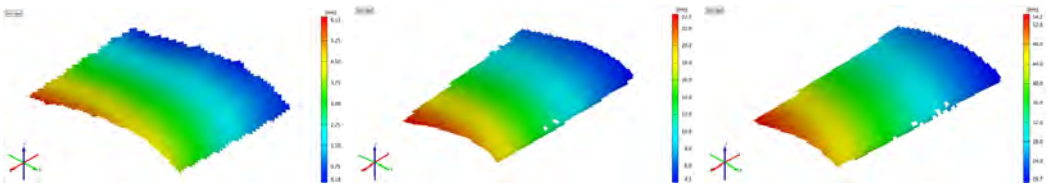

(a) Root part (b) Middle part (c) Tip part

Figure 2.17: An example of DIC measurements results. Bending displacement of three parts of the blade section in the shear force flap-wise bending with torsion load case.

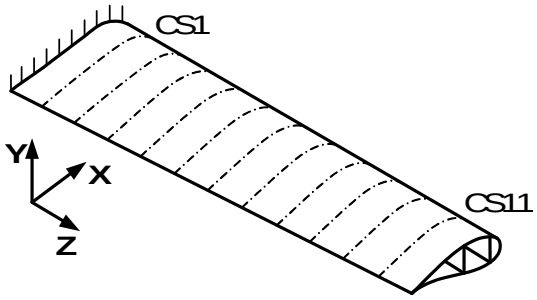

Figure 2.18: 11 evenly distributed cross-sections chosen from the entire top surface of the blade section for calculation of bending displacements and twist angles (the clamps are not shown).

The two main parameters – flap-wise bending displacement and twist angle – are calculated for each of the selected cross-sections based on the 3D displacement components of each point constituting the cross-section obtained by the DIC system. Both in-plane and out of plane cross-sectional deformations are considered to be very small with respect to the deformations due to bending and twist. Validity of this assumption was later proved by random checks during the experiments.

Technically, the twist angles for the selected cross-sections are determined as follows: First, a line is fitted to the bending displacements δy of the points of the cross-section along the width coordinate x by mean of the least square method, see Fig. 2.19. The twist angle and bending displacement are extracted from the linear function of the fitted line. The twist angle is taken as the slope of the line, while the bending displacement is taken as the δy coordinate of the line at a selected position x. Vizualisation of the method is depicted in Fig. 2.19 and the algorithm is given in Table 2.1.

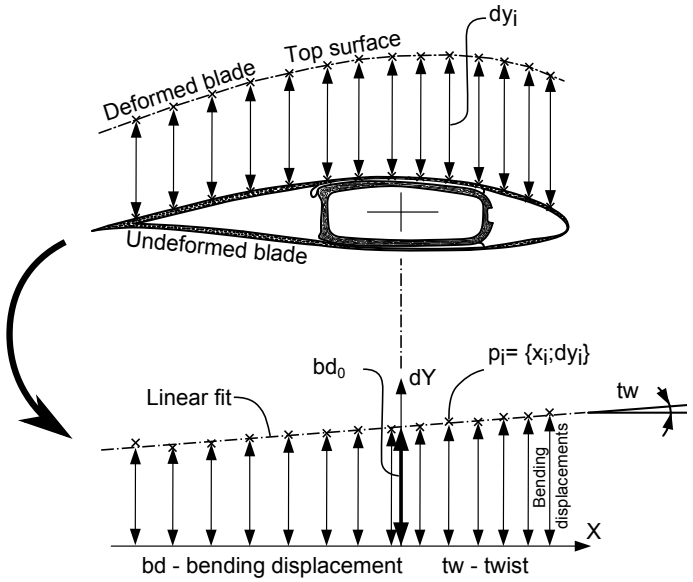

Figure 2.19: Algorithm visualization for calculation of bending displacement and twist angle for a cross-section.

Table 2.1: Calculation of cross-section bending displacement and twist.

$p_i = \{x_i, \delta y_i\}, \quad i = 1, N$	- cross-section points
$\delta y = tw \cdot x + bd_0$	- linear fit
tw	- twist
bd_0	- spar center bending displacement

Similar DIC measurement techniques was used by Berring et al. (2007) in studies on the same wind turbine blade section. However, the DIC data post processing methods exploited there are not robust. For example, to determine the bending displacement of a cross-section, simple averaging of the displacements Δy_i of all N points constituting the cross-section was used:

$$\Delta y = \sum_{i=1}^{N} \frac{\Delta y_i}{N} \tag{2.7}$$

This method is clearly sensitive to such factor as uneven distribution of the measured points along the cross-section. It can easily happen, as the distribution of the points in the exploited DIC system is not controlled by user and there is a good chance of some parts of the measured surfaces are more populated with points

than the others. Besides, it can be shown, that when used, this averaging process represents bending displacement at the mid-width position of a cross-section and only if all the measured points are uniformly distributed along the cross-section.

One of the practical problems with reduction of data is that clamped boundary conditions were applied to the blade section by means of a pair of clamps mounted at the blade section root. In spite of the rubber inserts between the root clamps and excellent fitting, the blade section was still able to move slightly at the root clamps even though they were very well tightened. The observed movements are small but were still able to significantly affect the results at the tip of the blade section due to its considerable length.

A solution for the problem of boundary conditions has not been found and for this reason it is presently solved numerically by correction of the obtained experimental results. The idea behind the approach is to reduce the results to the first cross-section (closest to the root) setting the bending displacement, bending angle and twist angle to zero. This can be considered as application of ideal boundary conditions to the blade section at the position of the first cross-section. When this modification is done, the distributions of bending displacements and twist angles along the blade section, obtained even for different load cases, can be placed on the same plots to facilitate the analysis process.

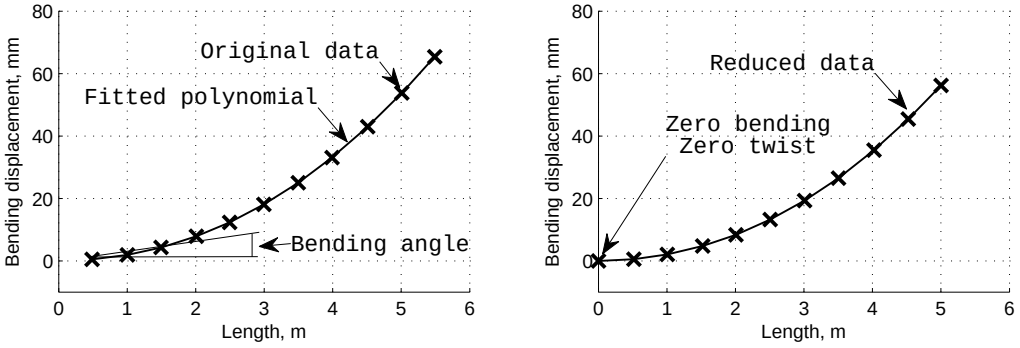

(a) Original results

(b) Reduced results

Figure 2.20: Visualization of reduction algorithm for imperfect clamped boundary conditions compensation

The reduction of the results is done as follows: First a third order polynomial fit by the least square method is performed to the obtained results of the bending displacement as a function of the blade length. Then the bending angle is calculated at the position of the first cross-section as a value of the obtained polynomial

first derivative. Next, all the bending displacements along the blade length are accordingly reduced so that the first cross-section has zero displacement and zero bending angle. Similarly, the twist angles along the blade section are reduced by the twist angle of the first cross-section, so that the the first cross-section has zero twist. See Figure 2.20 for visualiztion of the reduction process and Tables 2.2 and 2.3 for the algorithm details.

Table 2.2: Bending displacement reduction algorithm

$p_i = \{z_i, bd_i\}, \quad i = 1, N$	- bending displacement distribution
$bd(z) = a_3 z^3 + a_2 z^2 + a_1 z + a_0$	- polynomial fit
$ba_1 = -\frac{dbd(z)}{dz}\|_{z=z_1} = -3a_3 z_1^2 - 2a_2 z_1 - a_1$	- bending angle at the root CS
$bd'_i = bd_i - bd_1 + bd_1(z_i - z_1)$	- bending displacement reduction
$z'_i = z_i - z_1$	- length coordinate reduction

Table 2.3: Twist reduction algorithm

$q_i = \{z_i, tw_i\}, \quad i = 1, N$	- twist distribution
$tw'_i = tw_i - tw_1$	- twist reduction

The algorithms for the bending displacements and twist angle calculations as well as the reduction algorithm presented here are implemented in a series of MATLAB scripts for fast automatic processing of the DIC measurements results.

2.4 Experimental results and discussion

First presented are the results of the experimental study on both the original and the modified wind turbine blade sections, obtained by utilizing the DIC data processing algorithm developed in the present study and applied to the original DIC measurements by Berring et al. (2007). Next, the results of the present experiments on the modified blade section are presented. As for all the cases, the DIC measurements are processed according to the same algorithm they are all comparable against each other.

The results of the two flap-wise shear force bending tests on the original blade section are represented in Fig. 2.21. Here the bending displacements at the spar

center position showed no significant differences between the two load cases, Fig. 2.21(a). The only considerable difference was in the twist distributions along the blade section, Fig. 2.21(b): With the shear force applied at the spar center position, rather small twist angles were observed along the entire blade section; when the shear force was applied away from the spar center, corresponding to an extra 2.78 kNm torque applied at the tip, the blade section gradually twisted resulting in ~ 1 degree tip twist.

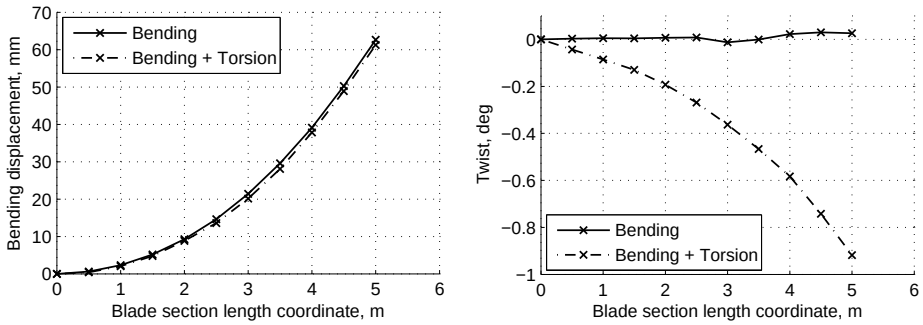

(a) Bending (b) Twist

Figure 2.21: Original blade section. Results of flap-wise shear force bending and flap-wise shear force bending with torsion tests. The bending displacements are measured at the spar center positons. Tip force 4.0 kN

The very small twist angles observed along the original blade section in the bending load case with the shear force applied at the spar center was a good indication that the spar center line potentially represents the desired shear center line of the original blade section.

When the torsion load case was extracted from the two flap-wise bending load cases by superposition, significant scatter were observed in the bending displacement results at the positions of 2.5 - 3.5 m (solid line with pluses on the graph), see Fig. 2.22(a). This could cause high deviations in the results of the reduction method due to the nature of the method. Therefore, to avoid negative effects of the observed scatter, these results (at pos. 2.5 - 3.5 m) are excluded from consideration when reduction is performed. The reduced bending displacements corrected this way are plotted as a solid line with crosses, Fig. 2.22(a).

The problem of the measurements deviation in the positions of 2.5 - 3.5 m may be caused by disturbances during the discrete three-step DIC measurements motivated by limited measurement volume of the DIC system setup. Particular care

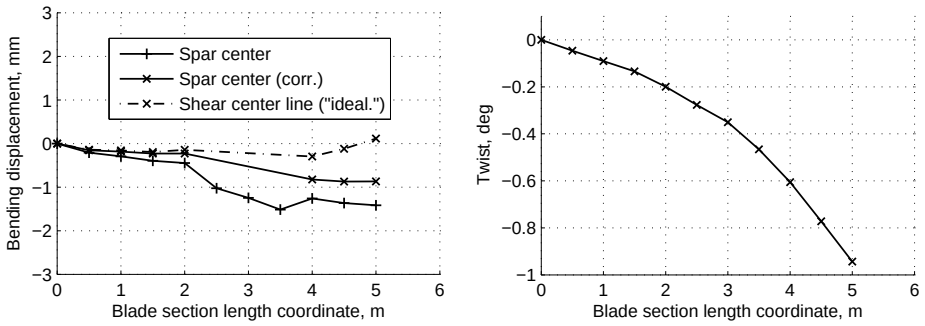

(a) Bending (b) Twist

Figure 2.22: Original blade section. Results of torsion test obtained by superposition of the results of the shear force bending and the shear force bending with torsion tests. Tip torque 2.78 kNm

and attention is therefore required to the discrete DIC measurement approach for generating reliable results. The same problem can be as well explained by higher absolute measurement noise in the two bending load cases due to generally much larger measured displacements. If the measurement noise is assumed as 0.1% of the measured value (corresponds to very precise measurements), then for the 60 mm bending deflections observed in both bending tests, the absolute error can be up to 0.6 mm. After the superposition, the 0.6 mm absolute error already corresponds to a very high 60% measurement error for the ~ 1 mm bending displacements.

In the view of the above arguments and the very small bending deflections of the spar center line for torsion, the spar center line was defined as the shear center line. This corresponded well with the adopted asssumption of a straight shear center line coinciding with the spar geometrical center. Yet, if the experimental measurements are considered errorless, then the "idealistic" shear center line with minimal bending displacements was then defined as a line parallel to the spar center but 10 cm closer to the trailing edge. The results of the bending displacements along both the spar center line and the "idealistic" shear center line are plotted in Fig. 2.22(a).

The results of the two bending tests presently performed on the modified blade section were found to be equal to the corresponding results on the modified blade section obtained by Berring et al. (2007). Thus, it was demonstrated that the blade section kept its structural properties in between the previous and the present studies even after high level loading performed by Dimitrov (2008) and the results of the present study are comparable to the results obtained by Berring et al. (2007).

The results of the bending tests of the modified blade section are presented in Fig. 2.23. Significant twist was observed along the modified blade section with the shear force applied at the spar center position, Fig. 2.23(b). From the same plot it is seen that when the shear force was applied away from the spar center, the tip twist was less than the corresponding tip twist for the original blade section. This was apparently due to increased torsional rigidity of the blade structure provided by the applied extra 25° GFRP layers.

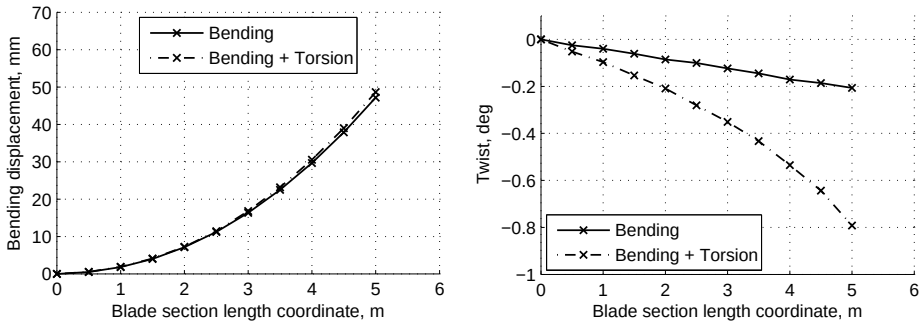

(a) Bending (b) Twist

Figure 2.23: Modified blade section. Results of flap-wise shear force bending and flap-wise shear force bending with torsion tests. The bending displacements are measured at the spar center positons. Tip force 4.0 kN

With the spar center line found to be a good representation of the original blade section shear center line, and in connection with the assumption of the shear center line being unaffected by the blade section modification, the modified blade section twist in the shear force bending test with the shear force applied at the spar center was considered as an indication of the bend-twist coupling effect in the modified blade section.

The results for the torsion test of the modified blade section obtained by superposition of the results of the bending tests are represented in Fig. 2.24. Bending displacements along both the spar center and the "idealistic" shear center line were found to be of low magnitudes – only up to 2 mm at the tip, see Fig. 2.24(a), but possessing a stable trend of the blade section to bend upwards, which was treated as an indication of the bend-twist coupling effect in the modified blade section. The blade section twist is shown in Fig. 2.24(b).

The results of the two torsion load cases – clamp and spar torsion are depicted in Fig. 2.25. Very similar results for bending displacements in the two load

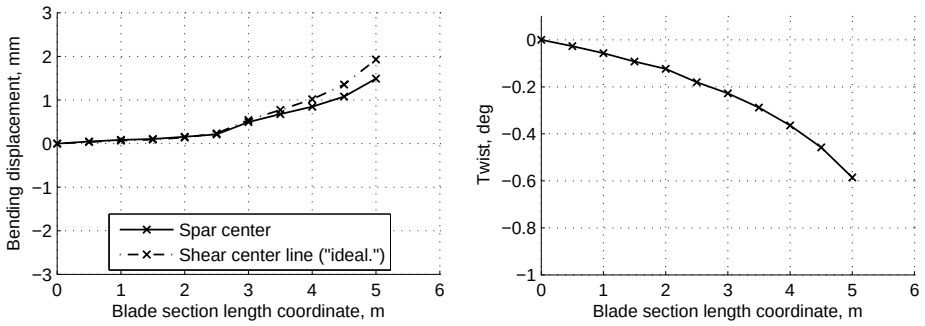

(a) Bending (b) Twist

Figure 2.24: Modified blade section. Results of torsion test obtained by superposition of the shear force bending test results and the shear force bending with torsion test results. Tip torque 2.78 kNm

cases were obtained, Fig. 2.25(a), and therefore the results of only one of the load cases are plotted. The bending displacements were found to be less than those obtained by superposition of the results of the bending tests, Fig. 2.24(a). Similar to the tests on the original blade section, the difference can be explained by higher measurement errors generated by the superposition (as discussed earlier) in contrast to more accurate direct measurements in the two torsion cases. Therefore, the results of the two torsion tests applied experimentally in the present study were considered to be more reliable.

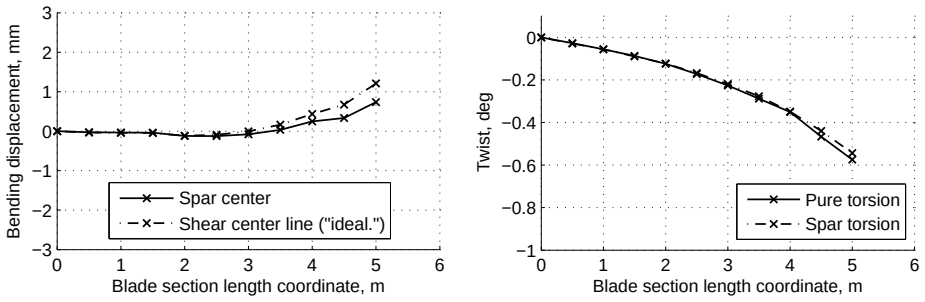

(a) Bending (b) Twist

Figure 2.25: Modified blade section. Results of clamp torsion and spar torsion tests. Tip torque 2.78 kNm

Bending displacements along the “idealistic” shear center line in the two torsion

load cases were found to be small, only ca. 1.2 mm at the blade section tip, yet a stable trend of the shear center line bending was revealed, Fig. 2.25(a). Both the spar center and the "idealistic" shear center line were deflecting in torsion and thus, it was considered as an evidence of the bend-twsit coupling effect in the modified wind turbine blade structure. It seemed like the effect was more pronunced at the tip region of the blade section.

Differences between the twist angles in the two torsion load cases were noticed close to the blade section tip, from position 4.0 m to position 5.0 m, see Fig. 2.25(b). The differences are of small magnitudes but clearly present the outer shell local deformation near the blade section tip. According to the expectations, this happened due to much lower stiffness of the blade section outer shell with respect to the spar. The local deformation region was estimated as ~ 1 m from the point of the torque application. Thus, the spar torsion test results indicated that application of torque to structures with soft shells by mean of a clamp can lead to local shell deformations and influence the DIC measurements. However, this effect was found insignificant in the present study for the blade section and loads considered.

2.5 Conclusions

An experimental investigation on the bend-twist coupling effects in a modified commercial wind turbine blade section was undertaken. The blade section being an inhomogeneous composite beam was found to be a very general and hence a very complex problem and a number of assumptions, like existance of a constant straight shear center line, were applied to simplify the experimental analysis method.

The results of the study demonstrated that the geometrical center of a load carrying spar cross-section well represents the shear center position in a cross-section of the original blade section structure. Under the assumption of the shear center position being insensitive to the blade section modification performed in the study, the effect of the bend-twist coupling in the modified blade section structure was demonstrated by twist measurements in the shear force bending load case when the shear force was applied at the spar center, and also by demonstration of the shear center line bending when the modified blade section was subject to torsion.

It was also found that bending displacements of the modified blade section shear center line, driven by the bend-twist coupling, were rather small for the torsion load case (ca. 1.2 mm for a 2.78 kNm tip torque), which can be problematic for

implementation of accurate experimental measurements. Therefore, the demonstration of twist generated by the coupling in bending load case might be more preferable as very small twist angles can be still accurately measured.

The bending displacements in the torsion load cases obtained by superposition of two shear force bending load cases were shown to produce rather large errors due to higher absolute measurement errors obtained when larger bending displacements were measured in the bending load cases.

The effect of different torque application methods on the twist measurements was revealed by exploiting a new loading approach, where torque is applied directly to the blade spar by utilizing a specially designed hanlde. It was demonstrated, that torque applied through the load clamp can potentially cause local deformations and affect the DIC measurements for the structures with soft shells. For the modified blade section a torque of 2.78 kNm applied through a load clamp created about ~ 1 m local outer shell deformation region, though the influence of the deformation on the twist results were found insignificant.

An advanced servohydraulic system was used successfully in the present study to apply a set of load cases, where some of them required two actuators. Yet, the attempt of operating the servohydraulis system fully automatically was unsuccessful due to the stability problems, operation was accurately done by manual control.

A DIC system was utilized for advanced 3D measurements on the blade section response, and a robust processing method for extraction of the bending displacements and twist angles along the blade section was developed. The method incorporates reduction techniques of the results to ovecome the problem of real (imperfect) boundary conditions. It was also demonstrated that the exploited three-step DIC measurements approach can lead to deviations of the final parameter distributions, especially when small values of bending displacements are measured. Hence a great care should be taken when using such kind of multi-step DIC measurements.

Chapter 3

Numerical modeling of wind turbine blades

3.1 Introduction

During the design process of a modern large wind turbine blade, typically several numerical models of the blade are to be built for analysis of its structural behavior. Each of the models has its own capabilities: some of them are aimed e.g. at static and dynamic global structural response analysis, some are aimed at the stability analysis to study local phenomena such as compressive buckling. Consequently, the models have different levels of detail and requirements to the development process and the computational resources.

Finite element (FE) models are commonly used for analysis of global static and dynamic responses of a wind turbine blade as well as for the aeroelastic computations, where the blade is treated as a general beam. The structure is represented by several beam elements, with typically six degrees of freedom (DOF) at each node (three displacements and three rotations), therefore the total number of DOFs for such a beam model, and requirements for the computational resources are low.

Yet, to formulate a beam element, a rather complex theory, which includes a 2D cross-section analysis carried out either analytically or numerically is required, see Fig. 3.1. Jung et al. (1999) performed an assessment of classical cross-section analysis methods applicable to composite beams. Variational Asymptotical Beam Sectional analysis (VABS) developed by Yu et al. (2002) and BEam Cross-section

Analysis Software (BECAS) developed by Blasques and Lazarov (2011) are two examples of the finite element cross-section analysis methods, applicable to arbitrary cross-sections.

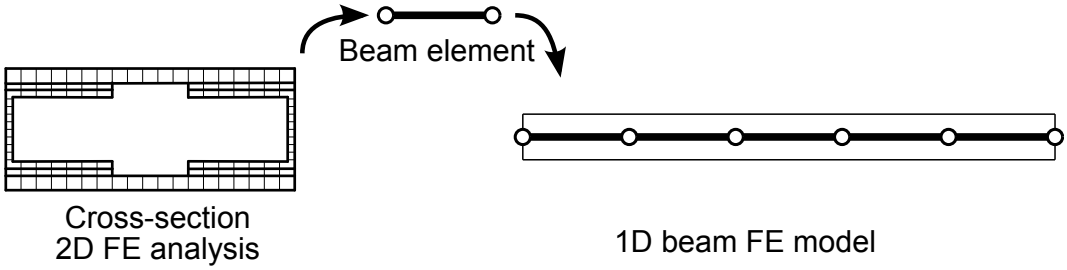

Figure 3.1: Building a beam FE model for a rectangular cross-section beam.

In addition to analysis of global response of the wind turbine blade structures, detailed 3D finite element models have to be developed to analyze local phenomena such as compressive buckling of the structure. The models support complex deformation modes and can account for geometry and material non-linearities for more accurate analysis. To represent a wind turbine blade structure, shell finite elements with 4 to 8 nodes and 6 DOFs per node or solid finite elements with 8 to 20 nodes and 3 DOFs per node are usually used, where the composite material data is input layer by layer, see Fig. 3.2. The size of the elements is determined by convergence analysis of the model and is usually rather small, hence the models typically consist of a large number of finite elements and DOFs. Thus, the computational resources requirements for these models are generally high.

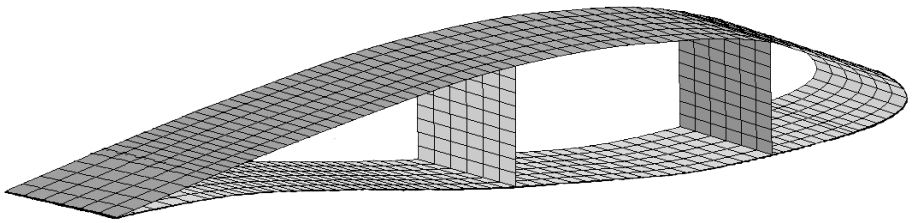

Figure 3.2: Mesh example of a detailed 3D wind turbine blade FE model built of shell elements.

A large number of commercial codes (such as ANSYS, ABAQUS, etc.) are available with ready to use shell and solid finite elements, and there is generally no need for any complex theory to be developed, before a detailed 3D model of a composite structure can be built. Capabilities of modern computers allow huge models with very large number of DOFs to be calculated relatively fast. These factors lead to a situation when detailed full 3D models, capable of predicting complex deformation

modes of the wind turbine blades are utilized to extract the blade properties in form of beam elements as it is done by Malcolm and Laird (2003, 2007).

Development of detailed 3D FE models built of shell and/or solid finite elements is addressed in the present study as an alternative approach for prediction of global wind turbine blade structural response instead of (or in addition to) beam finite element models. Problems regarding the development of detailed 3D FE models of modern composite wind turbine blade structures are therefore considered.

First, structural design approaches concerning wind turbine blades are reviewed where functions and features of the major design components are highlighted. Next, problems of FE modeling of the blades in connection to the blade design features are addressed. Here, a choice of finite elements and problems in connection with utilization of each finite element type are discussed.

A particular case of a commercial wind turbine blade section, modified as an attempt to introduce bend-twist coupling, is numerically studied. Two FE models – representatives of two FE modeling approaches – of the blade section, that have been developed recently, are presented. The first model is built of combination of solid and shell elements, while the second model is built only of shell elements with nodal offsets to the blade outer surface. The results from both models are compared and validated against the experimental data.

Particular attention is paid to the FE model built of shell elements with nodal offsets to the shell outer surface as the most attractive FE model due to significantly simpler development process. It is demonstrated by Laird et al. (2005), that when nodes of the shell finite elements are offset from their original mid-thickness position, the torsional stiffness of the structure is incorrectly calculated. Later it was demonstrated by Dimitrov (2008) and Fedorov et al. (2009), that the problem is common for the shell elements with offsets and independent of the FE solver. Therefore, the prediction of the blade section torsion behavior by the FE model built of shell elements with nodal offsets is closely studied.

3.2 Structural design of wind turbine blades

Modern large wind turbine blades are long slender structures mainly produced of high stiffness-to-weight ratio composite materials such as glass fiber or carbon fiber reinforced plastics (GFRP or CFRP) with e.g. epoxy or polyester as matrix, in combination with other materials like polyvinyl chloride (PVC) foam,

polyvinylisobutyl ether (PVI) foam, polymethacrylimide (PMI) foam or balsa wood, which are typically used as core material in sandwich components in the blades. Detailed overview and selection of the materials common for application to wind turbine blades are covered by Brøndsted et al. (2005).

The blades are made long, slender, pretwisted and tapered from the root to the tip. The pretwist of a wind turbine blade is specified by variation of angle of the attack along its length. The main reasons for the blade tapering is the load distribution due to variation of the aerodynamic loads along the blade. Internal bending and torsional moments in a loaded blade normally increase from its tip to its root. More details regarding typical loads in the wind turbine blade structures can be found in DNV/Risø (2002) and Hansen (2008).

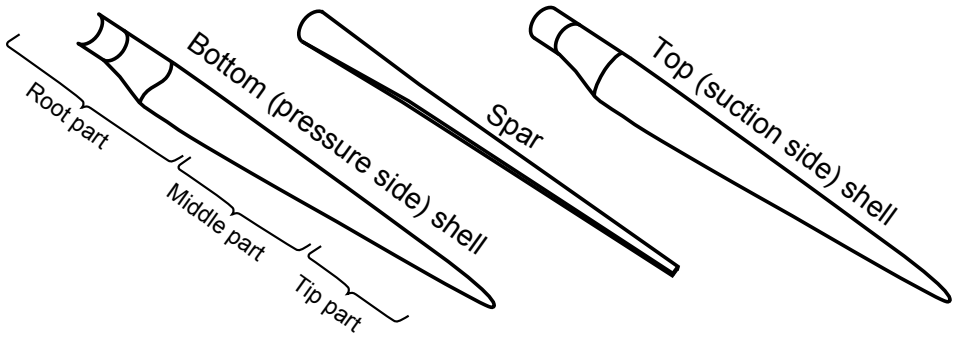

Figure 3.3: Wind turbine blade structural parts.

A modern wind turbine blade is conventionally viewed as consisting of three parts; the root part, the middle part and the tip part, see Fig. 3.3. The root part is a thick-walled structure supprting the high loads. It has a complex geometry due to the blade cross-section transformation from the airfoil shape to a cylindrical shape for connection of the blade to the wind turbine hub. The tip part is represented by thinner airfoils and thin-walled structure with much simpler geometry. The middle part of the wind turbine blade structure is typically a moderate- to thin-walled structure with moderate levels of geometrical and structural complexities.

Typically a modern wind turbine blade consists of several structural parts bonded together by epoxy adhesive. Each of the structural parts of the blade has its own purpose and perform its own function. The shape of the outer surface of the blade is formed by the top (suction side) and the bottom (pressure side) shells and is defined by the required airfoil. The function of the outer shell is to generate the aerodynamic load distributed along the airfoil surface and to transmit it to the load carrying structure - often a spar, see Fig. 3.3.

Thin airfoil shells may collapse in bending due to induced buckling. The trailing and the leading edges typically tend to buckle due to their large sizes. For this reason, sandwich structures (Fig. 3.4) are normally used in the shell walls to increase the resistance to buckling. Thick sandwich structures are mainly used in the walls of the root and the middle parts of wind turbine blades where the bending moments and compression forces are the highest. In the tip part of the blade where loads are not as high, sandwich structure is often not necessary.

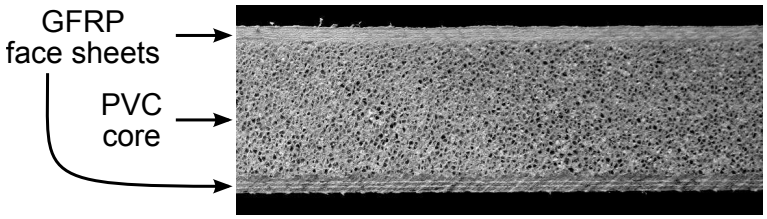

Figure 3.4: Example of a sandwich structure.

To provide a required blade bending stiffness, significant amount of uni-directional (UD) layers of fiber reinforced materials with the fibers aligned with the longitudinal axis are commonly present in the blade structure. Depending on a particular blade design, the UD layers can be part of a thick outer shell or part of the spar flanges. Blades made as pure airfoil shell structures typically possess insufficient resistance to transverse shear loads, therefore, reinforcements in form of one or two shear webs are also used. The shear webs are often made as thick sandwich structures, similarly to the outer shell, to improve their resistance to buckling. Typical structural design approaches for the shear webs and the load carrying spar are given by e.g. Burton (2011).

Several common approaches in design of the load carrying structure of modern wind turbine blades can be highlighted:

- *Box-beam spar.* A load carrying spar is made as a box-beam. Two shear webs are merged together with the UD layers forming the spar flanges and manufactured separately from the airfoil shell. The spar flanges are relatively thick, mainly containing the UD layers and designed to carry most of the axial stresses to ensure sufficient blade bending stiffness. The box-beam shear webs are of moderate thickness and take a significant part of the transverse shear stresses in the wind turbine blade. They are often made as sandwich structures to increase their resistance to buckling, see Fig. 3.5(a).
- *I-beam shear web.* In case of the I-beam spar, the stiff UD layers are part of the aerodynamic shell and the only shear web is presented with the same function as in the case of the box-beam spar, see Fig. 3.5(b)

- *C-beam shear webs.* Two C-beam spars can be used to carry the transverse shear loads in the blade structure. Here the outer shell contains the stiff UD layers similarly to the I-beam configuration, see Fig. 3.5(c).
- *No shear webs.* This design is usually implemented when the airfoil shell is capable of resisting the transverse shear load. It is common that the shear webs, when presented in the blade, do not extend along the entire blade length, leaving the tip part with the no-web configuration, see Fig. 3.5(d).

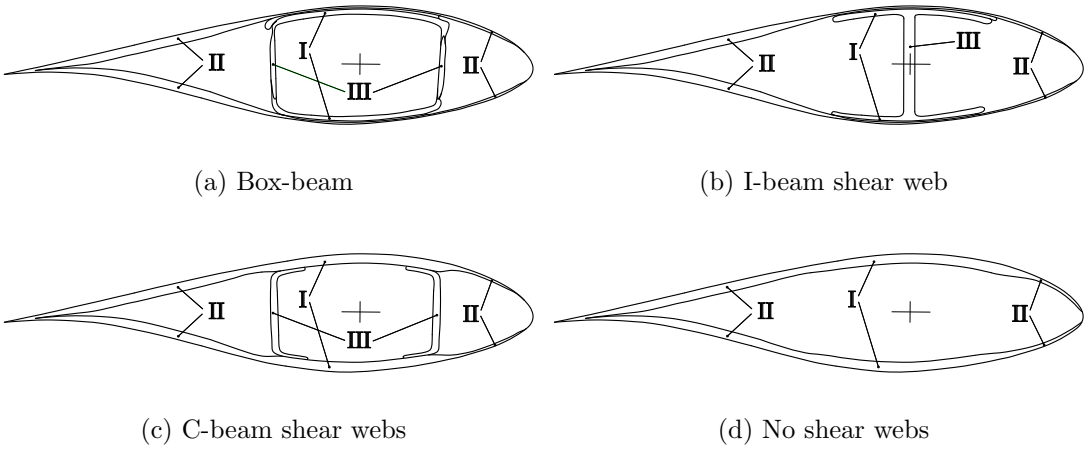

(a) Box-beam (b) I-beam shear web

(c) C-beam shear webs (d) No shear webs

Figure 3.5: Wind turbine blade designs. I - UD layers, II - sandwich structure in leading and trailing edges, III- sandwich structure in shear web of the spar.

3.3 FE modeling of wind turbine blades

FE modeling of the wind turbine blades is considered here with respect to the three blade parts, selected as general for wind turbine blade structures: The root, the middle and the tip parts, according to Fig. 3.3. The root part of a wind turbine blade that is often the most complex. FE models of the root part can be characterized by high developing and computational costs relative to the middle and the tip parts of the blade.

Typically the root part of a wind turbine blade has fairly thick walls compared to the cross-section dimensions with extensive application of sandwich components. Yet, although the blade is a shell structure, accurate modeling of such thick-walls demands solid elements (e.g. SOLID185 by ANSYS or HEX20 by NASTRAN).

The thick walls can not be accurately represented by shell elements due to non-trivial shear stress distribution through the wall thickness.

In the tip part of a wind turbine blade, the wall thickness is generally small, the transverse shear is also lower and shell finite elements are adequate for modeling of the blade tip parts at the same time reducing the development costs and the total number of DOFs in comparison to the model where solid elements are used. The shell elements available typically include sandwich formulation for easier representation of sandwich structures in the FE models. However, problems can arise in the leading edge area due to the large curvatures. The shell elements have certain limitations upon the allowed maximum element curvatures and hence finer meshes have to be generated in the leading edge area.

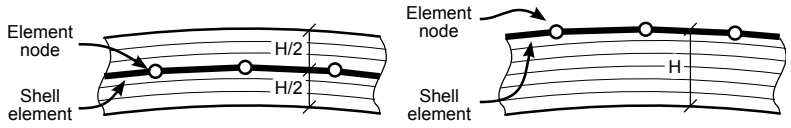

(a) Standard (b) Offset

Figure 3.6: Standard and offset formulations of shell finite elements for a laminate.

In a standard shell element formulation the nodes of the elements are placed in the wall mid-thickness plane, see Fig. 3.6(a). It can be a rather cumbersome task to calculate the correct mid-thickness nodal positions for a blade structure with variable wall thicknesses. The wall thickness variations can be caused, for example, by ply-drops in the layup or different thicknesses in the bonded adjacent walls. To significantly facilitate the FE model development process, a possibility for nodal offsets in the shell elements (Fig. 3.6(b)) can be used to ensure the nodal positions at the blade outer surface accurately defined by the blade airfoil. However, it was demonstrated by Laird et al. (2005) and later by Branner et al. (2007) and Dimitrov (2008) that this approach can lead to inaccurate predictions of the structure torsional stiffness. Laird et al. (2005) developed a special software called NUMAD to avoid the use of the offsets and to facilitate the pre-calculations of the mid-thickness nodal positions in wind turbine blade FE models.

The middle part of a wind turbine blade essentially consists of walls of moderate thicknesses, which can be at some areas rated as thick and at some areas as thin. Therefore, both solid and shell finite elements or their combination can be used here. Generally, combination of the two element types is a cumbersome task due to incompatibility of the nodal DOFs between them: solid elements typically have three DOF per node (displacements in three principal directions), while shell

elements have six (displacements and rotations). When such a combination takes place, certain modifications of the mesh or the layup has to be done and a great care has to be taken to avoid unintentionally applied restrictions to the involved DOFs.

Similar to the situation of curved shell elements covered above, the application of only solid elements in the middle part of a wind turbine blade can also become problematic in the leading edge region. Curved thin walls of the leading edge require significant refinements of the mesh and hence substantial increase in the total number of DOFs of a FE model.

3.4 Vestas blade section

A modified commercial wind turbine blade section studied experimentally (see chapter 2) is chosen as a subject for numerical investigation. The tapered and slightly pretwisted 8.4 meter section is cut from a 23 m wind turbine blade manufactured by Vestas Wind Systems A/S. The original blade is a lightweight composite structure designed with a nearly rectangular load carrying spar and the outer aerodynamic shape shell. The blade section root end (the cross-section closest to the blade root) can be seen in Fig. 3.7.

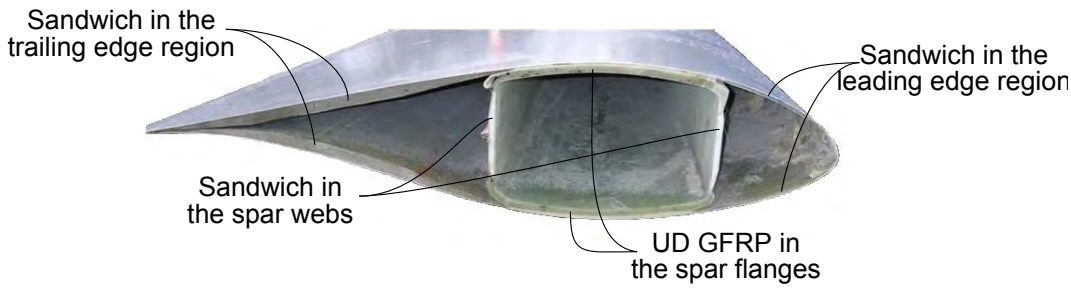

Figure 3.7: Root end of wind turbine blade section.

The load carrying spar of the blade is manufactured as a box beam with significant amount of UD GFRP material in the flanges, where the fibers are aligned with the blade pitch axis to provide high bending stiffness of the structure. For higher in-plane shear strength, the UD layers of the spar flanges alternate with thin GFRP layers where the glass fibers are arranged in a $\pm 45^{\circ}$ pattern (called biax). In contrast to the flanges, the spar shear webs are thinner and contain only biax layers. At the regions close to the blade section root, sandwich structure is introduced to the spar shear webs by placing a PMI foam core between the biax layers.

The outer shells of the blade section are sandwich structures with PVC core to increase resistance to the instability phenomenon known as compressive buckling. The thickest sandwich structures are placed at the trailing edge region and the thinnest at the leading edge region. Layup-wise, the outer shells are manufactured as combination of the layers, where the glass fibers are arranged in patterns of $+45°/-45°$ and $+45°/0°/-45°$ with respect to the blade pitch axis (called biax and triax accordingly). The pressure and the suction side outer shells are bonded to each other and to the load carrying spar by epoxy adhesive. The outer surface of the shells is covered by 1 mm thick gelcoat, see Fig. 3.7.

The original structure was modified prior to earlier experimental investigations, 2, where extra UD GFRP layers were applied to both pressure and suction sides of the blade section. The UD layers are of 4.4 mm thickness with the fibers biased by 25° with respect to the longitudinal (pitch) axis of the blade section. Before the application of the extra layers the original gelcoating was removed. The modified blade section is shown schematically in Fig. 3.8.

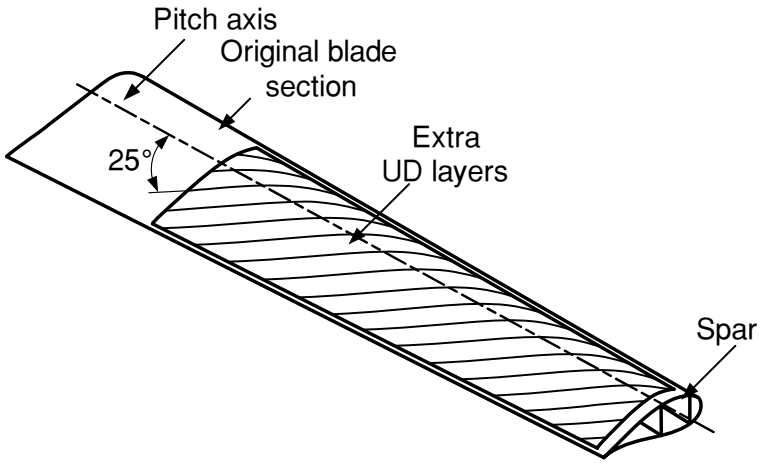

Figure 3.8: Modification of the blade section by applying extra UD layers on the pressure and suction sides.

According to the division of the entire wind turbine blade structure into three parts (Fig. 3.3), the blade section belongs to the middle part of moderate complexity level with moderate wall thicknesses. More details regarding the blade section geometry, layup and materials can be found in Appendix A. Additional information regarding the selection of the blade section and the modification procedures are given by Berring and Knudsen (2006).

3.5 FE models of Vestas blade section

A number of detailed 3D FE models of the original as well as the modified wind turbine blade section, that have been developed during several previous studies are considered here. The models use shell and/or solid finite elements, and different modeling techniques developed in several commercial software packages. Presently, the modeling techniques are classified in a simple manner and each approach is discussed. The earlier FE models were developed by Berring and Knudsen (2006), Branner et al. (2007) and Dimitrov (2008) and the reader is referred to these publications for more detailed description of the models.

Among all the developed FE models of the blade section, three model typesare highlighted:

- FE models with shell elements with nodal offsets
- FE models with shell elements of standard formulation (nodes placed at the wall mid-thickness)
- FE models with both shell and solid elements

3.5.1 FE models with shell elements with nodal offsets

FE models with shell elements with nodal offsets are the fastest and hence the cheapest for detailed 3D modeling of blades. The nodes in these models are offset from the wall mid-thickness and positioned at the blade outer surface, defined by the airfoil, see Fig. 3.9. The layup configuration is input layer-by-layer, e.g. using section input in ANSYS. Thus, no extra pre-calculations, or special considerations are required.

Laird et al. (2005) stated that the use of the nodal offsets, as implemented e.g. in SHELL181 finite elements in ANSYS, provides incorrect prediction of the structure torsional behavior. This problem proved to be independent on a FE solver, by replicating this blade section FE model in MSC, ANSYS and ABAQUS software packages by Dimitrov (2008). Further, he developed an extra blade section FE model, built of shell elements with nodal offsets and a material data input in form of stiffness matrix instead of the layer-by-layer input. The stiffness matrix input implies pre-calculations of the A, B and D matrices for each shell element, according to the Classical Laminate Theory. The nodal offsets introduced in the model

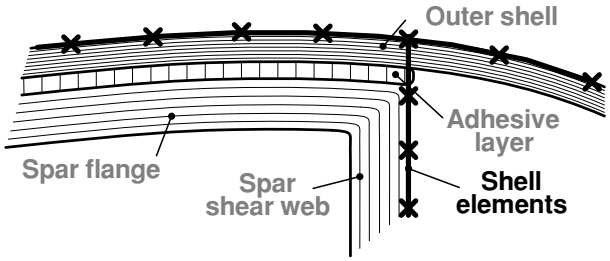

Figure 3.9: Example of junction of spar and leading edge of a blade, meshed using shell elements with nodal offsets.

are accounted in the pre-calculation of the mentioned matrices. It is demonstrated that the torsional behavior is predicted correctly when the matrix material data input is used, however, the reasons for that are still indistinct, as similar procedures as the ABD matrices pre-calculations are believed to be done by FE solvers in the case of layer-by-layer material data input.

3.5.2 FE models with shell elements of standard formulation

The second type of the detailed 3D FE models considered here is the FE models with shell elements with standard formulation, that is with the nodes placed in the wall mid-thickness. This modeling approach, when applied to the blade section, has several disadvantages related to complexifications of the development process. The disadvantages concern discontinuities of the mid-thickness surfaces in the blade cross-section planes where junctions of the walls of different thicknesses take place (see Fig. 3.10), and also discontinuities of the wall mid-thickness surfaces along the blade section due to the present ply-drops, see Fig. 3.9.

The first of the two discontinuities leads only to extra, often cumbersome, pre-calculations of the mid-thickness surface positions and introduction of rigid beam finite elements in the blade cross-section planes. However, it is demonstrated by Branner et al. (2007) that the second problem, in addition to introduction of extra rigid beam elements at the ply-drop positions (Fig. 3.11), leads to incorrect blade bending behavior predicted by the FE model, caused by these extra rigid elements. Nevertheless, the torsional properties seem to be accurately predicted by this modeling approach.

The FE models of the two types, described until now are developed using three different commercial FE software packages and consequently using different com-

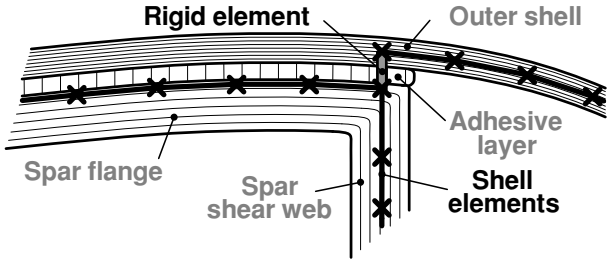

Figure 3.10: Example of junction of spar and leading edge of a blade, meshed using shell elements with nodes at the wall mid-thickness positions and extra rigid beam finite elements.

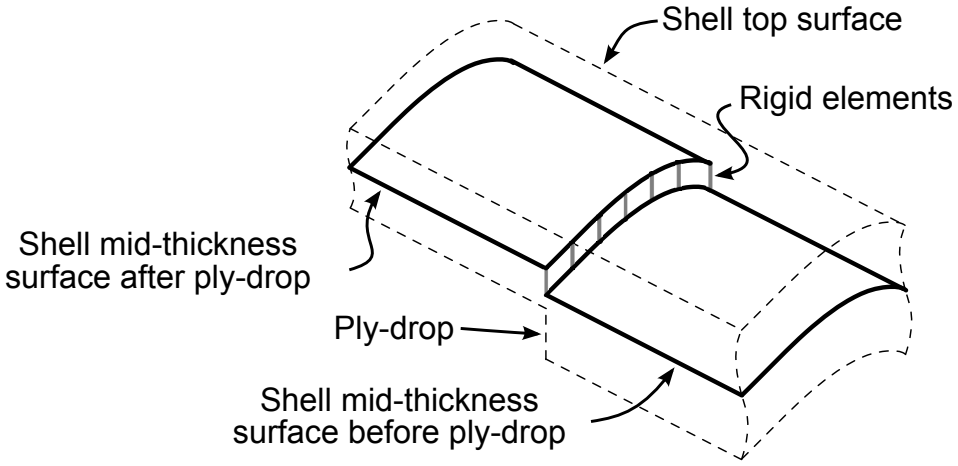

Figure 3.11: Example of rigid element connections in blade section due to a lengthwise ply-drop. The scale is distorted for more distinct picture.

mercial shell finite elements. The total number of DOFs is about 500,000 for all models.

3.5.3 FE models with combination of shell and solid elements

The last type of detailed FE models of the blade section is a FE model built of combination of solid and shell finite elements developed by Berring and Knudsen (2006). The model is built as an attempt to overcome the complexities and the related accuracy problems of the first two modeling approaches. Hereby, solid elements are used in the FE models to represent the core of the sandwich structure, adhesive and the extra UD GFRP layers of the modified blade section, while shell

elements are used to represent the sandwich face sheets and the GFRP shells, see Fig. 3.12.

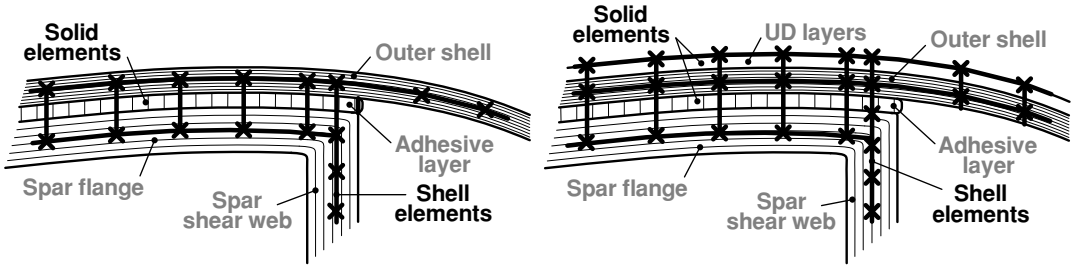

(a) Original blade section

(b) Modified blade section

Figure 3.12: Examples of junction of spar and leading edge of original and modified blade sections, meshed using combination of solid elements and shell elements with standard mid-thickness nodal placement. The adhesive layer is represented by solid elements with modified (increased) thickness.

The shell elements used in combination with the solid elements possesses standard formulation with the nodes placed at the wall mid-thickness surfaces. Therefore, special modifications are required for connection of the shell and the solid elements. The major modification was as an increase of the adhesive layer thickness together with a reduction of its stiffness. The adhesive stiffness properties were determined from the condition of keeping the modified adhesive layer contribution to the bending and torsional stiffnesses of the structure, estimated in a simple way, equal to the contribution of the original adhesive material. Details about the modification process can be found in Branner et al. (2007). This is definitely not a trivial task, making this type of FE models rather time consuming in development and with generally high potential of unknown effects to be added by such modifications.

The FE models built of combination of shell and solid elements generally demonstrated accurate prediction of global blade section response during the previous studies on the blade section. Using 8-node QUAD8 shell elements and 20-node HEX20 solid elements, the FE models developed in MSC software have 175 elements along the blade section length, 74 elements circumferentially in each cross-section, and 3 solid elements through the sandwich core an adhesive layer walls. The total number of DOFs is therefore around 3,500,000.

3.5.4 Overview of blade section FE models

The properties of the three considered FE modeling approaches are gathered in Table 3.1, where three parameters are evaluated: development complexity (corresponds to the development costs), approximate total number of DOFs (corresponds to the computation costs) and accuracy of the results.

Model type	Complexity	DOFs ca.	Accuracy
Shell, offsets	low	500,000	problems in torsion
Shell, standard	high	500,000	problems in bending
Shell/solid	very high	3,500,000	high

Table 3.1: Evaluation of detailed 3D FE models of a blade section.

It can be noticed from the table, that the models built of shell elements using offsets are rather straight forward to develop with lower number of DOFs and hence, the most attractive. Yet, it is known (see Hansen (2007)) that accurate torsion prediction might be essential for analysis of flutter – an aeroelastic instability phenomenon in modern large wind turbine blades. It is of a particular interest to perform a validation of these FE models against the experiments on the blade section subject to bending and torsion, see Chapter 2.

The FE models built of shell elements of standard formulation are more complicated to develop, although they can accurately predict the torsional behavior, but have problems with accurate prediction of its bending response. FE models built of combination of solid and shell elements are much more complicated to develop, but are capable of accurate prediction of the blade section global response.

3.6 Validation of blade section FE models

Validation of two FE models of the modified wind turbine blade section, representatives of the two modeling approaches – using shell elements with offsets and using combination of shell and solid elements – is presented in this section. The pure shell model is developed using ANSYS, while the second model is developed using MSC commercial FE code. The results of the models are brought to a single format and validated against the recent experiments on the blade section, presented in Chapter 2, where the blade section was subject to torsion. Additionally, to give a better overall picture of accuracies of the two modeling approaches, validation of the FE models of the original blade section is presented, where torsion load case is extracted by superposition of two bending load cases.

3.6.1 Boundary conditions and load application

FE models of the blade section are subject to clamped boundary conditions, implemented by constraining all degrees of freedom of all the nodes constituting the root clamp cross-section. Such boundary conditions do not correspond to the experimental support conditions, see discussion in Section 2.3.1, but they still represent the experimental setup.

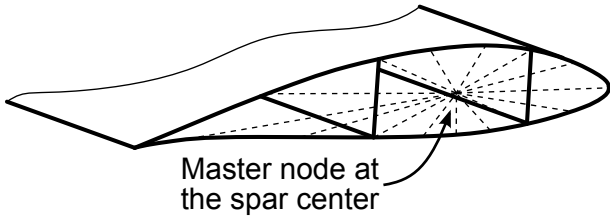

Figure 3.13: Scheme of a rigid connection with a master node at loaded cross-section.

To ensure smooth distribution of the loads and to avoid excessive local deformations at the blade section loaded tip, an approach similar to the one utilized in the experiments on the blade section is used in the FE models. That is a master node is created at the loaded cross-section spar center position with rigid connections to all the nodes of the cross-section. In the FE models built of combination of shell and solid elements developed in the MSC software, this is done by using MPC-RBE2 elements, while in the models built of shell elements, the rigid connections are created by using ANSYS command CERIG. The master node connections are shown in Fig. 3.13.

Three load cases equivalent to the cases studied experimentally are modeled: Flap-wise shear force bending, flap-wise shear force bending with torsion and pure torsion, see Fig. 3.14. The loads are applied to the blade section FE models through the created master nodes as a system of forces and torques statically equivalent to the system of forces applied to the blade section during the experiments. The shear force bending load case, Fig. 3.14(a), is implemented as a single force acting at the master node, while in the shear force bending with torsion load case, Fig. 3.14(b), the load is applied by means of an equivalent shear force and an extra torque acting at the master node. The torsion load case is implemented simply as a torque acting on the master node, Fig. 3.14(c).

In magnitudes, the loads applied to the blade section in the numerical models are equal to the experimentally applied loads. Those are: 4.0 kN forces in the two bending load cases and 2.78 kNm torque in the bending with torsion and the torsion load cases.

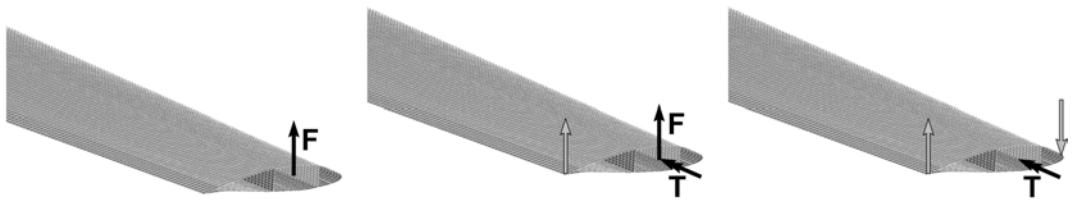

(a) Shear force bending (b) Shear force bending and torsion (c) Pure torsion

Figure 3.14: Load application to blade section in shear force bending - a, shear force bending and torsion - b, and pure torsion - c, load cases. Gray arrows - experimentally applied loads. Black arrows - statically equivalent loads applied in FE models through the created master node.

3.6.2 Results and discussion

Post processing of the FE model results is done according to the calculation algorithm developed during the experimental study (see Section 2.3.3). Bending displacements at the spar center positions and twist angles of eleven cross-sections evenly distributed along the blade section are calculated, and the results are reduced to the cross-section closest to the blade section root to minimize the effect of actual boundary conditions, see the discussion in Section 2.3.1.

The bending displacement and the twist results from the two bending load cases for the original blade section are shown in Fig. 3.15(a) and Fig. 3.15(b) accordingly. The results corresponding to the shear force bending case are plotted with solid lines, and the shear force bending with torsion results are plotted with dashed lines. Generally, there are only minor deviations between the numerical and the experimental results. Only the shell FE model with offsets demonstrated noticeable inaccuracy in prediction of the blade section twist in the shear force bending with torsion load case – ca. 30% tip twist error.

The bending displacement and the twist results from the torsion load case for the original blade section, obtained by superposition of the two bending load cases are shown in Fig. 3.16(a) and Fig. 3.16(b) accordingly. The results of the shell FE model with offsets can be clearly distinguished as bending displacements and twist angles, predicted by the model significantly deviate from the experimental values – ca. 25% error for the tip twist. According to the results for the original blade section, given on the two pairs of graphs until now, the problem of innacurate

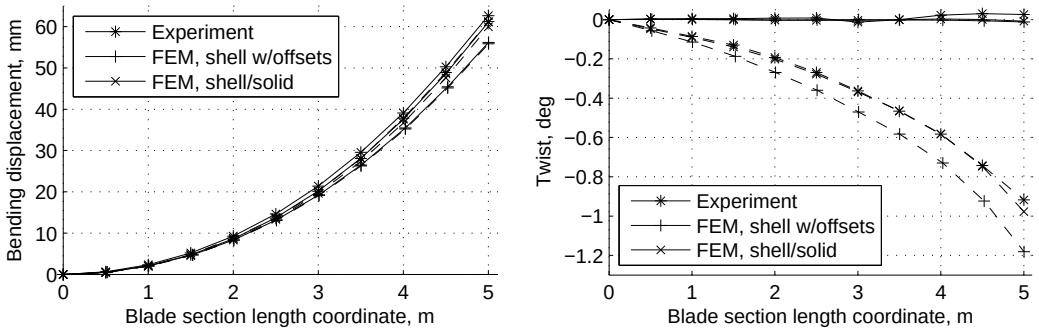

(a) Bending displacement (b) Twist

Figure 3.15: Flap-wise shear force bending and shear force bending with torsion load cases for the original blade section. Numerical and experimental results for bending displacement - a, and twist - b. Shear force 4 kN., torque 2.78 kNm.

prediction of the blade section twist as a response to applied torque, by the shell FE model with offsets, is clear.

For the modified blade section under the two bending load cases the results look very similar to the ones for the original blade section, see Fig. 3.17. The results for bending displacements are shown in Fig. 3.17(a). The tip twist error demonstrated by the shell FE model with nodal offsets in the shear force bending with torsion load case is around 16%, see Fig. 3.17(b). Note, however, that when the modified blade section is loaded by a single shear force applied at the spar senter, both FE models accurately predict the blade section twist, induced by bend-twist coupling.

When the modified blade section was subject to torsion, the shell FE model with offsets demonstrated the highest deviations of the twist angles from the experimental values, while the results of the shell/solid FE model agreed very well with the experiments, see Fig. 3.18. The bending displacements induced by bend-twist coupling are overpredicted by both FE models and possess rather high relative deviations, yet the obtained magnitudes for all the results are low (ca. 1 mm tip bending displacement for a 5 m blade section), so no solid statement on the accuracy can be done here, Fig. 3.18(a). The tip twist deviation for the shell FE model with offsets is ca. 22% with respect to the experiment – very similar to the results obtained for torsion of the original blade section, see Fig. 3.18(b).

For better overview of the results the difference between the numerical and experimental results for the tip bending displacements and the tip twist angles are listed in Table 3.2 for both FE models of each blade section configurations.

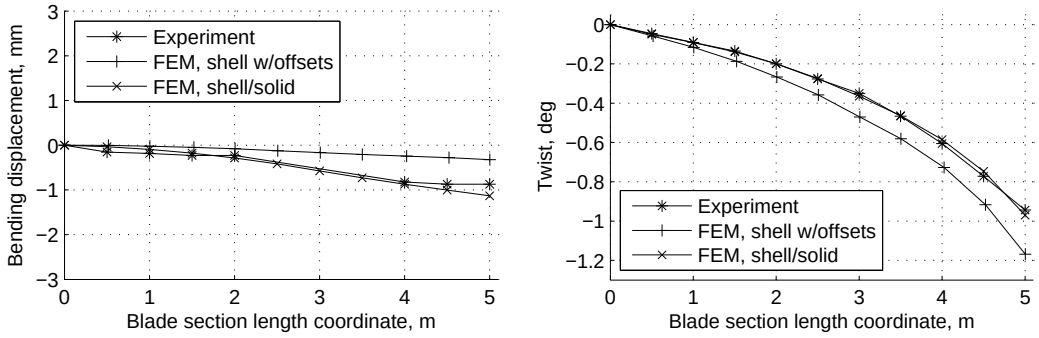

(a) Bending displacement

(b) Twist

Figure 3.16: Bending displacement - a, and twist - b, results for torsion load case for the original blade section by superposition of the results of shear force bending and shear force bending with torsion load cases. Torque 2.78 kNm.

Note, that the tip twist of the blade section under torsion load, overpredicted by the shell FE models with offsets, possess significant difference with respect to the experimental values of ca. 20-30%. In turn, the bending displacements are predicted by these models with nearly constant difference of ca. 9%. The results generated by the FE models built of combination of shell and solid elements are generally more accurate in comparison to the shell models with offsets.

3.7 Conclusions

Detailed FE models of modern composite wind turbine blade structures were examined in the present study. The development of the detailed FE models built of shell and/or solid finite elements was addressed as an approach for prediction of global wind turbine blade structural response.

A commercial wind turbine blade section was considered for a particular study. Several FE models of the blade section were discussed and two FE models of the wind turbine blade section – representatives of two most attractive detailed 3D FE modeling approaches, were validated against the latest experiments on the blade section to present a complete picture of performance of the blade section FE models.

Finally, attractiveness of the FE models built of shell elements with offsets in terms of development costs and requirements to the computational resources was

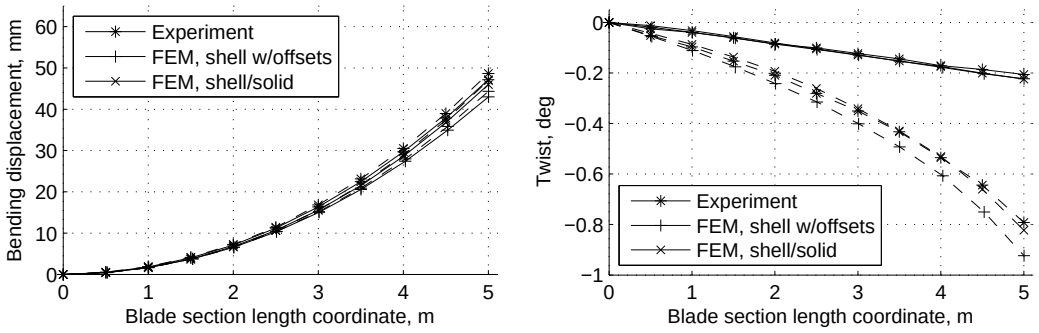

(a) Bending displacement

(b) Twist

Figure 3.17: Flap-wise shear force bending and shear force bending with torsion load cases for the modified blade section. Numerical and experimental results for bending displacement - a, and twist - b. Shear force 4 kN., torque 2.78 kNm.

demonstrated. However, a week point of the method, that is inaccurate prediction of the structure torsional response (20-30% tip twist discrepancy), essential for large blade structures was exposed as well.

The FE models built of shell elements with standard formulation, where the nodes are placed at the shell mid-thickness positions were found to be more expensive in development due to extensive use of rigid beam elements, introduced in the mid-thickness surface discontinuities. The problem of inaccuracy in prediction of global bending response of the blade section structure due to the rigid elements introduced into the model at the ply-drop positions was covered as well.

An example of combination of shell and solid finite elements was found to be of the highest development cost due to required non-trivial modifications of the FE model, that can potentially lead to unaccounted effects. However, it was demonstrated that this type of FE models is the most accurate in prediction of global blade section response.

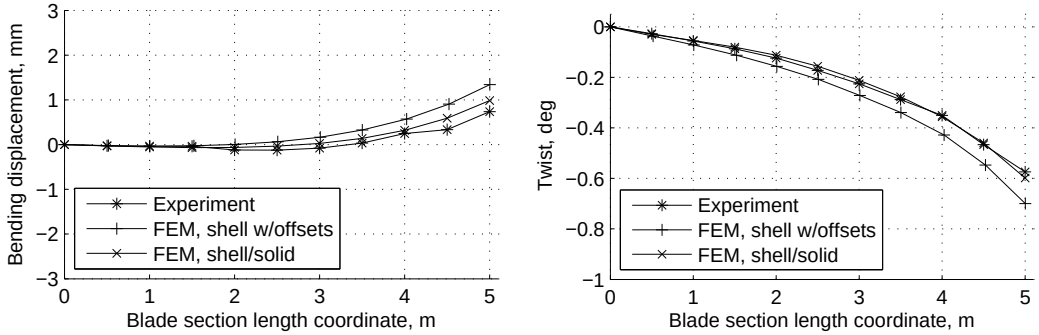

(a) Bending displacement

(b) Twist

Figure 3.18: Numerical and experimental results for bending displacement - a, and twist - b, for the modified blade section. Pure torsion with moment of 2.78 kNm.

		Original blade			Modified blade		
		Bending	Bending torsion	Torsion superp.	Bending	Bending torsion	Torsion
Shell w/offsets	bd	10%	9%	avg.	9%	9%	low
	tw	good	**29%**	**24%**	8.5%	**16%**	**22%**
Shell/solid	bd	2.5%	2%	low	2.5%	3.5%	low
	tw	low	6%	3%	8.5%	4%	4%

Table 3.2: Difference between experimental and numerical results for tip bending displacement (bd) and tip twist (tw) in three load cases for FE models of the original and modified blade sections built of shell elements with offsets and built of combination of shell and solid elements. Author's assessments "low" or "average" are placed, when low magnitudes (and ths high measurement error) of the measured values are observed.

Chapter 4

Validation of FE models of coupled composite beams

4.1 Introduction

The experimental investigation carried out on a commercial wind turbine blade section (see Chapter 2) demonstrated, that the blade section problem is too complex for a pure experimental study and several assumptions are required to treat the problem in a simple manner. The bend-twist elastic coupling effect in the blade section was demonstrated as the blade section bending response induced by the coupling in torsion. The obtained bending response was of small magnitudes and therefore subject to measurement uncertainties.

In a numerical study performed on the wind turbine blade section (see Chapter 3) the advantages of the FE models with shell elements were demonstrated for thin to moderately thick walls. However, some problems common for the shell FE models were found as well: low accuracy in prediction of the blade torsion response when nodal offsets are used in shell finite elements, and low accuracy in prediction of the blade bending response when rigid elements are used at the discontinuity regions due to ply-drops.

In view of the problems described above, uniform composite beams of simple geometries and layups are selected for a more detailed study of performance of the shell element based models. Detailed 3D FE models of three types, representative of several modeling techniques, are developed for each of the composite beam configuration. The results of the shell element based models are compared to the

results of the FE models built of continuum shell elements. The continuum shell finite elements possess similar geometry as volumetric elements, but perform as shell elements. Therefore, the use of continuum shell elements is expected to be a solution to the discontinuity problem common for FE models of wind turbine blade structures built of shell elements.

A set of composite beams of open (I-shaped) and closed (box-shaped) cross-sections was manufactured and tested to provide experimental data for validation of the developed FE models. The beam configurations are selected so that they demonstrate the bend-twist coupling effects. Several principal fiber directions are chosen for the beam flanges for introduction of different bend-twist coupling effect magnitudes.

Chandra and Chopra (1992) showed that restraining of the cross-section warping can lead to 630% increase in torsion stiffness especially for composite beams of open cross-sections. Therefore, particular attention is paid to this problem in the present study and the effects of restrained warping in composite beams are studied both numerically and experimentally.

A special test setup was built to carry out testing of the composite beams. Clamped boundary conditions are imposed to the composite beam specimens and accurate application of torsion and bending loads is done by utilizing an advanced servo-hydraulic system. Two Digital Image Correlation (DIC) systems are used for 3D measurements of deformations of the beam specimens. One of the systems, complemented with an optical system for spot measurements, is aimed for the global beam response measurements, while the second system is specially dedicated for the measurements on cross-section warping deformations.

4.2 Problem definition and objectives

High attractiveness of FE models built of shell elements for study of the bend-twist coupling effects in composite beam structures was demonstrated during the numerical analysis of a commercial wind turbine blade section presented in Chapter 3.

When shell finite elements are used according to the standard formulation, the element nodes are placed at the wall mid-thickness position (Fig. 4.1(a)). Modeling of a ply-drop requires introduction of rigid elements for connection between the two neighbor mid-thickness planes disconnected due to the ply-drop, see an

example in Fig. 3.11 in Section 3.5.2. It was demonstrated by Branner et al. (2007), that the usage of rigid elements due to ply drops along a wind turbine blade structure leads to underestimation of the blade bending stiffness.

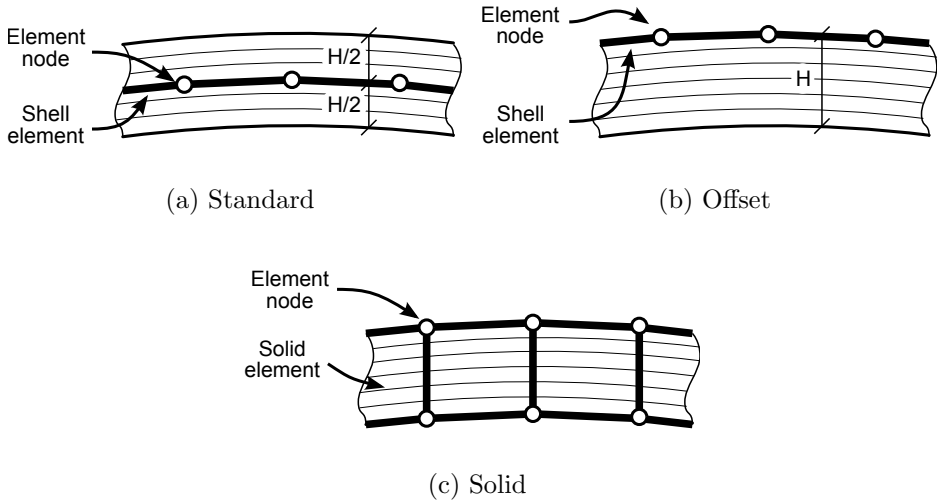

(a) Standard

(b) Offset

(c) Solid

Figure 4.1: Meshing a laminate with shell elements without nodal offsets - a, shell elements with nodal offsets - b, and with solid elements - c.

Another developing method implies utilization of shell elements that have the nodes offset to one of the wall surfaces, see Fig. 4.1(b). This method generally requires no extra rigid elements to be introduced to a FE model as no discontinuities occur, and thus, much less development efforts. Malcolm and Laird (2005) and Branner et al. (2007) demonstrated that the use of shell elements with nodal offsets when modeling thin-walled beams and wind turbine blades leads to underprediction of the torsional stiffness, so that the structure twist response to torsion is overpredicted by 20-30%.

The utilization of solid elements (Fig. 4.1(c)) in combination with shell elements in such FE models generally solves the problems of discontinuities and inaccuracies, but instead, it leads to a more complicated meshing, much larger total number of DOFs and often requires complicated modifications of the FE model in order to generate accurate connections between shell and solid finite elements.

For further more detailed investigation on performance of the FE models built of shell elements with and without nodal offsets, a set of composite beams of simple geometries and layups is considered. The beams possess uniform cross-sections with straight walls, simple symmetric layups and bend-twist coupling of different magnitudes. Open (I-shaped) and closed (box-shaped) cross-sections are selected

as representatives of common wind turbine blade load carrying spar designs (cf. Fig. 3.5). The maximum wall thickness to cross-section size ratio t/h is selected of max. 0.25 – similar to the blade section studied previously, see chapters 2 and 3.

It is of particular interest to investigate the performance of FE models built of shell elements without offsets for such simple composite beams. The models will have no extra rigid elements along the beam lengths due to the absence of ply-drops and therefore should have no problems with accurate prediction of the beam bending responses. Another goal is to study the accuracy of the torsional stiffnesses predicted by the FE models built of shell elements with offsets.

Accuracy of the FE models built of continuum shell finite elements (represented by SOLSH190 element in ANSYS) is of a particular interest of the present study. The continuum shell elements combine the geometry of solid elements (Fig. 4.1(c)) and performance of shell elements, and thus can be used to overcome the problem of discontinuities in FE models of wind turbine blades due to ply-drops. Therefore, the beam FE models built of continuum shell elements are to be developed and their performance is to be studied.

To validate the results of all the developed models, a set of composite beams is to be selected for manufacturing and testing. For evaluation of the accuracy of the developed FE models in predicting of complex bend-twist coupled response of the composite beams, torsion and bending are chosen as main load cases to be implemented experimentally to test the beams clamped at one end.

The torsion load case implies a torque applied at the beam end to generate constant torque along the beam, so that all the beam cross-sections experience equivalent torsion loading conditions. Similarly, in the bending load case, a bending moment is applied at the beam end so that all the beam cross-sections experience equivalent bending loading conditions. Response of the beams is to be measured in terms of bending displacements along the beam centerline and twist of the cross-sections (considered rigid in-plane) using the algorithm developed in Section 2.3.3.

According to the results of the study by Choi and Horgan (1977), where slow decay of the end effects in the anisotropic materials is demonstrated, the response of the tested composite beams can be affected by the boundary conditions. An example of such effect was studied e.g. by Chandra and Chopra (1992) where the effect of restrained warping on torsional behavior of composite beams was experimentally demonstrated and significant increase in torsion stiffness of open cross-section composite beams due to restrained warping was revealed.

Warping corresponds to the out-of-plane deformations of the beam cross-section which typically occurs when the beam is subject to torsion, see Fig. 4.2. Warping effects in thin-walled beams is covered by Vlasov (1961). The behavior of the composed beams addressed in the present study can be potentially affected by the warping restrains imposed by the clamped boundary conditions (Vlasov's torsion). Therefore, the numerically predicted warping deformations along the beams are to be investigated and validated against the warping deformations measured experimentally to ensure equivalent warping conditions in FE models and the real composite beams.

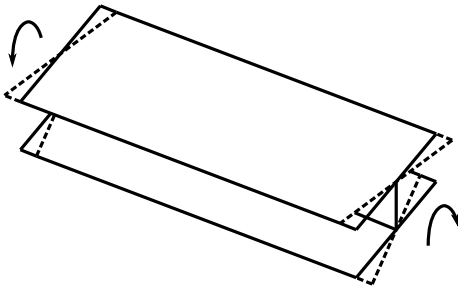

Figure 4.2: Warping in an open cross-section uniform beam. Warping deformations are showen by dashed lines, beam twist deformation is reduced to emphasize warping.

A cross-section in the mid-length position of the beam specimen is selected for investigations on the warping deformations. Here the end effects from the clamped beam root and the load clamps at the beam end are expected to be minimal (situation closest to St. Venant's free warping torsion), and thus, warping amplitudes and possible deviations between the numerical and experimental results are expected to be the highest.

4.3 Composite beam test specimens

Test specimens of simple geometries are addressed in the present study. Two basic cross-section shapes: Box- and I- shapes, Fig. 4.3 are selected for the composite beams as cross-sections similar to common designs of the load carrying spar in wind turbine blades. Only symmetrical layups are considered for simplicity.

For easier manufacturing process, all the beam specimens are designed as combinations of only two components bonded together. The first component is a UD flange plate, and the second is a C-profile shear web with $\pm 45^{\circ}$ layup (biax), see

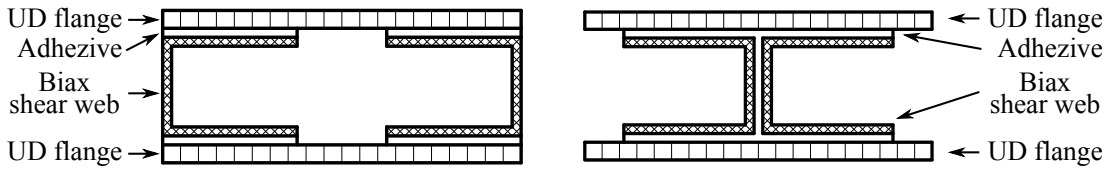

(a) Box-beam cross-section (b) I-beam cross-section

Figure 4.3: Two cross-section types of composite beam specimens. Box-shaped - a, and I-shaped - b.

Fig.4.4. Both box- and I-beam specimen configurations are composed as combinations of these two components. The biax shear webs are the same for all the specimen configurations, and only the UD flanges can be different by selecting the fiber orientations with respect to the beam longitudinal axis for introduction of the bend-twist coupling effects. Such approach allowed for easier, cheaper and faster manufacturing process and as a consequence larger number of specimens available for testing.

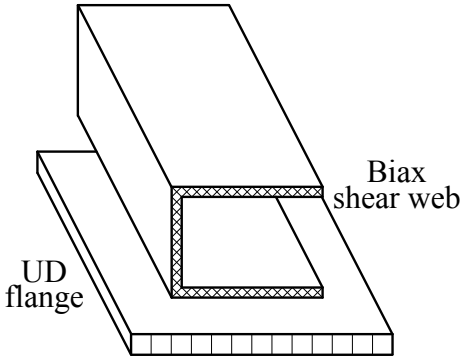

Figure 4.4: Basic components of composite beam specimens.

Glass-fiber reinforced plastic (GFRP) is chosen as the main material for the composite beams. Both the UD flanges and the shear webs are manufactured from prepreg GFRP materials. Epoxy adhesive is used for bonding of the components.

The final dimensions and the layup for the chosen cross-sections are determined based on the results of an iterative process where a number of constrains have to be fulfilled:

- A four-column testing machine is taken as a foundation for the experiments and thus, the specimen lengths is limited to approx. 1 m. To minimize the

end effects, the cross-section dimensions are limited to 100 mm in width to keep a ratio of 1/10 between the beam width and length. This is dictated by the effects of restrained warping and is a common practice in definition of beams, see e.g. Song and Librescu (1993).

- Maximum and minimum bending and torsional stiffnesses of the specimens have to are limited from above in order to comply with limitations of the load application system and to ensure large enough beam deformations for accurate measurements during the tests.

- Three configurations of the UD flanges with different fiber directions are to be selected for introduction of the bend-twist coupling effects to the composite beams. The basic configuration is chosen as 0° UD fiber directions, corresponding to zero coupling configuration.

To solve this design problem, a preliminary numerical analysis on the composite beams is performed using FE models built of shell elements for each of the beam configurations. The stiffness constrains mentioned above are ensured by applying the maximum allowed loads to the beams and controlling the distributions of bending displacement and twist along the beam. The fiber directions in the beam UD flanges are selected according to a simple evaluation of the bend-twist coupled response of the beam, that is as a ratio between the generated bending angle and the twist angle at the tip of the beam loaded by a tip bending moment. Details on the constrains are given in the following sections, where the entire test setup is presented.

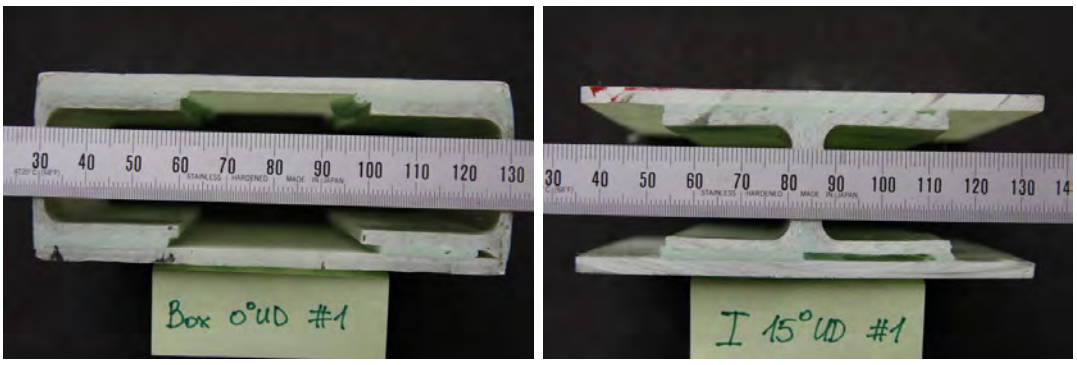

(a) Box-beam (b) I-beam

Figure 4.5: Composite beam specimens. Box-beam - a, and I-beam - b.

Based on the results of the iterative process performed using the preliminary beam FE models mentioned above, the composite beam dimensions are determined as: 1100 mm x 100 mm x 40 mm with 3.5 mm UD flange thickness and 2.5 mm shear web thickness. Detailed sizing of the final beam specimens is given in Appendix B. Material data for the following detailed FE models are obtained in a series of material tests performed on specimens made from beam segments left after the final beam length adjustments. Information about the material tests and the material data is detailed in Appendix C.

Three symmetrical layups are selected for each of the cross-section type. The chosen layups have the fibers in the UD flanges biased by 0°, 15° and 25° from the beam longitudinal axis. To account for potential specimen damage due to low in-plane shear strength of the UD flanges, two replicate specimens of each beam configuration were manufactured. Thereby, twelve composite beam specimens were manufactured in total. Photos of the manufactured beams are shown in Fig.4.5.

4.4 FE models of composite beams

Three FE models were developed in ANSYS v11.0 for each composite beam configuration:

1. FE model built of shell elements with standard mid-thickness nodal positions
2. FE model built of shell elements with nodal offsets
3. FE model built of continuum shell elements

For the FE models built of shell elements, layered 4-node SHELL181 elements with 6 DOFs per node (3 translation and 3 rotations) were used and layered 8-node SOLSH190 with 3 translation DOFs per node for the FE models using continuum shell elements. The material orientation data is input into the models layer by layer using SECTION format. Only linear analysis is considered in the present study due to expected small deformations and strains.

4.4.1 FE model built of shell elements

FE models of composite beams were built of shell elements of standard formulation. In these models all the nodes were placed at the wall mid-thickness, so that a

problem of mid-thickness surface discontinuity, typical for this type of FE models, occured. Four points of the wall mid-thickness discontinuity were singled out for each cross-section shapes at the adjoining of the walls of different thicknesses (the edges of the shear web C-profiles), see Fig. 4.6.

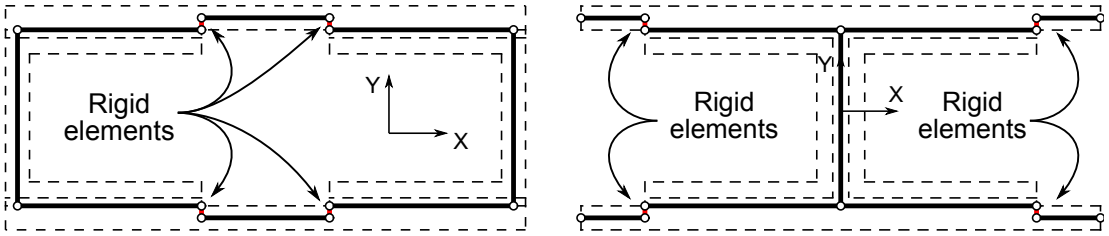

(a) Box-beams (b) I-beams

Figure 4.6: Cross-section meshing using shell elements without offsets. Box-beam - a, and I-beam - b. Nodes are placed along the black solid lines.

The wall mid-thickness positions were pre-calculated and rigid beam elements MPC184 were introduced for connection of the adjacent mid-thickness surfaces on node-by-node basis. The rigid elements were used for all cross-sections along the beam length. Generally, this is a tedious task, but for the structures with such simple geometries like the modeled beams it can be done automatically by using scripts that are typically supported in commercial FE solvers. Placement of the rigid elements along the beams is illustrated in Fig. 4.7.

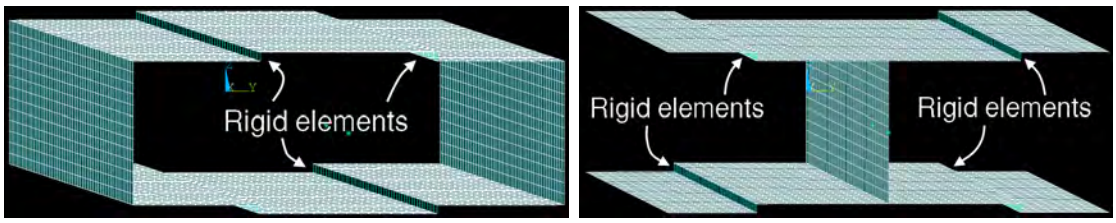

(a) Box beam (b) I beam

Figure 4.7: Rigid elements along box-beam, (a), and I-beam, (b), FE models built of shell elements.

4.4.2 FE models with shell elements w/offsets

In the FE models with shell elements with offset nodes no pre-calculations of the wall mid-thickness positions are required and the development process mainly concerns building the simple box- or I-shaped geometries with the layer-by-layer material data input. The location of the nodes is shown in Fig. 4.8.

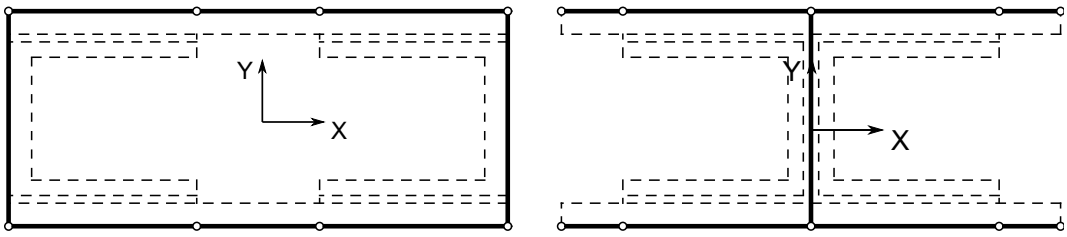

(a) Box-beams (b) I-beams

Figure 4.8: Cross-section meshing of box- (a) and I- (b) cross-sections using shell elements with offsets. Nodes are placed along the black solid lines.

4.4.3 FE model with continuum shell elements

The last type of the FE models is built of continuum shell finite elements. Full spatial geometries of the composite beams are reconstructed in the models, see Fig. 4.9. Only one finite element is used to model the UD flange thickness and shear web. The nodal positions are pre-calculated based on the cross-section geometries and layups, which is a typical task for detailed FE models built of volume elements.

4.4.4 Boundary conditions and convergence study

Only clamped boundary conditions are considered so that in the FE models one of the beam ends is clamped by constraining all DOFs for all the nodes of the cross-section. The loads are applied in accordance to the experimental setup described in the next section. In-plane rigid cross-sections are created using CERIG command in ANSYS to represent the so called "load clamps" attached to the beam specimens for load application during experiments. The loads are applied to the master nodes of the rigid cross-sections, placed in the center of symmetry of the cross-section.

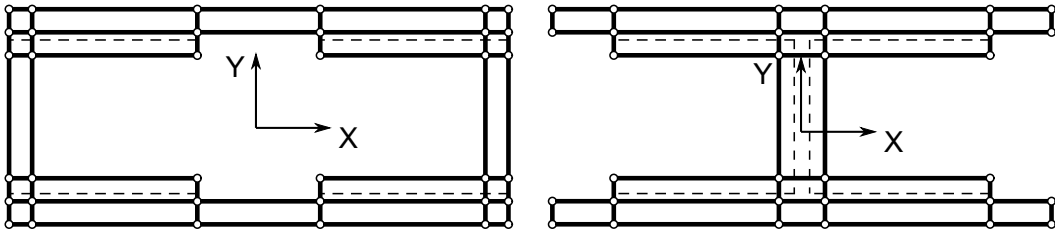

(a) Box-beams (b) I-beams

Figure 4.9: Cross-section meshing of box- (a) and I- (b) cross-sections for continuum shell FE models. Nodes are placed along the black solid lines. Beam original geometry is designated by dashed lines.

The meshing parameters for all the FE models are determined based on a convergence study. The convergence criterion is taken as 1% deviation of the bending displacement and twist angle at the tip of the beams between successive mesh refinment steps. The study is performed for both bending and torsion applied to the beams. According to the results of the convergence study, ca. 150 elements along the beam length and ca. 40 elements along the cross-section width are required. Therefore for all the developed FE models the elements are selected as rectangles with the sides in the cross-section plane of about 2.5 mm.

4.5 Test setup

A detailed description of the test setup is given in this section. The section is splitted into six subsections, where each of the them is devoted to a separate part of the setup such as e.g. DIC measurement system, which the author found important to present in details.

4.5.1 Test rig

A four-column MTS 810 testing machine is chosen as a test rig foundation for the experiments on composite beams, see Fig. 4.10. It has a main vertical actuator mounted on the crosshead that could be fixed at any height along the four guide columns. A strong foundation of the testing machine is used for mounting of additional actuators and necessary instruments. To maximize the distance between

the main vertical actuator and the testing machine foundation, and thus to maximize the beam length, the crosshead is fixed in the uppermost position. The beam specimens are mounted on the main actuator and placed vertically.

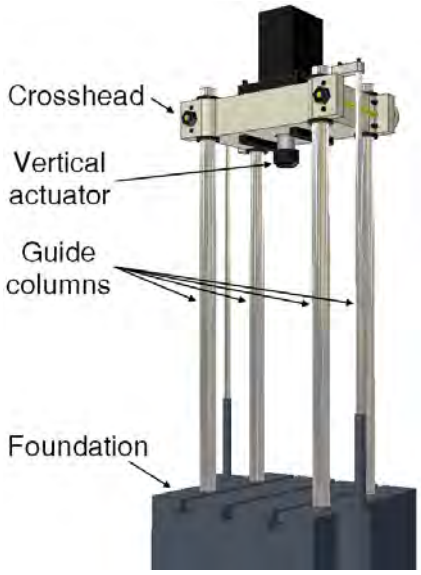

Figure 4.10: 3D model of MTS 810 four column testing machine.

The main vertical actuator is capable of applying vertical compressive or tension load while the required tip forces are applied to the beam specimens by two compact powerful hydraulic actuators, mounted on the testing machine foundation. All three actuators provide their current position and force signals through the position sensors (LVDTs) and the force transducers (load cells) mounted on them, so that they are all simultaneously controlled by a single MTS controller, which has a possibility of logical actuator interconnections for implementation of complex load cases.

According to the chosen test setup, the compact hydraulic actuators generate the required load cases by applying off-axis forces to the composite beam specimens. In such load cases the loads applied to the specimens are directly transmitted to the piston of the main vertical actuator. To avoid overloading and damage of the vertical hydraulic actuator and the force transducer mounted on it by direct application of high bending moments, a special off-axis load protective system was designed.

4.5.2 Off-axis load protection system

The problem of off-axis loading of the main vertical actuator is defined as follows:

1. Bending moment applied to the vertical actuator piston and the force transducer mounted on it should be minimized,
2. The size of the protective setup is to be as small as possible to avoid significant reduction of the beam maximum length;

A solution was found in form of two simple supports created for the vertical actuator piston. The simple supports were provided to the piston extension mounted after the attached load cell. A scheme of the solution is shown in Fig. 4.11, where the vertical actuator piston and the mounted beam are placed in horizontal position.

In the unprotected test setup the bending moment $M = Fd$ applied to the beam as a couple of forces F, acts to the actuator piston and the load cell. This is shown in Fig. 4.11(a) in form of the bending momemt distribution diagram. The simple supports introduced in the protected setup generate a reaction bending moment $M_R = -Rd_R = -M$, see Fig. 4.11(a), and thus prevent the distribution of the applied bending moment M after the protective setup.

To provide reaction forces high enough for protection of the actuator piston, the simple supports have to be at least as stiff as the piston itself, and have to ensure good reliable contact to the piston extension. Therefore, the simple supports are implemented as four steel bars of adjustable length mounted on the testing machine guide columns. The resction force is thus provided by the guide columns and a good contact between the columns and the piston extension is provided by adjusting the bars.

The adjusting bar consists of two threaded pins and a steel tube with two inner threads, see Fig. 4.12. One of the threaded pins has a left-hand thread while another one has a right-hand thread. The threaded tube has both threads inside - half of its length for each thread. When the pins are screwed into the tube, the length of the whole adjusting bar can be tuned by turning the threaded tube.

Due to a significant play in the threads and no space available for lock-nuts, the adjusting bars work reliably only in one of the load directions at a time: either in tension or in compression. Nevertheless, it is enough for robust operation of the protective setup.

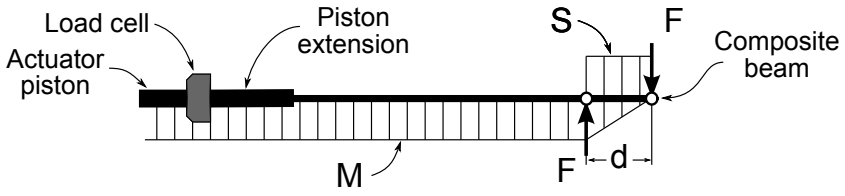

(a) Unprotected

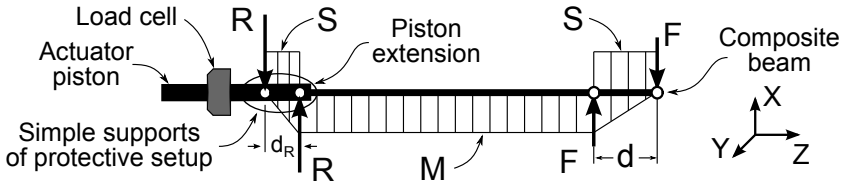

(b) Protected

Figure 4.11: Off-axis load unprotected (a) and protected (b) setups with load diagrams in bending load case. S - shear force, M - bending moment. F - applied forces, R - reaction forces

Figure 4.12: Steel adjustable bar for simple support

Consider one of the simple supports (Fig. 4.13) in the horizontal plane XY. An in-plane force F applied at the simple support can be considered as a system of two forces F_x and F_y – projections of the original force F. When properly adjusted (that means a contact is ensured between the bar and the piston extension) each of the reaction force projections is provided by at least two adjusting bars being under compression. Thereby, the four adjusting bars of the simple support can be divided into two primary (under compressive load) and two secondary bars (under tensile load, shown in gray on the Fig. 4.13). The primary bars always provide the required reaction force, while efficiency of the secondary bars is questionable due to the play in the treads and can be considered as poor.

The adjusting bars are mounted at the testing machine guide columns by mean of simple clamps and a specially designed steel connection plate with bronze friction bearing is used as an interface between the bars and the piston extension, see Fig.

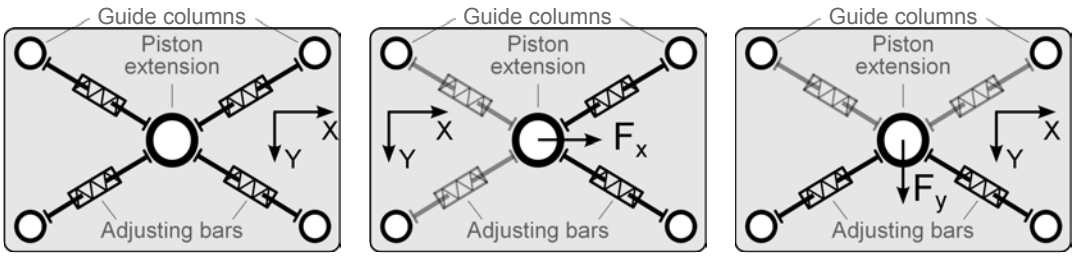

(a) Unloaded (b) Loaded in X direction (c) Loaded in Y direction

Figure 4.13: Scheme of horizontal cross-section of protective setup simple support. Top view. Three states are shown: Left – unloaded, center and right – the support is loaded by two principal force projections. Primary adjusting bars are in compression and shown in black, secondary - in tension and shown in grey.

4.14. The soft bronze bearing is manufactured together with the piston extension and the connection plates to ensure a very small gap between them. The gap is filled by a fine grease for good contact between the surfaces. For significant simplification of the protective setup assembling and adjusting, the bronze friction bearings of the two simple support connection plates are made as a single-peace bronze tube.

A 2D FE model of the connection plate is developed to evaluate maximal stress levels, see 4.14. The boundary conditions are defined as simple supports for the holes to which the adjustment bars are connected. The loads are applied to an appropriate half-circle of the central hole in form of distributed pressure varying linearly from zero at the edges to maximum value at the middle of the half-circle. The integrated value of the distributed load is equivalent to a chosen nominal value of 20 kN. As it can be noted from the figure, a number of holes is made in the connection plates for mounting purposes. The biggest four holes are made for reduction of the final plate mass.

For easier assembly, setup and adjusting of the protective setup, the two connection plates are tightened together by pins at each of the four corners. Thereby, the two plates are made as a single stiff assembly. To support the protective setup weight, four steel so-called “weight bars” are mounted to the connection plates assembly. The bars link the lower connection plate with the testing machine guide columns.

The final dimensions and operational parameters of the test setup and the beam specimens are determined in an iterative process, where such parameters as beam working length (free of boundary conditions and load calmps), maximal load levels

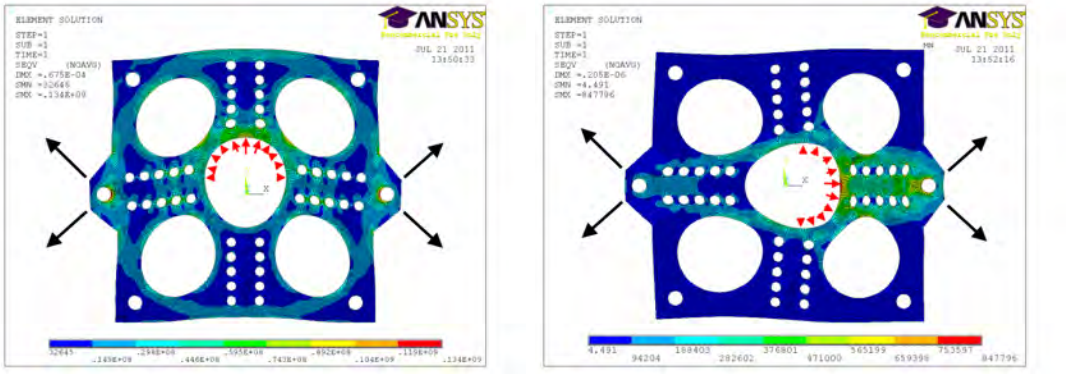

(a) (b)

Figure 4.14: Results of FE calculations of steel connection plate. The plate is loaded by a 20 kN force distributed along a half of the central hole as pressure (shown as red arrows) in the vertical (a) and horizontal (b) directions. The black arrows designate connections to the adjusting bars.

applied to the beam, geometry of the protective setup (connection plate thickness, bronze bearing diameter, adjusting bar length, etc.) and other parameters are considered as variables. A safety factor of at least 2 is ensured for the connection plates and the adjusting bars. The results of the iteration process are gathered in Table 4.1. Thus, the developed test rig is capable of providing 1.0 kNm bending moment to a beam specimen without damaginng the vertical hydraulic actuator.

Table 4.1: Off-axis load protection setup parameters

Parameter	Value
Max. shear force in shear force bending load case	1.0 kN
Max. moment in bending load case	1.0 kNm
Length of the beam specimen (free of clamps)	0.765 m
Distance between the connection plates	0.11 m
Connection plate thickness	10 mm
Max. horizontal reaction force in simple supports	20 kN

A simplified 3D drawing of the final design of the protective setup is shown in Fig. 4.15 and a photo of the protective setup mounted on the testing machine is shown in Fig. 4.16. All the bars attached to the guide columns are fixed by mean of

column clamps tightened by bolts. Strengths of the column clamps are evaluated by FE modeling, details of which are omitted here.

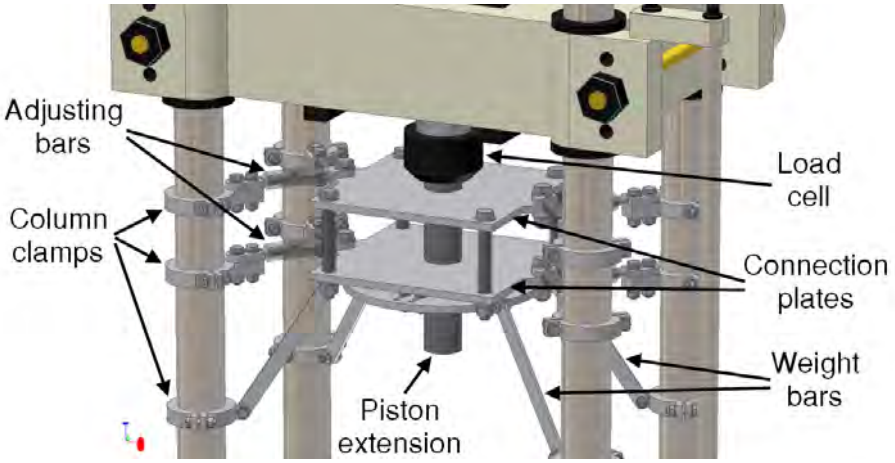

Figure 4.15: Protective setup on a four-column testing machine. Simplified 3D CAD model.

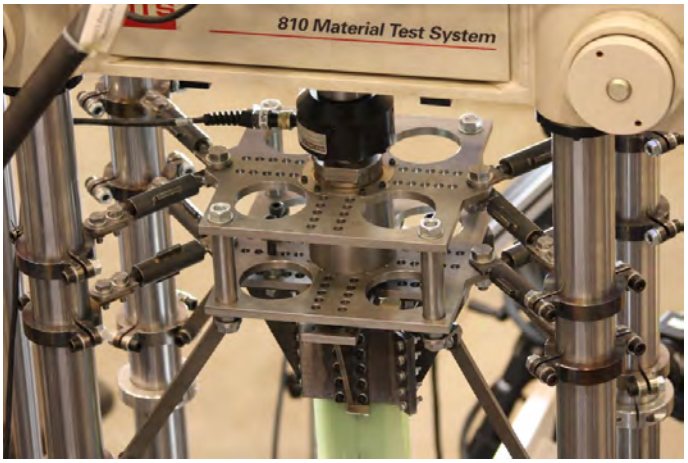

Figure 4.16: Protective setup on a four-column testing machine. Photo of the protective setup with mounted beam.

4.5.3 Specimen mounting

A special mounting system was designed for application of clamped boundary conditions to the composite beam specimens, see Fig. 4.17. The system consists of a steel clamp rigidly mounted on a beam specimen, a steel cross serving as an interface to the vertical actuator extension and four steel corners for connection of the clamp to the cross.

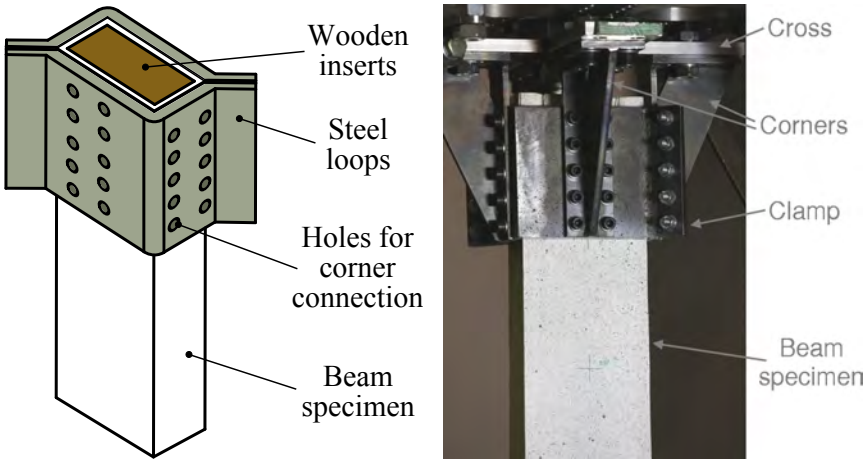

(a) (b)

Figure 4.17: 3D drawing (a) and a photo (b) of beam mounting at the piston extension.

The steel cross (partly shown in Fig. 4.17(b)) is 10 mm thick and has a hole in its center, through which it is mounted on the piston extension by a massive bolt screwed into a thread in the piston extension. The cross itself has a set of holes at each of its four parts for connection to the clamp by four corners.

The steel clamp ("root clamp") is designed as a pair of tightened steel loops mounted on the beam specimen and strongly tightened by twelve small bolts along the clamp, see Fig. 4.17(a). For protection of the beam specimens against damage due to overtightening, wooden inserts are glued inside the beams. The root clamp length is chosen to be 100 mm as an optimal value: A longer clamp would reduce the specimen length, and a shorter clamp would introduce high stresses at the beam end. The mounting system of the real setup can also be seen in Fig. 4.16.

As the main vertical actuator cannot restrain the beam root twisting in torsion, the beam specimens are mounted to the cross by long bolts passed through the

holes of both connection plates of the protective setup. Thereby, the root twist is constrained by the connection plates.

4.5.4 Load application

Two load cases – bending and torsion are applied to the beam specimens by two compact hydraulic actuators through the load clamps mounted on the beams, see Fig. 4.18. In the bending load case the actuators are attached at the mid-width of the load clamps, which corresponds to the beam cross-section center of symmetry. Two forces F are applied in opposite directions, so that with a distance $d_M = 0.170$ m between them they produce a bending moment $M = Fd_M$. For torsion the two actuators are attached to the tip load clamp through the handles, described previously. With the distance $d_T = 0.37$ m between the actuators, equal forces F acting on the handles produce a torque $T = Fd_T$. The load clamps are depicted in Fig. 4.19(a).

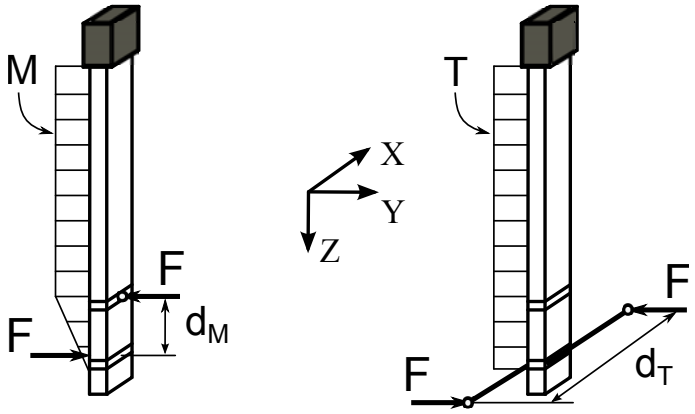

Figure 4.18: Load application to composite beams. Left – bending, right – torsion load case. M – bending moment distribution, T – torque distribution.

Special "forks" are mounted on the handles for connection to the compact hydraulic actuators. To avoid unwanted moments applied by the hydraulic actuators, they are connected to the forks by mean of spherical joints, see Fig. 4.19(b). A 3D drawing and a picture of the test rig with mounted beam specimen can be seen in Fig. 4.20.

Due to absense of hydraulic service manifolds (HSM - a mechanism for emergency oil flow cut off) on the two compact hydraulic actuators, it was not safe to operate them under load control. Instead, displacement control is used, where both

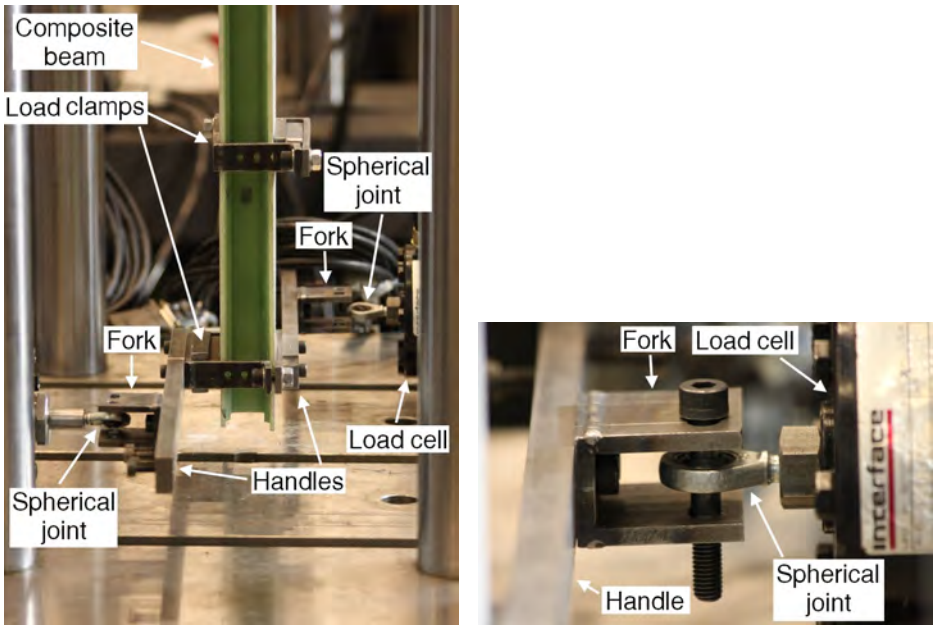

(a) Tip clamps on I-beam and handles for torsion load application.

(b) Spherical joint at the clamp for load application

Figure 4.19: Load application to beams. Load clamps and handles - a, and spherical joints - b.

actuators are operated manually through the hydraulic system controller. Thus, the required moments are applied by providing small displacement actuator movements and and the same time monitoring the load on both actuators. Similar load application was implemented in the experiments on a wind turbine blade section, see Section 2.3.2.

Magnitudes of the loads applied to the composite beams are mainly determined by the beam bending and twist responses that can be accurately measured by the measurement systems used in the experiments. For instance, the box-beams with the 25° UD configuration (the fibers in the UD flanges are biased 25° with respect to the beam axis) are expected to possess the highest torsion stiffness, while the 0° UD I-beams – the least, therefore the 25° UD specimens require higher torque to achieve measurable twist angles, than the 0° UD. The applied moments are listed in Table 4.2.

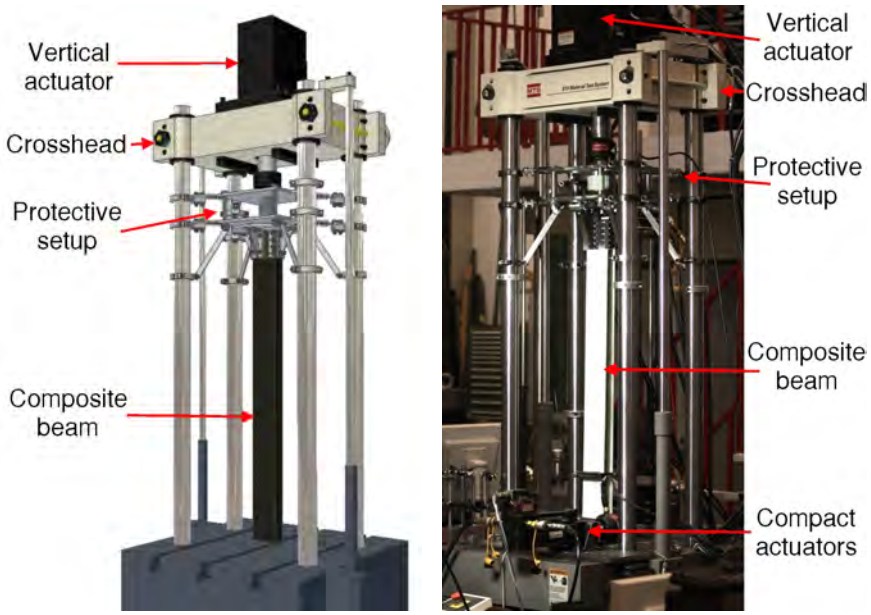

(a) (b)

Figure 4.20: 3D drawing and photo of test rig with mounted beam specimen.

Table 4.2: Moments (kNm) applied to composite beams

	Box-beams	I-beams
Bending	0.4	0.4
Torsion	0.2	0.01

4.5.5 DIC measurement systems

Two Digital Image Correlation (DIC) systems ARAMIS are used in the present test setup for accurate 3D measurements on the composite beams, see GOM (2008) for principles of the DIC measurements and general system parameters. The first DIC system is assigned for full-scale 3D displacement field measurements on one of the flanges of the beams. The system is equipped with two 4-megapixel digital cameras attached to the ends of a 0.5 meter bar. The cameras have lenses of 20 mm focal distance, providing wide angle of view and possibility to cover the entire beam specimen. For better resolution of the measured data, the camera setup is tilted about $30-40^{\circ}$ to fit the beam specimen into the snapshot diagonal. This increases the number of pixels involved in the measurements and thus provides more dense measurements data for more accurate analysis. A measurement volume (that is

a volume defined during calibration, where accurate DIC measurements can take place) is set to ca. 650 mm x 650 mm x 650 mm. The full-scale DIC system setup is shown in Fig. 4.21(a).

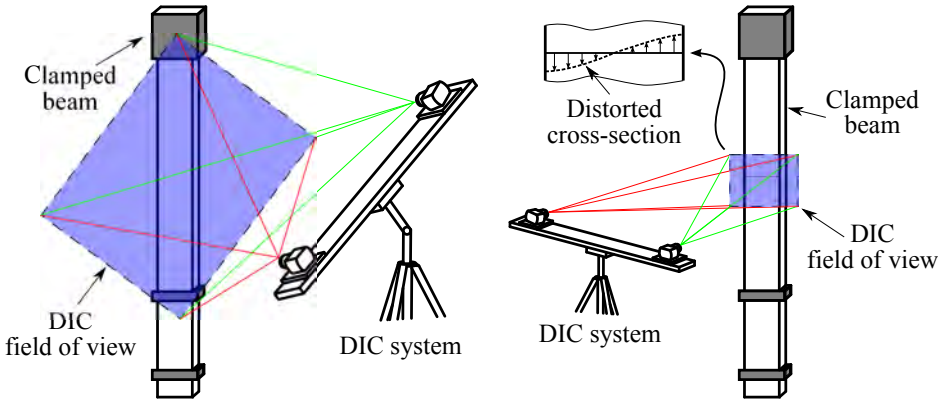

(a) Full-scale system (b) Small-scale system

Figure 4.21: Diagram of a full-scale (a) and a small-scale (b) DIC system setups for experiments on composite beams. Digital cameras are installed on a stiff camera bar mounted on a tripod.

Experimental measurements on the warping deformations in the composite beams are performed in a similar way as done by Dufort et al. (2001), where the warping in short composite beams was measured under three point bending. The second (small-scale) DIC system is assigned for very accurate measurements on the central part of a beam specimen. Warping deformations of the cross-sections in this region are measured based on the axial displacement field measured for the beam flange surface. A cross-section of interest is selected in the measured area and the axial displacements (vertical displacements in Fig. 4.21(b)) of the points constituting the cross-section, reduced by the rigid body motion, represent the cross-section distorsion, that is warping. Thus, warping deformations are measured only on the outer surface of the beam flange.

Among a number of factors, the accuracy of the DIC system measurements depends on the measurement volume: Smaller the volume - more accurate are the measurements. Therefore, the small-scale DIC system is equipped with 4-megapixel digital cameras with 50 mm focal distance lenses and narrow angle of view to limit the measurement volume by width of the beam specimen flange. The measurement volume is thus set to ca. 200 mm x 200 mm x 200 mm. A scheme of the small-scale DIC system setup is given in Fig. 4.21(b). A photo of the DIC systems is shown in Fig. 4.22.

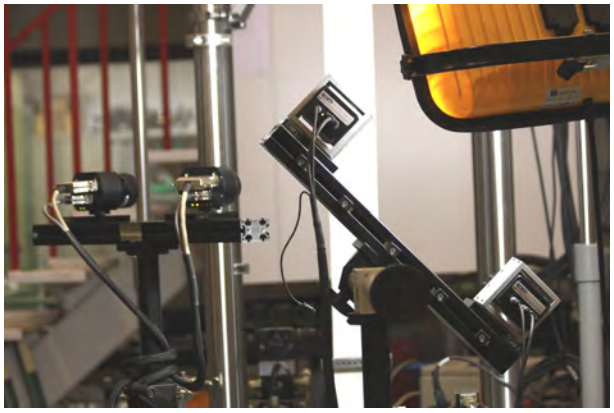

Figure 4.22: Photo of DIC systems setup. Left – small-scale DIC system; Right – full-scale DIC system. A composite beam appears white.

For reduction of the twist angle from the DIC measurement data, a twist calculation algorithm, developed earliear and described in Section 2.3.3, is used. Due to small magnitudes of the expected beam twist angles, the twist calculation algorithm accuracy is evaluated using a simple test. The test setup consists of an aluminum plate representing a composite beam flange (350 mm x 100 mm). The plate is fixed in a tool where the plate rotation can be accurately controlled with steps as small as 1/6°. The 3D displacement field over the entire plate is measured by the small-scale DIC system, while the plate is rotated step by step in a range of $-5°..+5°$. The accuracy of the twist angles calculations are then evaluated.

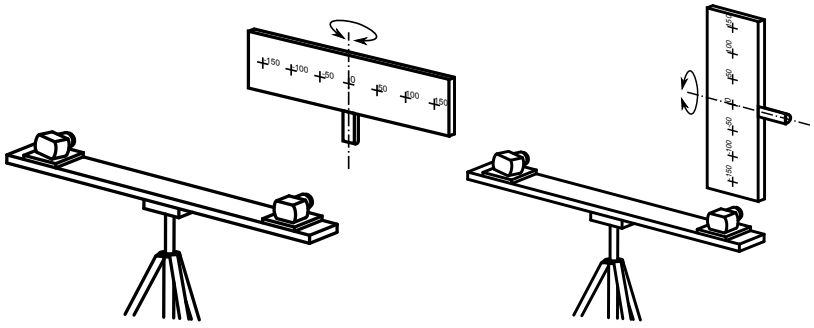

(a) Horizontal setup (b) Vertical setup

Figure 4.23: Diagram of horizontal (a) and vertical (b) DIC system setups for accuracy evaluation of DIC system based twist angle measurement method.

The twist calculation accuracy evaluation is done for both vertical and horizontal

plate orientations to check if the DIC system orientation influences the measurement accuracy. Diagrams of both evaluation test configurations are shown in Fig. 4.23, and snapshots of both plateconfigurations with overlaid measured displacement field are shown in Fig.4.24.

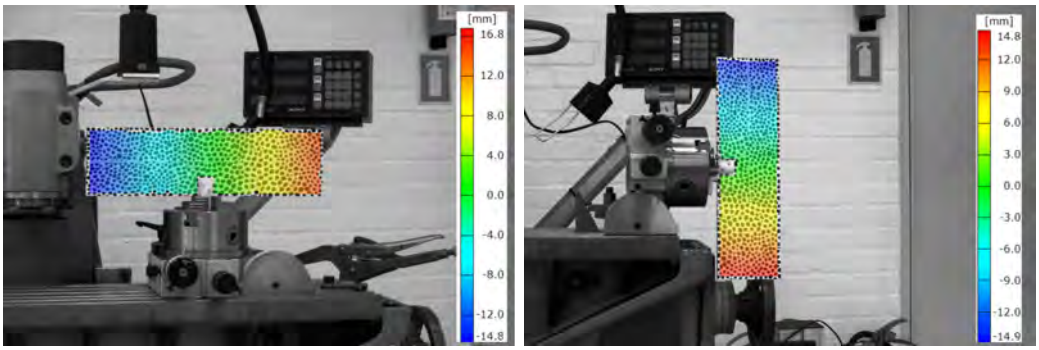

(a) Horizontal setup (b) Vertical setup

Figure 4.24: Snapshots of horizontal (a) and vertical (b) setups for evaluation of the DIC measurements accuracy.

The results of comparison between the set and the measured twist angles are presented in Fig. 4.25. It can be seen that in general, the plate twist angles are accurately measured with errors of less than 4% in the most of the range. Higher error levels are obtained only for the lowest twist angles in range of about $\pm 0.5°$. According to the results obtained, the twist measurement method accuracy in the range of $\pm 0.5°$ is questionable. Therefore an extra optical measurement system was used during the tests.

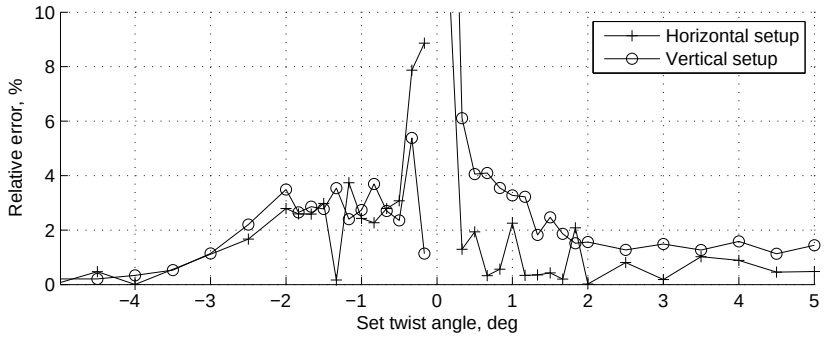

Figure 4.25: Errors in twist angle calculations obtained by processing DIC measurements.

4.5.6 Optical measurement system

An optical system utilized in the present test setup is an analog of the systems used by Chandra et al. (1990), Chandra and Chopra (1991) and Greenhalgh and Pastore (1993) in their experimental investigations on the bend-twist coupling effects in composite beams. The system includes several lasers, a set of small mirrors glued to a beam specimen and a screen for registration of the laser beam deflections. This system provides direct measurements of bending and twist angles at selected points along the beam.

Compared to the DIC systems, the optical measurement system has one significant disadvantage: While a DIC system can virtually provide 3D measurements for any point of the beam surface and at any time after the test has been performed, the optical system can provide measurements only for limited number of points, carefully chosen well in advance before the test begins. However, if high quality lasers are used in the optical system, it can provide angular measurements of much higher accuracy than the DIC system, and therefore it is used in the present test setup to ensure accurate measurements of small bending and twist angles along the beam specimens.

The essence of the optical measurements is in registration of the laser beam deflections reflected from the mirrors glued to the tested beam specimen. Thus, six mirrors are glued along the mid-width of the back side (opposite to the side measured by the DIC systems) with a step of 100 mm starting from the beam clamped end. The laser beam deflections are registered by measuring the laser spot displacements on a screen mounted ca. 2 meter away from the tested beam specimen, see Fig. 4.26. The displacements are measured by taking snapshots of the laser spots pattern together with a long ruler attached to the screen. To reduce the spherical distortion effects in the snapshots, a digital camera equipped with lenses of very long focal distance mounted on a tripod far away from the screen, is used.

The bending and twist angles are calculated by processing the snapshots taken during the experiments. For a screen placed a distance L away from the mirrors, the vertical and horizontal displacements ΔZ and ΔX of the laser spot correspond to bending and twist angles BA and TW:

$$BA = \frac{\Delta Z}{2L} \qquad\qquad TW = \frac{\Delta X}{2L} \tag{4.1}$$

Due to poor quality of the laser pointers used in the tests as the laser beam sources, the spots on the screen were often fuzzy, and thus, accuracy of the present optical measurement system configuration was limited by approx. $0.01 - 0.05°$.

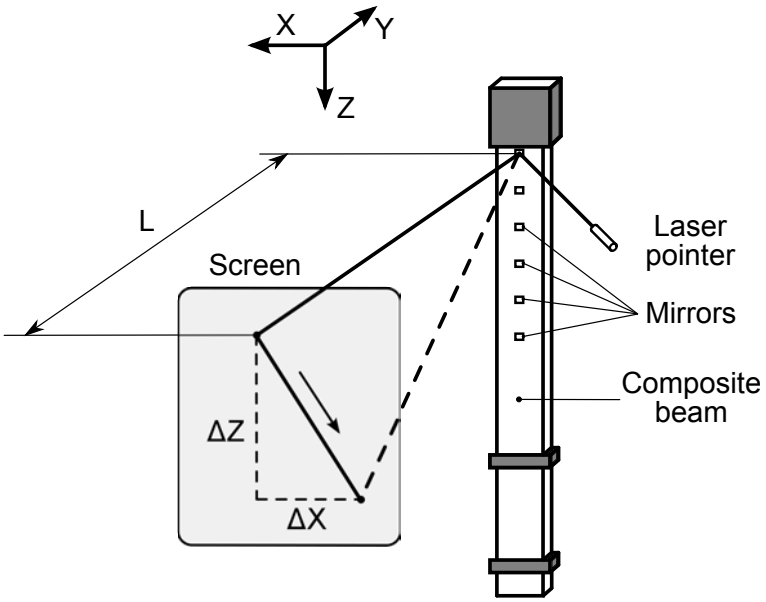

Figure 4.26: Diagram of optical measuring system setup.

4.6 Results and discussion

The results of bending and twist angles along the composite beams measured by the full-scale DIC system and optical measurements are compared. Next, the composite beam global responses in bending and torsion load cases predicted numerically are compared to the experimental measurements. The results are presented in form of distribution of bending displacements and twist angles along the beams. Finally, numerical predictions and experimental measurements of the warping deformations in the beams are discussed.

4.6.1 Comparison of DIC and optical measurements

The bending and twist angles along the beam specimens obtained using the DIC measurements are calculated according to the algorithm developed during the experimental study of bend-twist coupling effects in a wind turbine blade section, see Section 2.3.3. The bending angles are determined as slopes in the bending displacement curve of the beam. They are determined from the first derivative of a polynomial fit to the bending displacement distribution along the beam.

Representative results for the twist angle measurements are given in Fig. 4.27(a), where twist of the box-beams subjected to bending moment is presented. These

results correspond to the lowest twist angles for the composite beams and therefore are of highest interest for evaluation of the twist angles measured by DIC (recall questionable accuracy at low twist angles in Fig. 4.25).

Generally a very good correlation is found between the measurements done by the full-scale DIC system and the optical measurements. Notice some differences between the results of the two measurement techniques especially at very low twist angles. The differences are less than about 0.05° – they are observed most clearly for the 0° UD configuration beam specimen.

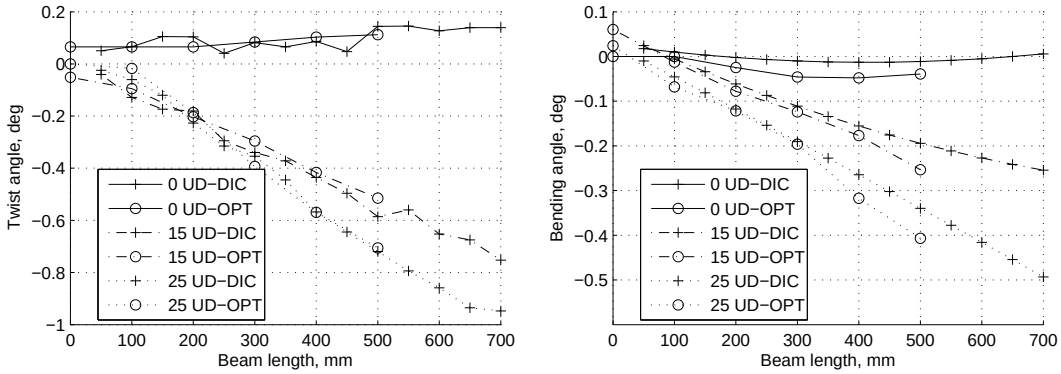

(a) Twist angle along composite box-beams in bending

(b) Bending angle along composite box-beams in torsion

Figure 4.27: Comparison of twist angles (a) and bending angles (b) along composite beams measured by DIC and optical systems.

The representative cases corresponding to one of the lowest magnitudes of the measured bending angle are presented in Fig. 4.27(b), where bending angles of the box-beams in torsion are shown. The results of the two measurement techniques generally do not differ more than ±0.05°, which is very similar to the results of twist angle measurements. Based on the results of the accuracy evaluation of the bending and twist angles measured with the full-scale DIC system, the DIC measurement technique is proved to be of a sufficient accuracy level. Therefore, to avoid overloading of the following graphs, the results of the optical measurements are not presented.

4.6.2 Global response of composite beams

The response of the composite beams in bending and torsion predicted by FE models and measured during the experiments are shown in Figs. 4.28 - 4.31. Bending displacements, bending angles and twist angles are calculated by application of the algorithm described in Section 2.3.3 to the full-scale DIC measurements on the beams and to the results of the beam FE models.

Two specimens are tested for each of the box-beam configurations while only one I-beam specimen per configuration is tested. Therefore, two experimental results are available on the Box-beam result plots. Note, that some discrepancies occurred between the experimental results for the box-beam specimens of equal configurations, see e.g. bending of the 0° UD beams in Fig. 4.29(a) and Fig. 4.29(b). The discrepeancies are most likely caused by possible beam geometry variations unintentionally introduced during the specimen manufacturing, however, the discrepancies are not large.

Note that for an unknown reason one of the 25° UD box-beams in torsion demonstrated response very similar to the response of one of the 15° UD box-beams, so that the result curves corresponding to the two beams are almost indistinguishable, see Fig. 4.29. In bending, however, the beams responded differently, see Fig. 4.28. Additionally, the 0° UD I-beam specimen demonstrated unexpected coupled behavior (Fig. 4.30(c)). The reason is found to be in the specimen geometrical defects: The UD flanges are not properly aligned with the beam longitudinal axis as well as in the cross-section plane, which is shown in Fig. 4.32.

In general the composite beam responses can be desrcibed as follows: The 0° UD beams demonstrated highest bending stiffnesses and lowest torsional stiffnesses together with smallest bend-twist couplings, while the 25° UD beams demonstrated lowest bending stiffnesses and highest torsion stiffnesses with largest bend-twist couplings. It has to be mentioned, that the torsional stiffness did not vary significantly with the fiber biasing in the UD flanges for both box- and I-beam configurations, see Fig. 4.29(c) and 4.31(c). Apparently, for the present beam configurations, contribution of the biax shear webs to the torsional stiffness is considerable, and therefore, the effect of fiber biasing in the flanges on the torsional stiffness is reduced.

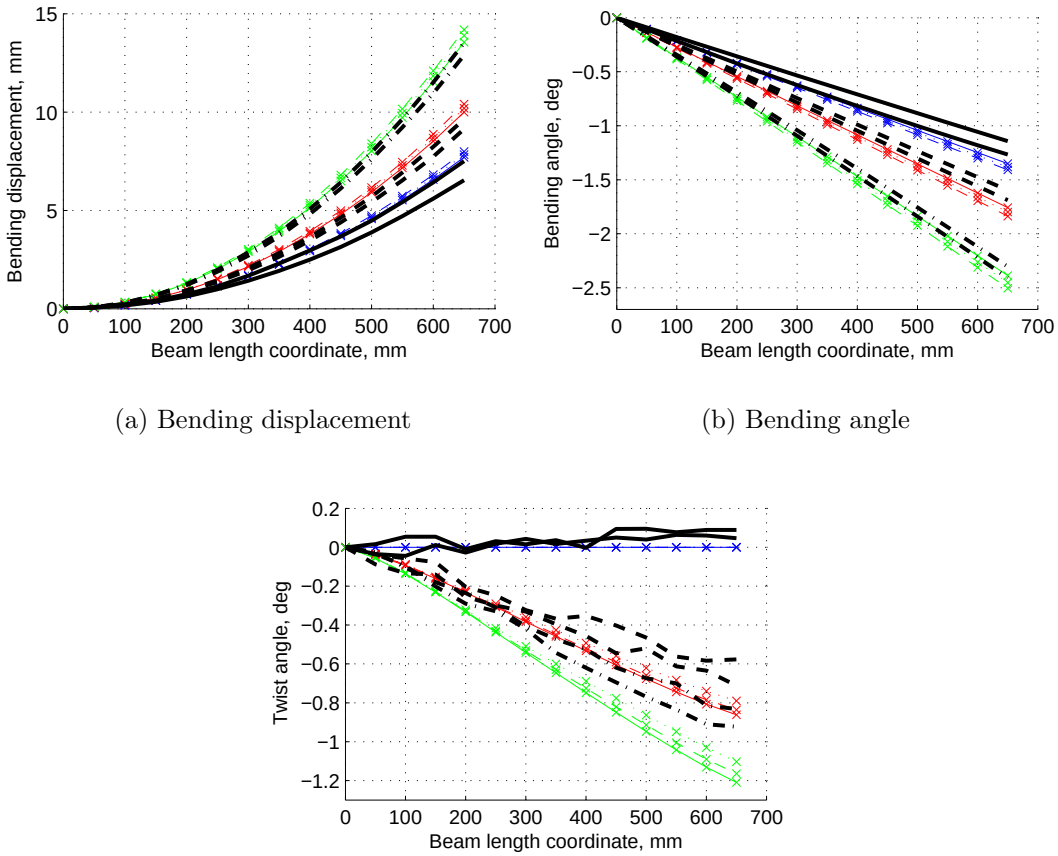

(a) Bending displacement

(b) Bending angle

(c) Twist

Figure 4.28: Bending displacements (a), bending angles (b) and twist angles (c) for box-beams in bending. Bending moment 0.4 kNm. Curves are identified as follows. FEA by beam configuration: 0° UD – blue, 15° UD – red, 25° UD – green. FEA by element type: shell elements w/o offset nodes – dashed, shell elements with offset nodes – solid, continuum shell elements – dotted. Experiment by beam configuration: 0° UD – black solid, for 15° UD – black dashed, for 25° UD – black dashdot.

In general the beam bending responses in bending predicted by all the FE models for all the box- and I-beam configurations agree very well with the experiments, see Fig. 4.28(a), 4.28(b), 4.30(a) and 4.30(b). There is a common tendency for the FE models to slightly underestimate the beam bending stiffnesses and therefore to generate higher bending displacements and bending angles. However, the deviations of the numerical results are all within the range of the discrepancies in the experimental data for the corresponding beam configurations.

The beam bending responses in torsion due to the bend-twist coupling effects agree well to the experiments for all the beam configurations. For the box-beams, the deviations between the numerical results and the experimental data are within the range of scatter in the experimental data for the corresponding beams configurations, see Fig. 4.29(a) and 4.29(b). A general trend in all the FE models to slightly overpredict the bending response is observed. For the I-beams, the experimentally measured responses are of very low magnitudes and thus subject to measurement errors, but the numerical results still reasonably well correlate to the experiments, see Fig. 4.31(a) and 4.31(b).

Noticeable deviations are observed between the numerical results and the experimental data for the twist angless along the box-beams in bending (Fig. 4.28(c)), and significant deviations are observed for the same results for the I-beams, see Fig. 4.30(c). As the beam bending responses in torsion are rather well predicted numerically, it is unlikely, that the current issue is due to shortcomings of the numerical models.

Indeed, recall the way the bending moment is applied to beams, see Fig. 4.18. It was realized, that the two actuators applying forces to a beam specimen in bending implicitly impose some twist constrains by generating a parasitic torque. The two load application points (depicted as hollow circles in the figure) at the beam specimen slightly move sideways as the beam twists and induce the parasitic torque by two reaction forces generated by the actuators.

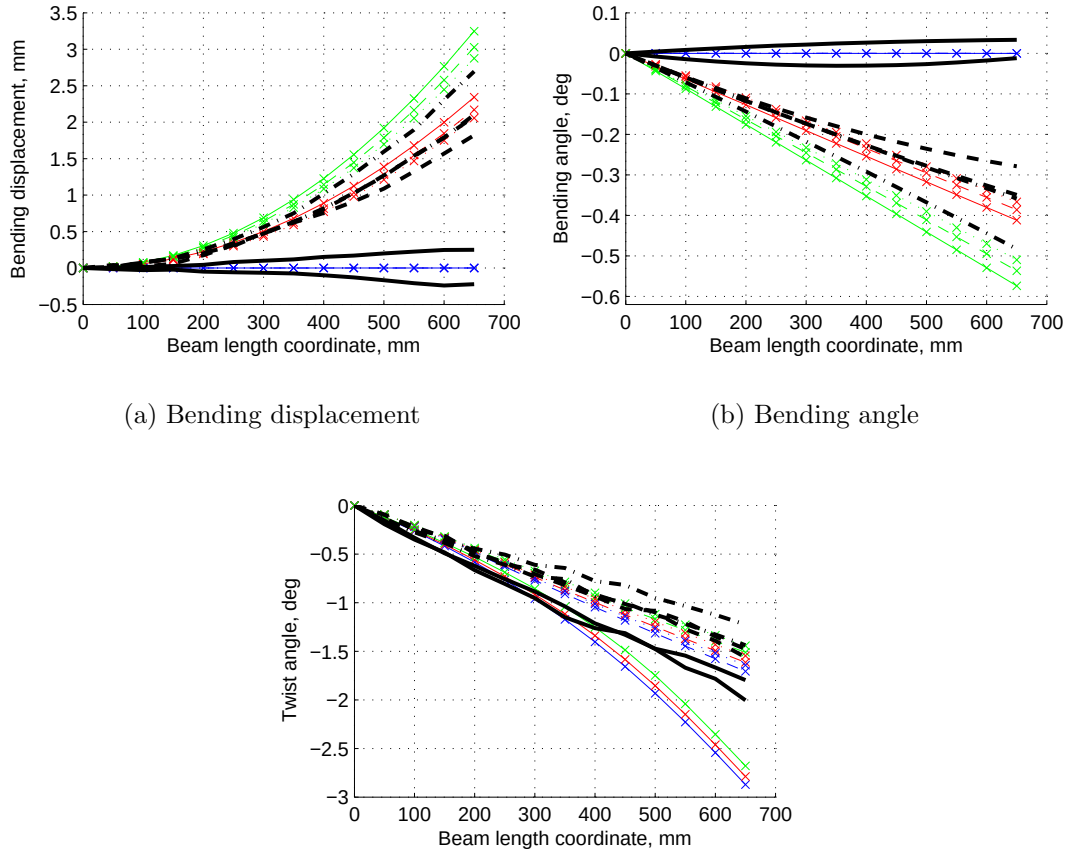

(a) Bending displacement

(b) Bending angle

(c) Twist

Figure 4.29: Bending displacements (a), bending angles (b) and twist angles (c) for box-beams in torsion. Torque 0.2 kNm. Curves are identified as follows. FEA by beam configuration: 0° UD – blue, 15° UD – red, 25° UD – green. FEA by element type: shell elements w/o offset nodes – dashed, shell elements with offset nodes – solid, continuum shell elements – dotted. Experiment by beam configuration: 0° UD – black solid, for 15° UD – black dashed, for 25° UD – black dashdot.

In the test setup the load application point is made as a special fork, a bolt and a spherical bearing, shown in Fig. 4.19(b). Therefore, an attempt was undertaken to set the fork free to move sideways with respect to the bolt by creating a slit instead of a circular hole for the fork-bolt connection. However, the reaction forces provided by the actuator due to the fork sideways movements still generated a parasitic torque enough to reduce the beam twist response. It is clear that the effect of the parasitic torque is much more pronounced for the I-beams due to the low torsional stiffnesses of these beams. Therefore, the experimental results for the beam twist responses in bending (Fig. 4.28(c) and 4.30(c)) are not accurate, yet demonstrating significant bend-twist coupling effects in the 15° UD and 25° UD beam configurations.

The twist of the box-beams in torsion predicted by the FE models built of shell elements with offsets significantly deviates from the experimental data, see Fig. 4.29(c). The difference in the beam free end twist for the present beam configurations reach 100% of the experimentally measured values. This is much higher than e.g. the tip twist errors of 20%-30% demonstrated by a similar FE model in case of torsion of a wind turbine blade section in Chapter 3.

In general, the beam twist angles in torsion predicted by the FE models built of shell elements without nodal offsets and built of continuum shell elements in a good agreement with the experimental data, see Figs. 4.29(c) and 4.31(c). Note, that the problem of innacutare twist prediction by the FE models built of shell elements with nodal offsets does not appear in torsion of the I-beams (Fig. 4.31(c)). Hereby, this problem reveals itself only when closed cross-section beams are subject to torsion.

As seen in Figs. 4.29(c) and 4.31(c), the distributions of twist angle along the beams are very close to linear. Therefore, the effect of torsional stiffening of the beams due to restrained warping as it was demonstrated by Chandra et al. (1990) (which was expected to appear as variations of the torsional stiffnesses along the beams and subsequent nonlinear twist angle distributions along the beams) is found insignificant for the studied composite beam configurations.

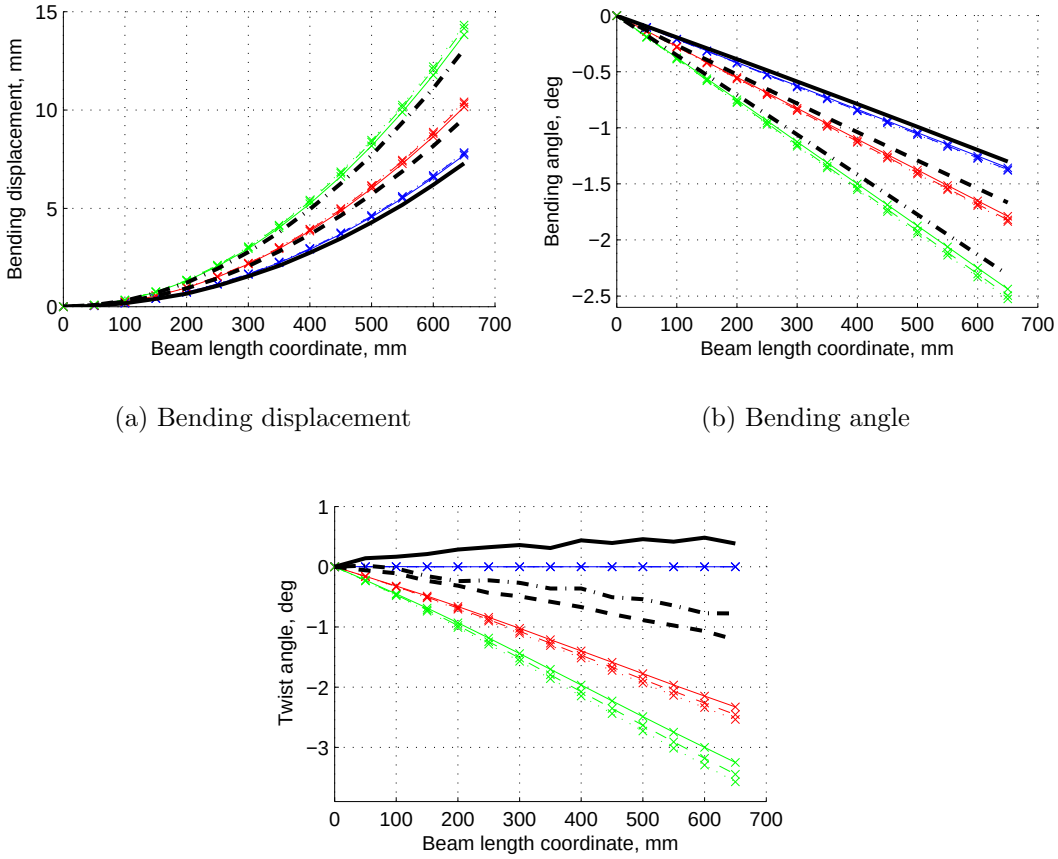

(a) Bending displacement

(b) Bending angle

(c) Twist

Figure 4.30: Bending displacements (a), bending angles (b) and twist angles (c) for I-beams in bending. Bending moment 0.4 kNm. Curves are identified as follows. FEA by beam configuration: 0° UD – blue, 15° UD – red, 25° UD – green. FEA by element type: shell elements w/o offset nodes – dashed, shell elements with offset nodes – solid, continuum shell elements – dotted. Experiment by beam configuration: 0° UD – black solid, for 15° UD – black dashed, for 25° UD – black dashdot.

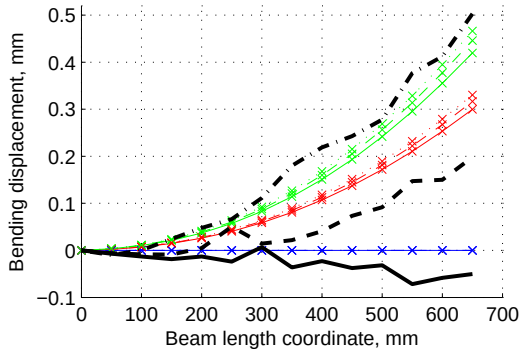

(a) Bending displacement

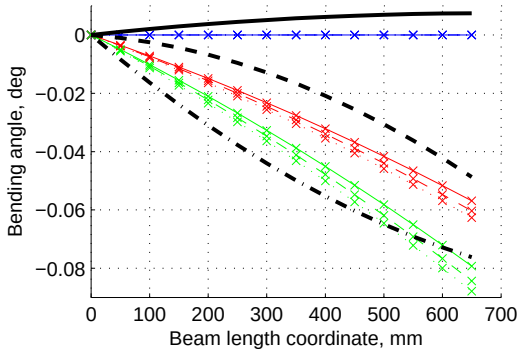

(b) Bending angle

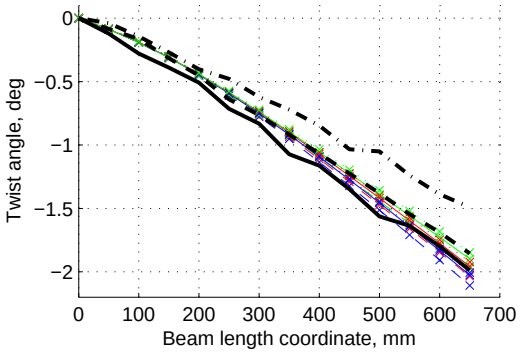

(c) Twist

Figure 4.31: Bending displacements (a), bending angles (b) and twist angles (c) for I-beams in torsion. Torque 10 Nm. Curves are identified as follows. FEA by beam configuration: 0° UD – blue, 15° UD – red, 25° UD – green. FEA by element type: shell elements w/o offset nodes – dashed, shell elements with offset nodes – solid, continuum shell elements – dotted. Experiment by beam configuration: 0° UD – black solid, for 15° UD – black dashed, for 25° UD – black dashdot.

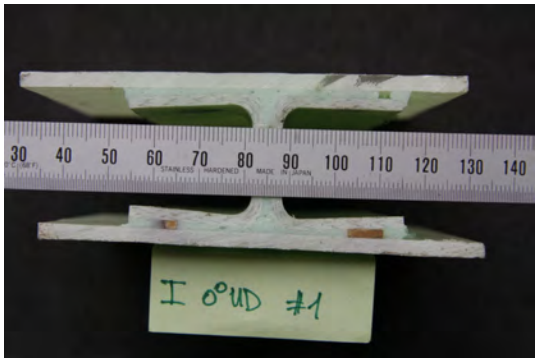

Figure 4.32: Geometry defects in one of the I-beam specimens.

4.6.3 Warping in composite beams

Warping predicted numerically and measured experimentally for the cross-section in the middle of the composite beams is presented in Figures 4.33 – 4.36. The selected cross-section of interest is in the beam mid-length position, which corresponds to 300 mm position according to the plots of the beam global responses in Figs. 4.28 – 4.31. Only the results of the FE models built of shell elements with nodal offsets and continuum shell elements are presented here. The results of the FE models built of shell elements without nodal offsets are not presented because of non-trivial warping patterns due to discontinuities in the wall mid-thickness planes.

In general, the numerically predicted warping deformations in the Box-beams agree well to the experimental results, however some minor deviations, particularly noticeable for the 0° UD beams, see Fig. 4.33 and 4.34. As seen in Fig. 4.33(b), the results of the FE models built of shell elements with nodal offsets tend to overpredict the warping deformations at the flange edges for all the beam configurations. The reason for this kind of overprediction is unclear.

Warping deformations in the I-beams are also rather well predicted by the FE models, see Fig. 4.35 and 4.36. An opposite warping direction is seen for the 0° UD beam configuration, which is explained by the specimen geometry defect described earlier, and the bend-twist coupling in the beam induced by this geometry defect.

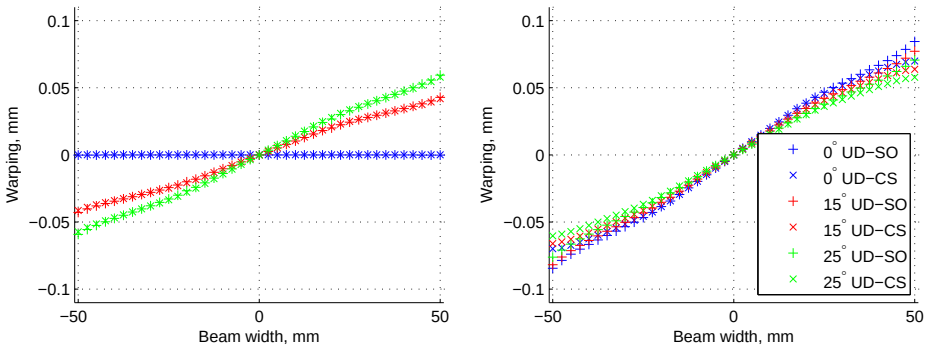

(a) Bending (b) Torsion

Figure 4.33: Warping in box-beams in bending (a) and torsion (b). FEM results. SO – FEM built of shell elements with nodal offsets; CS – FEM built of continuum shell elements.

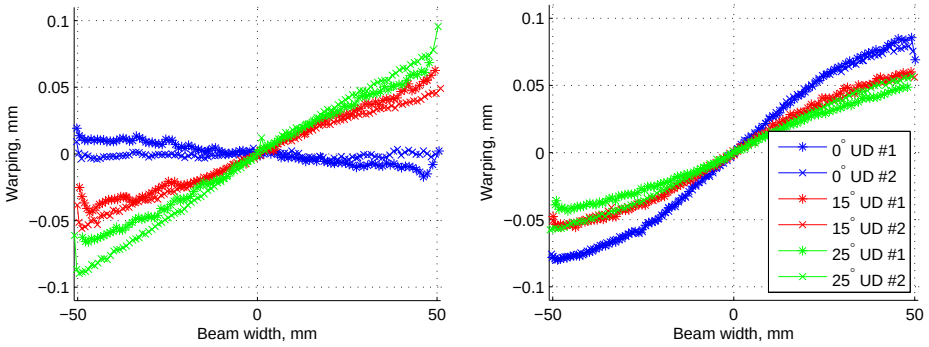

(a) Bending (b) Torsion

Figure 4.34: Warping in box-beams in bending (a) and torsion (b). Experimental results.

Note an interesting effect demonstrated in all the beam configurations: When the beam twist is caused by application of torque, the warping deformation pattern is non-linear and resemble the shape of sine function. In contrast, in bending, where the beam twist is induced by the bend-twist coupling, the warping deformation pattern is linear. This effect is clearly seen on the plots of experimental results for both Box- and I-beam configurations, see Fig. 4.34 and 4.36.

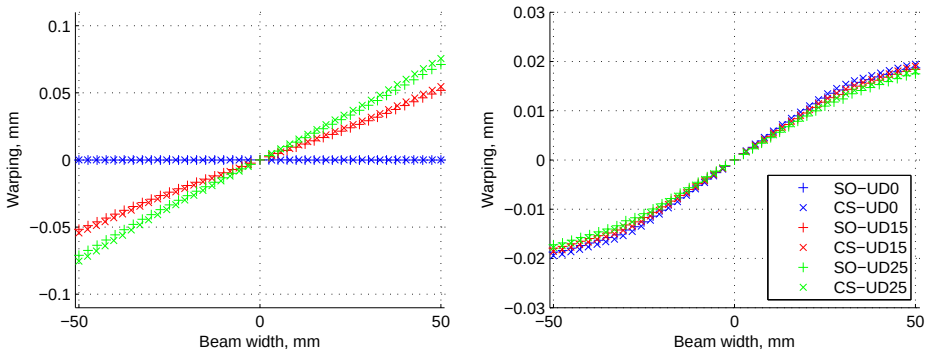

(a) Bending (b) Torsion

Figure 4.35: Warping in I-beams in bending (a) and torsion (b). FEM results. SO – FEM built of shell elements with nodal offsets; CS – FEM built of continuum shell elements.

The obtained results indicate that the warping situations in the composite beams are well predicted by all the FE models for all the beam configurations. The attempt of experimentally measure warping in composite beams was a success with measured warping deformations as small as 0.02 mm in case of I-beams.

4.7 Conclusions

FE models of three types are investigated in the present study and the obtained numerical results are compared against the experiments on a set of uniform composite beams of open (I) and closed (box) cross-sections with different levels of bend-twist couplings. The three FE model types include shell elements of standard formulation without nodal offsets, shell elements with nodal offsets and continuum shell elements.

To generate experimental data for validation of the results of the developed FE models the composite beams were tested in bending and torsion. An advanced test

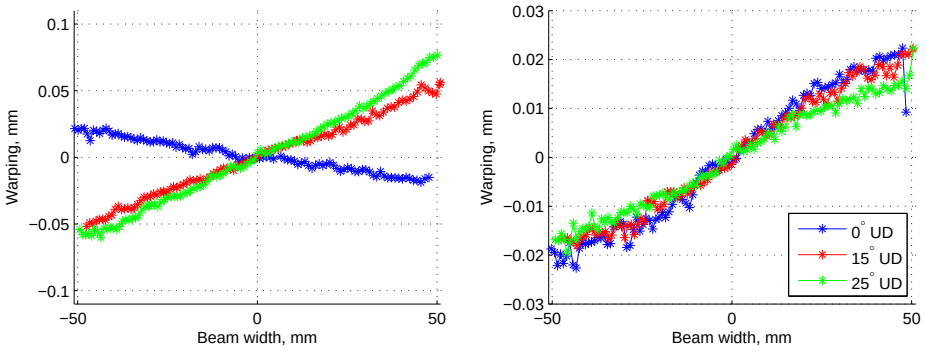

(a) Bending (b) Torsion

Figure 4.36: Warping in I-beams in bending (a) and torsion (b). Experimental results.

setup based on a four column testing machine is designed for this purpose. The test setup consisted of such components as a specially designed off-axis load protection system, a hydraulic system for accurate load application, two DIC systems for full-scale and local 3D measurements on the beam specimen deformations.

According to the results, the FE models built of shell elements without nodal offsets and the FE models built of continuum shell elements demonstrated high accuracy in all load situations. Therefore, when a beam FE model built of shell elements without nodal offsets has no rigid elements along the beam due to the material ply drops, the accuracy of the model is proved to be high, which makes these type of FE models attractive for investigations of the bend-twist coupling effects in composite beam structures without ply drops (e.g. uniform beams).

Twist distributions along the box-beams in torsion were poorly predicted by the FE models with shell elements with nodal offsets. The observed tip twist error was as high as 100% of the experimentally measured values. Thus, the accuracy problem of this type of FE models appears to be very significant even for such simple structures as the considered beams. However, these models did not demonstrate any significant inaccuracies in predicting twist of the open cross-section I-beams subject to torsion.

The bending responses in torsion induced by the bend-twist coupling are generally accurately predicted by all FE models, yet in case of the I-beams the bending responses are found to be of small magnitudes due to low torsional stiffness of the I-beams, and therefore were subject to measurement noise. The twist responses of

the beams in bending induced by the bend-twist coupling could not be validated due to a parasitic torque generated by the load application system. The parasitic torque significantly affected the experimental results of twist in the I-beams due to low torsional stiffnesses of the specimens. For the box-beams, the parasitic torque effect was not as high and twist angles of singnificant magnitudes were observed.

It was found that warping restrains at the clamped end did not significantly affected the global response of the composite beams. Warping deformations in the beams were generally well predicted by all the FE models. An interesting effect of linear warping was found in the composite beams when the beam twist was induced by the bend-twist coupling in bending load case.

This page is intentionally left blank.

Chapter 5

Simple bend-twist coupling analysis method for beams

5.1 Introduction

A simple method developed for analysis of bend-twist coupling effects in beam structures is presented in this chapter. The foundation for the method was given by Chandra et al. (1990), where author used a simple formulation in form of a 2x2 matrix to describe the relation between the bending and torsion moments applied to a beam and its bending and twist responses. The 2x2 matrix incorporated only bending stiffness, torsional stiffness and bend-twist coupling coefficient. A similar relation considering only beam elongation and twist was as well formulated for the studied extension-twist coupled beams. The beam responses, calculated by using the two adopted formulations were compared against the experimental results generated during the study. Similar formulations were used later by Lobitz and Veers (1998, 2003), Ong and Tsai (1999) and Lobitz et al. (2001).

In the present work, the same 2x2 constituting matrix formulation considering only beam bending and twist is adopted for application to the experimental results obtained by DIC measurements on bend-twist coupled beams and to the results of detailed 3D FE models (e.g. built of shell elements) of the beams. A vast amount of the measurement data available for the tested/modeled beams is processed to evaluate beam bending stiffness, torsional stiffness as well as bend-twist coupling coefficient and their variations along the beams, if any.

The results from the simple bend-twist coupling analysis method will be compared to the results of the Beam Cross-Sectional Analysis Software (BECAS) tool

developed recently by Blasques and Lazarov (2011) and the Variational Asymptotic Beam Sectional Analysis (VABS) by Yu et al. (2002) in a benchmark case of bend-twist coupled solid composite beam.

Finally, the developed method is applied to the numerical and the experimental results obtained for the wind turbine blade section and the composite beams investigated earlier by the author in Chapters 2 - 4. The lengthwise variations of bending stiffness, torsional stiffness as well as bend-twist coupling coefficient are evaluated for these composite structures.

5.2 Motivation and objectives

Experimentally measured distributions of bending displacements and twist angles along composite beams were compared to results from detailed FE models of the beams studied in Chapter 4. The results of the studies demonstrated, that this method is suitable for a very simple experimental investigation on the bend-twist coupling effects in a blade structure as it is done in Chapter 2. However, to evaluate the magnitude of bend-twist coupling in a beam in the format of classical Euler-Bernoulli or Timoshenko beam formulation, the appropriate elements of the cross-section stiffness matrices for the beam structure have to be calculated.

The objective of the present study is to develop a simple method particularly aimed at the evaluation of the magnitudes of bend-twist elastic coupling in a composite beam in form of classical Euler-Bernulli formulation. The main feture of the method is that it should be possible to apply it both to the numerical results, generated by a detailed FE model of the beam, and to experimental results for the beam.

5.3 Analysis method

A simple formulation for a cross-section stiffness matrix adopted by Chandra et al. (1990) and Lobitz and Veers (1998) is used in the present analysis. The cross-section stiffness matrix describes the bending and torsion behavior of a beam by a relation between the generalized bending moment M and torque T applied to the beam cross-section and the corresponding deformations κ_b and κ_t by mean of

bending stiffness EI, torsional stiffness GJ and – bend-twist coupling coefficient K:

$$\begin{bmatrix} M \\ T \end{bmatrix} = \begin{bmatrix} EI & -K \\ -K & GJ \end{bmatrix} \begin{bmatrix} \kappa_b \\ \kappa_t \end{bmatrix} \tag{5.1}$$

The 2x2 stiffness matrix corresponds to a reduced form of the cross-section stiffness matrix written according to the classical Euler-Bernoulli beam formulation, where several coupling coefficients are neglected. The neglected coefficients correspond to the coupling between bending and extension of the beam and to the coupling between bending of the beam in two principal directions. It can be shown e.g. by using the classical laminate theory, that these couplings are very limited for symmetric cross-sections with symmetric layups. For common designs of the load carrying spars of wind turbine blades (cf. Fig. 3.5) which are very close in shape to symmetric cross-sections and often have symmetrical layups, these couplings are also small, and the presented simple formulation can thus be applied.

Under certain circumstances the elements of the cross-section stiffness matrix (5.1) can also be compared to the corresponding elements of the cross-section 6x6 stiffness matrix formulated according to the Timoshenko beam theory. This is particularly the case when no coupling exist between the beam bending and torsion deformation modes included into the 2x2 stiffness matrix formulation and the other deformation modes accounted in the Timoshenko beam formulation, see (2.1) and (2.2).

Following the relation (5.1), Lobitz and Veers (1998) introduced a coupling coefficient α, which is "normalized" with respect to bending EI and torsional GJ stiffnesses and therefore is often used as a measure of bend-twist coupling in beams:

$$\alpha = \frac{K}{\sqrt{EIGJ}}; \qquad -1 < \alpha < 1 \tag{5.2}$$

The presented formulation is used for evaluation of three important parameters of a beam: Bending stiffness EI, torsional stiffness GJ and bend-twist coupling coefficient K based on the numerical results provided by a detailed 3D FE model of the beam (e.g. built of shell finite elements), or based on the experimental results on the beam obtained by using a digital image correlation system. By applying the two load cases, bending and torsion, and measuring bending and twist responses of the beam in each load case, it is possible to resolve the system.

It is easy to see that when two independent load cases, bending and torsion, are considered, the system (5.1) becomes overdetermined, as it consists of four equations and only three unknowns, thus, one of the measured parameters can be excluded from the system. According to the results of the experiments on composite beams presented in Chapter 4, the beam deformations induced by the bend-twist coupling are typically small, see e.g. the results of I-beams bending deformations induced in torsion in Fig. 4.31(a). Therefore, to mitigate the effect of the measurement noise particularly high when small parameters are measured, either beam bending κ_b induced in torsion or beam twist κ_t induced in bending (whichever is of lowest accuracy) is excluded from the system.

Consider now bending and torsion load cases separately applied to a uniform beam. All the beam cross-sections experience equivalent loading conditions described by the system (5.1). Therefore two equations are written for the case of a bending moment M applied to the beam:

$$M = EI\kappa_{bb} - K\kappa_{tb}, \qquad 0 = -K\kappa_{bb} + GJ\kappa_{tb}, \tag{5.3}$$

and similarly, two equations are written for the case of a torque T applied to the beam:

$$0 = EI\kappa_{bt} - K\kappa_{tt}, \qquad T = -K\kappa_{bt} + GJ\kappa_{tt}; \tag{5.4}$$

In the two loaded cases considered above, κ_{tb} and κ_{bt} – are the beam deformations corresponding to the beam twist the in bending load case and to the beam bending in the torsion load case accordingly, and they are fully determined by the bend-twist coupling. By excluding κ_{tb} from the system of equations, the expressions for the beam cross-section properties are determined the following way:

$$EI_b = M\frac{\kappa_{tt}}{\kappa_{tt}\kappa_{bb} - \frac{M}{T}(\kappa_{bt})^2} \tag{5.5}$$

$$GJ_b = T\frac{\kappa_{bb}}{\kappa_{tt}\kappa_{bb} - \frac{M}{T}(\kappa_{bt})^2} \tag{5.6}$$

$$K_b = M\frac{\kappa_{bt}}{\kappa_{tt}\kappa_{bb} - \frac{M}{T}(\kappa_{bt})^2} \tag{5.7}$$

$$\alpha_b = \frac{K_b}{\sqrt{EI_b GJ_b}} = \frac{\kappa_{bt}}{\sqrt{\frac{T}{M}\kappa_{tt}\kappa_{bb}}} \tag{5.8}$$

By excluding κ_{bt} from the system, the expressions for the beam cross-section properties are determined as follows:

$$EI_t = M\frac{\kappa_{tt}}{\kappa_{tt}\kappa_{bb} - \frac{T}{M}(\kappa_{tb})^2} \tag{5.9}$$

$$GJ_t = T\frac{\kappa_{bb}}{\kappa_{tt}\kappa_{bb} - \frac{T}{M}(\kappa_{tb})^2} \tag{5.10}$$

$$K_t = T\frac{\kappa_{tb}}{\kappa_{tt}\kappa_{bb} - \frac{T}{M}(\kappa_{tb})^2} \tag{5.11}$$

$$\alpha_t = \frac{K_t}{\sqrt{EI_t GJ_t}} = \frac{\kappa_{tb}}{\sqrt{\frac{M}{T}\kappa_{tt}\kappa_{bb}}} \tag{5.12}$$

Typically, the beam deformations κ_{tb} and κ_{bt} induced by the bend-twist coupling are of much lower magnitudes than κ_{bb} and κ_{tt}, therefore the second component in the general denominator in (5.5)-(5.12) is much lower than the first component, so that bending EI and torsional GJ stiffnesses are almost insensitive to the fluctuations of the coupling induced responses caused by e.g. measurement noise and thus:

$$EI_b \approx EI_t; \qquad GJ_b \approx GJ_t \tag{5.13}$$

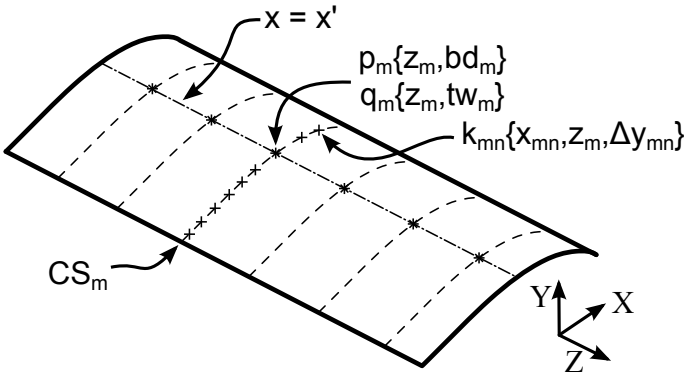

Figure 5.1: Beam response measurements.

5.3.1 Beam response measurements

Calculations of bending and twist responses of a beam in bending and torsion load cases considered in the simple bend-twist analysis method can be done based on the displacement field of the beam surface, obtained as a result of a detailed 3D FE analysis on the beam, or from experiments on the beam. The calculation algorithm is an expansion of the algorithm developed for calculations of the wind turbine blade section deformation described in Section 2.3.3.

Consider a part of the beam surface for which the full 3D displacement field is obtained, see Fig. 5.1. A number of cross-sections CS_m, with $m = 1..M$, are selected on the beam surface. Each cross-section is composed out of N points for which vertical displacements Δy_{mn}, corresponding to the beam bending displacements, are available. Thereby, the measured bending displacement field for the considered beam surface can be written as $k_{mn} = \{x_{mn}, z_m, \Delta y_{mn}\}$, where $m = 1..M$ and $n = 1..N$

Bending displacement bd_m and the twist angle tw_m of a cross-section CS_m are calculated from a linear fit to the bending displacements of the points constituting the cross-section, see details in Table 2.1 and Fig. 2.19 for the original algorithm. The cross-section bending displacement is then calculated for a selected position x'. Thus, the distributions of bending displacements $p_m\{z_m, bd_m\}$ and twist angles $q_m\{z_m, tw_m\}$ along the beam are obtained.

For calculation of the cross-section bending rotation κ_b, the i^{th} order polynomial is fitted into the distribution of the cross-section bending displacements along the beam, see full calculation algorithm for the case of $i = 3$ and $j = 2$ in Table 5.1. The rotations are then calculated as values of the second derivative of the fitted

polynomial. The cross-section twist deformations κ_t corresponding to the beam twist rate, are calculated as values of the first derivative of the j^{th} order polynomial fitted into the twist angle distribution. The selection of the polynomial orders i and j is discussed below.

Table 5.1: Algorithm for calculation of cross-section deformations.

1.	$k_{mn} = \{x_{mn}, z_m, \Delta y_{mn}\}$	- bending displacement field
	$n = 1..N; m = 1..M$	
2.	$\Delta y_m = tw_m \cdot x + bd_{0m}$	- linear fit within cross-section CS_m
	tw_m	- twist of CS_m
	bd_{0m}	- bending displacement of CS_m at $x = 0$
3.	$bd_m = \Delta y_m(x')$	- bending displacement of CS_m at x'
	$p_m = \{z_m, bd_m\}, \quad m = 1..M$	- bending displacement distribution
	$q_m = \{z_m, tw_m\}, \quad m = 1..M$	- twist distribution
4.	$bd(z) = a_3z^3 + a_2z^2 + a_1z + a_0$	- polynomial fit to p_m
5.	$\kappa_b = -\frac{d^2bd(z)}{dz^2} = -6a_3z - 2a_2$	- bending rotations
6.	$tw(z) = a_2z^2 + a_1z + a_0$	- polynomial fit to q_m
7.	$\kappa_t = \frac{dtw(z)}{dz} = 2a_2z + a_1$	- twist rates

The process of derivative calculation is well known for its low robustness due to excessive sensitivity to noise in the input data. Therefore, the results for the cross-sectional bending rotations and twist rates can be significantly affected by the noise generated by a measurement system. It is especially important for DIC measurements obtained during experiments, as the results of FE analyses are considered as free of noise. To reduce the effect of the DIC measurement noise and thus to improve the robustness of the developed calculation algorithm, it is necessary to extract data from as many cross-sections as possible ($M = M_{max}$), so that the subsequent polynomial fittings has a noise filtering effect.

Consider application of the bend-twist coupling analysis method to a clamped uniform beam. If all the beam cross-sections are free to warp (St. Venant's torsion), then the application of bending and torsion moments to the tip of such a beam will lead to a uniform cross-section bending rotations ($\kappa_b = const$), and to a constant twist rate ($\kappa_t = const$). Therefore it is enough to use the second order polynomial

($i = 2$) for the bending displacement distribution and the first order polynomial ($j = 1$) for the twist angle distribution to correctly represent the beam behavior.

If warping is not allowed at the clamped end of the beam (Vlasov's torsion), then polynomials of higher orders are required to represent the effect of warping restrain (clamped beams) typically expressed as increase in torsional stiffness. Higher order polynomials are also required in case of non-uniform beams where the cross-sectional stiffness and coupling parameters change along the beam length.

To capture the variations of bending and torsional stiffnesses and bend-twist coupling coefficient along the beam, appropriate polynomial orders have to be chosen. However, one has to bear in mind, that higher polynomial orders are more sensitive to the measurement noise. For this reason, no recommendation can be given by the author on the polynomial order selection, and instead, the order should chosen by trying several polynomials and selecting the ones that generate the results least affected by the measurement noise but at the same time allowing to capture the expected stiffness and coupling parameters variations.

5.4 Verification against results of BECAS and VABS

The results of the developed bend-twist coupling analysis method for a case of a solid composite beam are compared to the results of the Beam Cross-Sectional Analysis Software (BECAS) tool developed recently by Blasques and Lazarov (2011) and the Variational Asymptotic Beam Sectional Analysis (VABS) by Yu et al. (2002). 2D FE cross-sectional analysis is performed in these two tools to calculate a 6x6 stiffness matrix of the studied beam cross-section according to Timoshenko beam formulation.

A case of solid beam of square cross-section made of orthotropic material is considered for the comparison. The beam dimensions are 100 mm x 100 mm x 1000 mm, see Fig. 5.2. The beam is manufactured as a single layer orthotropic material with fibers placed in XZ plane. The fibers are oriented so that the angle between them and the longitudinal Z-axis of the beam is 22.5°. Mechanical properties of the orthotropic material are given in Table 5.2.

A FE model of the composite beam is developed in ANSYS using layered volume finite elements SOLID185. The meshing parameters are determined by the dimensions of the solid finite elements, which are chosen as 5mm x 5mm in the beam

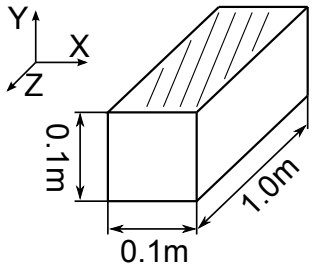

Figure 5.2: Solid beam geometry.

Parameter	Value
E_{11}	480 Pa
$E_{22} = E_{33}$	120 Pa
$G_{12} = G_{13}$	60 Pa
G_{23}	50 Pa
$\nu_{12} = \nu_{13}$	0.19
ν_{23}	0.26

Table 5.2: Orthotropic material parameters. Principal fiber direction is 1-1.

cross-section plane and 25mm along the beam. Hence, there are 20x20 elements in each cross-section and 40 elements along the beam. According to the developed bend-twist coupling analysis method, two load cases, bending and torsion, are applied to the beam fixed at one end (warping deformations are allowed in the entire beam) and 3D displacement field of the beam top side lying in the XZ plane is extracted in form of 41 cross-sections based on the displacements of the appropriate nodes in the beam deformed state. The extracted displacement field is processed according to the calculation algorithm of the bend-twist coupling analysis with the cross-section bending displacements determined at the cross-section mid-width position.

To demonstrate the effect of using higher polynomial orders in the analysis method, two polynomial orders were selected for the calculations: $i = 3$ and $j = 2$ (see Table 5.1) - as one of the minimal orders; and $i = 12$ and $j = 11$ - as some of the higher orders for this particular case. The variations of bending stiffness EI, torsional stiffness GJ and bend-twist coupling coefficients K_b and K_t along the beam are hence calculated using the two order sets.

The results of both BECAS and VABS tools were generated by Blasques and Lazarov (2011) in form of 6x6 cross-section stiffness matrix. Only the results of the BECAS tool are used in the present verification, as no significant differences between the results of the two tools were found.

The distributions of EI, GJ and K_b with K_t along the beam calculated by the bend-twist coupling analysis method are respectively compared to the three components K_{44}, K_{66} and K_{46} of the 6x6 cross-section stiffness matrix calculated by BECAS, see plots in Fig.5.3. The parameters calculated by BECAS are given as solid horizontal lines in the center of the plot, representing constant value along the beam length. The results of the simplified analysis are given as distributions of the calculated parameters along the beam. The ranges of the plots are limited by $\pm 10\%$ of the BECAS value, for convenience.

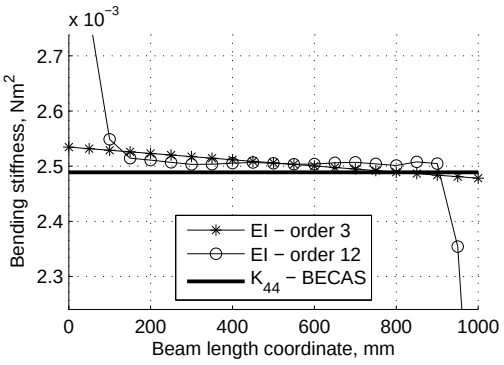

(a) Bending stiffness EI vs K_{44}

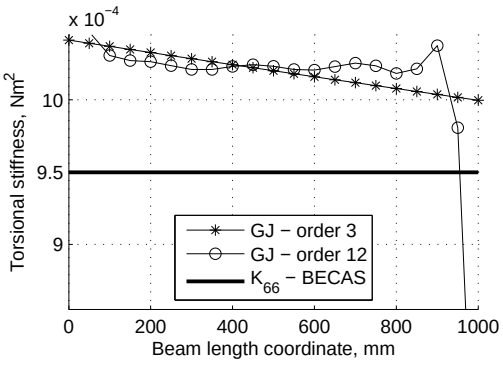

(b) Torsional stiffness GJ vs K_{66}

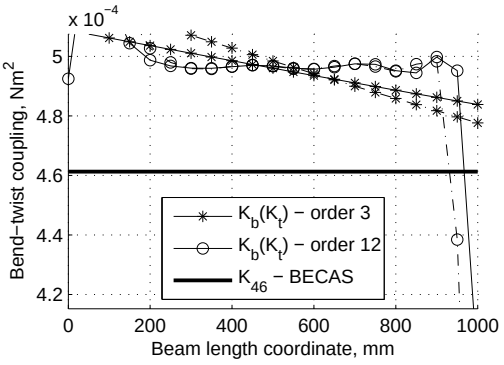

(c) Bend-twist coupling K_b and K_t vs K_{46}

Figure 5.3: Bending stiffness EI (a), torsional stiffness GJ (b) and bend-twist coupling coefficients K_b and K_t (c) versus the results of BECAS tool K_{44}, K_{66} and K_{46}.

The boundary conditions for the examined beam are set so that the out-of-plane

cross-section deformations (warping) are allowed within the entire beam, but the in-plane deformations of the fixed cross-section are restrained. Therefore, the boundary condition effect is expected to appear in form of slight increase in beam bending stiffness and torsion stiffness at the fixed beam end. Indeed, as seen in the graphs, the results of the bend-twist coupling analysis method demonstrate higher bending and torsional stiffness at the clamped beam end. However, the low order polynomial fit approach can capture and demonstrate this effect only roughly in form of a stable stiffness growth along the entire beam, while the higher order approach can do it in a more distinct manner.

The results of bending and torsional stiffness, generated by using the 12^{th} order polynomial fit demonstrate more stable distributions along the beam length with more pronounced edge effects than the lower order approach. But this happens only in case when FE analysis results, free from any measurement noise, are processed. If the measurements are of low quality, the higher order approach will react to the measurement noise as if it is caused by variation of the beam properties and thus, will generate unrealistic results. Therefore, the low order polynomial approach suits for processing the experimentally obtained measurements, while the high order approach can be recommended only for processing of FE analysis results.

Nevertheless, no significant deviations between the results generated by using the 3^{rd} and the 12^{th} order polynomials are found. The deviations of 3-4% between them are accounted as acceptable. The differences between the bend-twist coupling coefficients K_b and K_t are found low for both considered polynomial orders, which is due to absense of the noise in the FE model output.

Finally, as it can be seen in the given plots, the result of bending stiffness calculated by the simplified analysis method are very close to the results of BECAS with deviation of ca. 1%. Torsional stiffness and bend-twist coupling coefficient deviate from the BECAS results about 7-8%. Apart from the sensitivity problems of the bend-twist coupling analysis method, the errors are caused by the simplified problem formulation used in the developed method, which does not allow beam deformation modes other than bending and twist. Yet for such simple analysis method the up-to-8% errors are still accounted as of moderate levels.

5.5 Analysis of numerical and experimental results for composite beams

The bend-twist coupling analysis method is applied to the results of the experiments and the FE analyses on composite beams performed in Chapter 4.

First, an optimal set of orders for polynomial fit into the bending displacements and twist angles along the beams is to be selected. For this reason, three polynomial order sets are chosen for evaluation. With the notation of Table 5.1, the polynomial sets are the following: $i = 3$ with $j = 2$, $i = 4$ with $j = 3$ and $i = 5$ with $j = 4$. The first set corresponds to the lowest polynomial orders capable of capturing variations of the cross-section parameters (EI, GJ, K_b and K_t) along the beam, while the two other are representatives of higher order approaches. For convenience, the sets are named according to the order i used for polynomial fitting into the bending displacement distribution.

The experimental results obtained by DIC measurements on one of the 0° UD box-beams are selected for the present benchmark case. According to the recommendation for application of the bend-twist coupling analysis method (see Section 5.3.1), to decrease sensitivity of the polynomial derivation procedures to DIC measurement noise, the most dense measurement data possible are extracted from DIC measurements on the beam surface. Hence, 71 cross-sections are extracted along the measured beam surface, starting from position 10 mm and up to position 700 mm from the clamped beam end, with a step of 10 mm. The distributions of bending and torsional stiffnesses as well as of bend-twist coupling coefficient calculated by using the bend-twist coupling analysis method are presented in Fig. 5.4.

In all three graphs pronounced end effects are clearly present for the results of higher order approaches with polynomial order sets with $i = 4$ and $i = 5$. Obviously, this happens due to the sensitivity of the derivation procedures to the measurement noise. The results of the 3^{rd} order polynomial fitting approach are exposed to much lower fluctuations, but they still demonstrate good agreement between the global trends in variations of the cross-sectional parameters and the results of the higher order approaches. Therefore, the 3^{rd} order polynomial is selected for representation of the bending displacement distribution and the 2^{rd} order polynomial is selected for the representation of the twist angle distributionswhen the simple bend-twist coupling analysis method is applied.

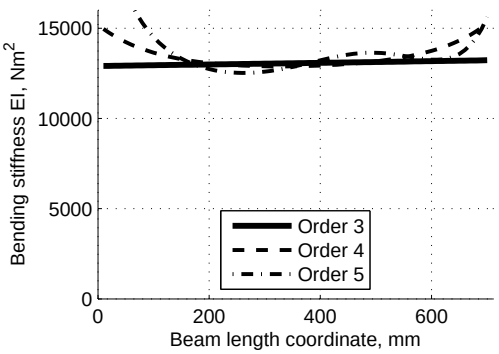

(a) Bending stiffness EI

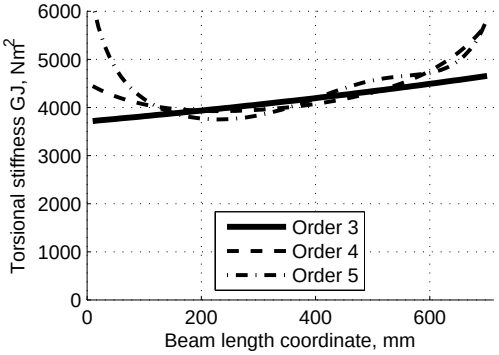

(b) Torsional stiffness GJ

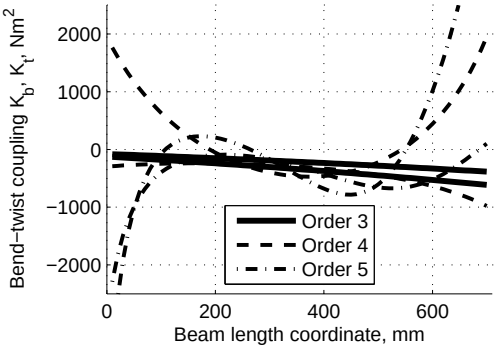

(c) Bend-twist coupling K_b, K_t

Figure 5.4: Distributions of bending stiffness EI (a), torsional stiffness GJ (b) and bend-twist coupling coefficient $K_{b,t}$ (c) calculated for three polynomial order sets for 0° UD box-beam.

5.5.1 Analysis of experimental results on composite beams

Similarly to the benchmark test above, to decrease sensitivity of the bend-twist coupling analysis to measurement noise, 70 cross-sections are extracted along the beams from the full-scale DIC measurements performed during experiments. The cross-sections are at positions starting from $X = 10$ mm from the clamped beam end, and up to $X = 700$ mm from the clamped beam end, with a step of 10 mm.

The results of the bend-twist coupling analysis on the box-beams are presented in Fig. 5.5 and on the I-beams are presented in Fig. 5.6. The bend-twist coupling results are given in form of coefficients α_b and α_t calculated according to (5.8) and (5.12) using two different coupling induced beam responses: beam bending in torsion and beam twist in bending.

The results of bending stiffness for box- and I-beams (Fig. 5.5(a) and 5.6(a)) are rather close to constant with only minor variations which are accounted as insignificant. In contrast, torsional stiffnesses for all the beam configurations (Fig. 5.5(b) and 5.6(b)) are noticeably varying. For the box-beams a stable trend towards increase in bending stiffness at the free end is found, which could be either due to boundary conditions, imposed by the load clamps mounted at the beam tip, or due to strong end effects – the exact reason is unclear. Torsional stiffness of the I-beams is clearly affected by the warping restrains at the clamped end which is expressed as stiffening at the beam clamped end.

Due to very low magnitudes of the beam bending displacements induced by bend-twist coupling in torsion load case (see e.g. Fig. 4.29(a)), the coupling coefficients α_b for all the beams (see Fig. 5.5(c) and 5.5(d)) are subject to variations and therefore are of low reliability. The distributions of bend-twist coupling coefficient α_t are much more stable, see Fig. 5.5(d) and 5.6(d). However, due to the problem of parasitic torque induced by the load application system in bending load case (see details in Section 4.6.2) the magnitudes of beam twist responses and hence the magnitudes of the coupling coefficients α_t are reduced. The reduction is more severe for the I-beams due to their much lower torsional stiffnesses.

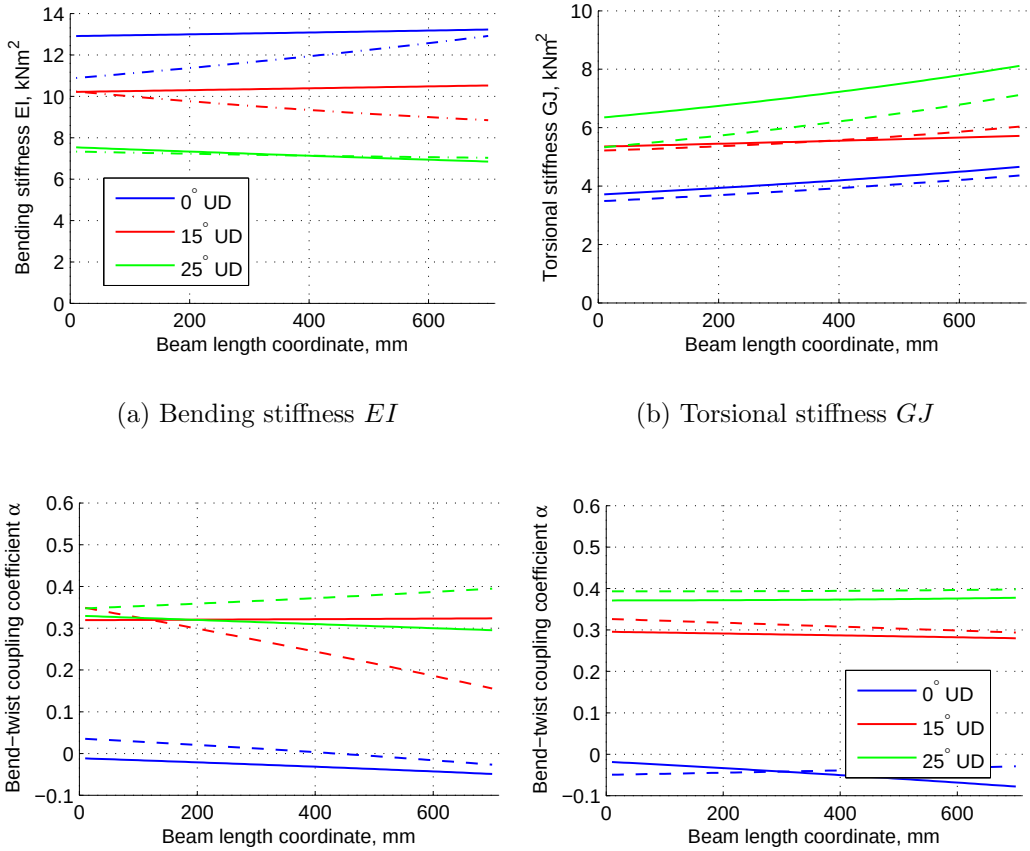

(a) Bending stiffness EI

(b) Torsional stiffness GJ

(c) Bend-twist coupling α_b

(d) Bend-twist coupling α_t

Figure 5.5: Bending stiffness EI (a), torsional stiffness GJ (b) and bend-twist coupling coefficients $\alpha_{b,t}$ (c, d) calculated for UD box-beams based on the experimental DIC measurements. Solid and dashed lines represent two different specimens for the same beam configuration.

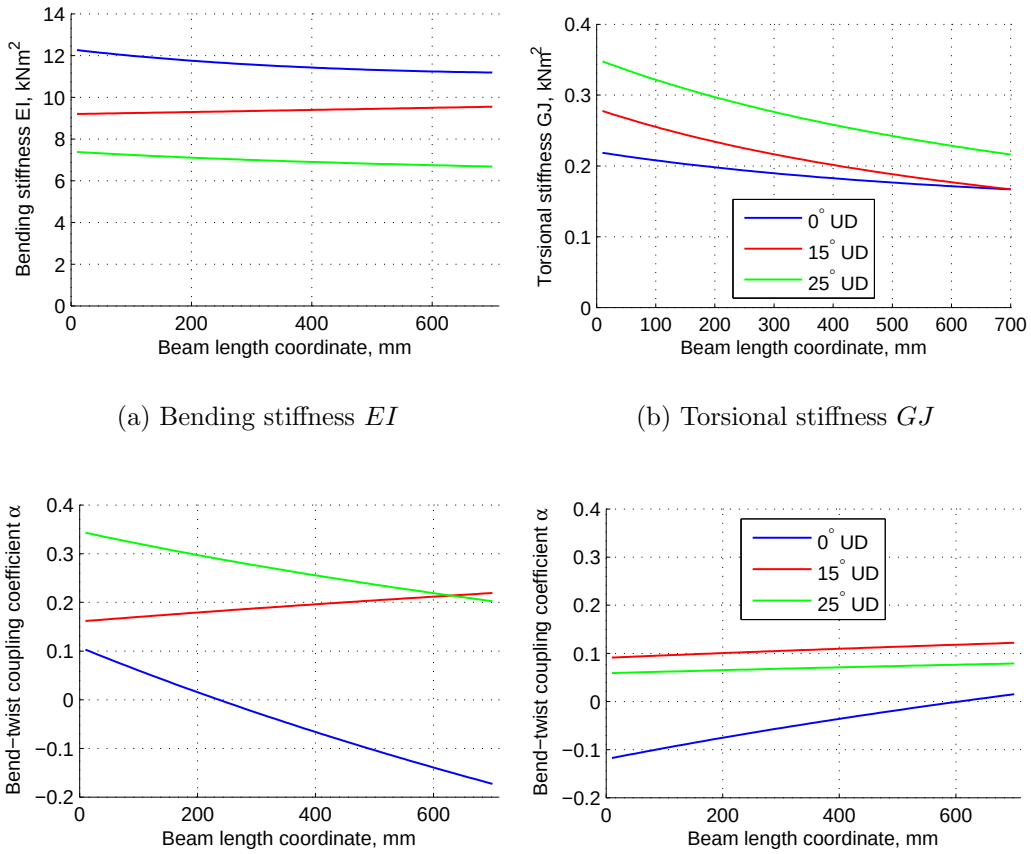

(a) Bending stiffness EI

(b) Torsional stiffness GJ

(c) Bend-twist coupling α_b

(d) Bend-twist coupling α_t

Figure 5.6: Bending stiffness EI (a), torsional stiffness GJ (b) and bend-twist coupling coefficients $\alpha_{b,t}$ (c, d) calculated for UD I-beams based on the experimental DIC measurements. Solid and dashed lines represent two different specimens for the same beam configuration.

5.5.2 Analysis of numerical results on composite beams

The distributions of bending stiffness, torsion stiffness and bend-twist coupling coefficient along the composite beams obtained by application of the simple bend-twist coupling analysis method to the results of FE analyses on the composite beams are presented in Figs. 5.7 and 5.8.

Due absence of measurement noise, steady distributions are obtained when the results of FE analyses on the beams are processed. All the FE models, apart from the ones built of shell elements with nodal offsets, demonstrate results very close to the experiments. The problem of incorrect prediction of beam torsional stiffnesses by the FE models built of shell elements with nodal offsets is clearly seen in Fig. 5.7(b). This configuration of shell elements leads to underprediction of the box-beam torsional stiffness at the beam tip and its strong overprediction at the beam clamped end.

One should notice that for the I-beams, there is no such problem with prediction of the beam torsional stiffness, see Fig. 5.8(b). The results of the FE models built of shell elements with nodal offsets are very similar to the results of the two other models and also to the experimental values. However, the numerically predicted torsional stiffness of the I-beams is not dependent on the UD fiber direction variation in the beam flanges as much as the torsional stiffness obtained experimentally does.

The bend-twist coupling coefficients α_t predicted by the numerical models for all the beam configurations are higher than the experimentally obtained values due to the mentioned problem of parasitic torque induced by the load application system. The effect of the issue is found to be more pronounced for the I-beams, for which the experimentally obtained coefficients are as much as 1.5 times below the numerical values.

Summarizing the results of this section, the developed simple bend-twist coupling analysis method proved to be an good tool for the purpose of pure experimental study on the effects of bend-twist coupling in composite beams and for validation of detailed 3D FE models of composite beams. The method provided estimations of beam bending and torsional stiffnesses as well as bend-twist coupling coefficient with possibility to analyze the distributions of these parameters along the beam length. The effects of warping restrains can also be studied using the results generated by the analysis method.

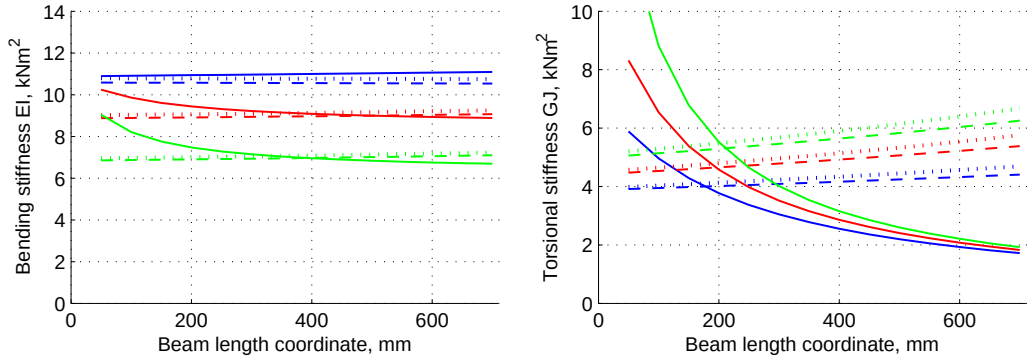

(a) Bending stiffness EI (b) Torsional stiffness GJ

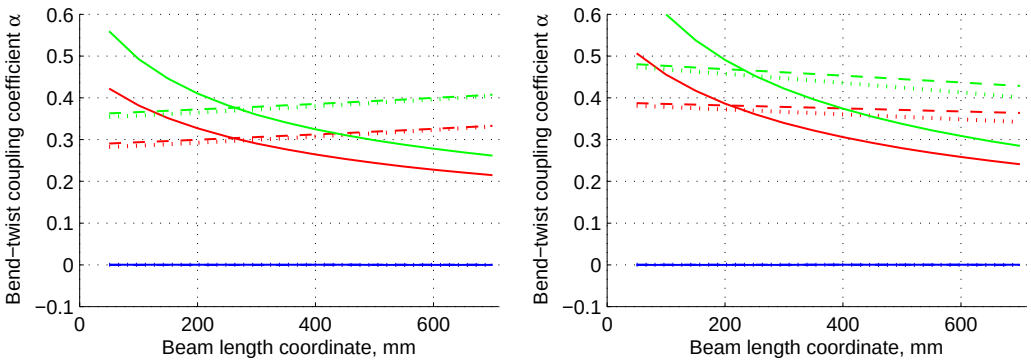

(c) Bend-twist coupling α_b (d) Bend-twist coupling α_t

Figure 5.7: Bending stiffness EI (a), torsional stiffness GJ (b) and bend-twist coupling coefficients $\alpha_{b,t}$ (c, d) calculated for UD box-beams based on the results of FE models. Blue color corresponds to 0° UD beams, red – 15° UD beams and green – 25° UD beams. Solid lines represent the results of FE models with shell elements with nodal offsets, dashed – FE models with shell elements without nodal offsets, and dotted – FE models with continuum shell elements.

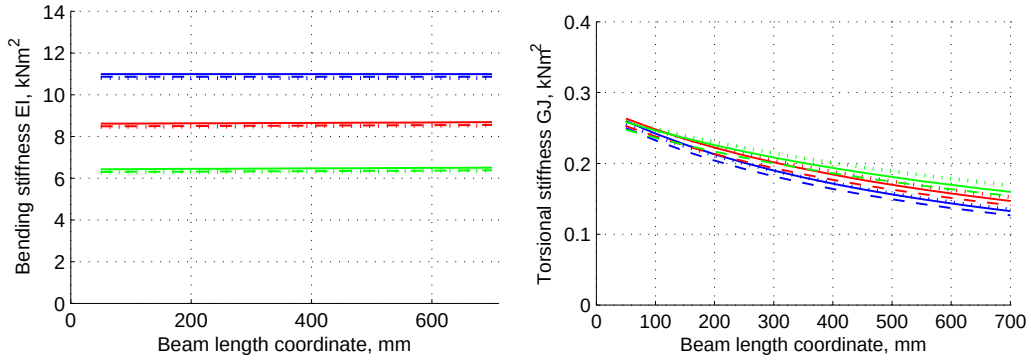

(a) Bending stiffness EI

(b) Torsional stiffness GJ

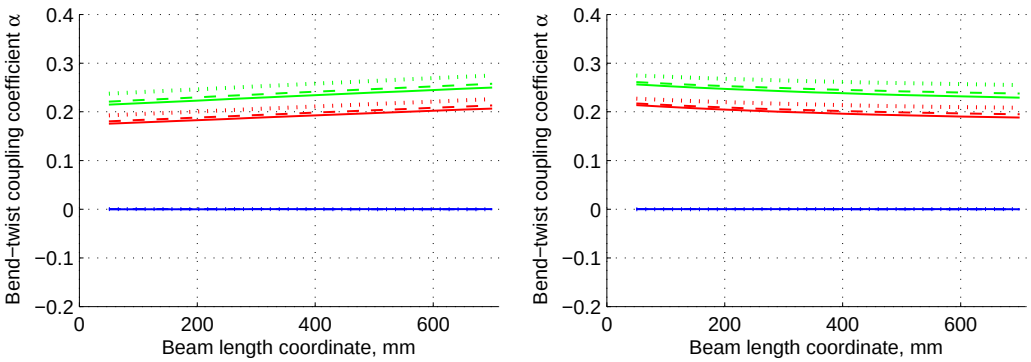

(c) Bend-twist coupling α_b

(d) Bend-twist coupling α_t

Figure 5.8: Bending stiffness EI (a), torsional stiffness GJ (b) and bend-twist coupling coefficients $\alpha_{b,t}$ (c, d) calculated for UD I-beams based on the results of FE models. Blue color corresponds to 0° UD beams, red – 15° UD beams and green – 25° UD beams. Solid lines represent the results of FE models with shell elements with nodal offsets, dashed – FE models with shell elements without nodal offsets, and dotted – FE models with continuum shell elements.

5.6 Analysis of FE results for wind turbine blade section

For evaluation of mechanical properties of the wind turbine blade section studied in Chapters 2 and 3, the simple bend-twist coupling analysis method is applied to the results of the 3D FE models of the original and modified blade sections built using shell elements with nodal offsets to the blade outer surface. Yet, it is known that utilization of the the nodal offset technique in shell elements leads to inaccurate prediction of blade torsional rigidity, these FE models are used for generation of the blade section response in bending and torsion load cases as the other blade section FE models considered in the study, are not fully available (only results of the models in a number of load cases are provided), so that is was not possible to extract more dense data on the blade section deformation for successful application of the bend-twist coupling analysis method.

Bending load case is implemented in addition to the blade section torsion considered during the previous numerical study on the blade section presented in Chapter 3. Bending moment of 5.0 kNm is applied to the free end of the blade section by means of rigid connections between all the nodes at the loaded cross-section – the same way as it is done in the torsion load case, see Section 3.6.1 and Fig. 3.13 for details.

The responses of the FE models of the original and modified blade sections are extracted from 21 cross-sections along the blade section length. Several polynomial orders are selected for representation of the blade bending displacement distributions to account for possible end effects in the results of the developed bend-twist coupling analysis method. The orders are chosen from the 3^{rd}, as the lowest one, and up to the 6^{th}. For the twist angle distributions along the blade section, polynomials of one order lower than for the bending displacements are used, as only the first order derivative is required for calculation of the blade section twist rates.

The results of the developed simple bend-twist coupling analysis method are compared to the results of the BPE method developed by Malcolm and Laird (2003). The BPE method implies interpretation of the blade section by six uniform beam elements and recovery of 6x6 cross-section stiffness matrices for these beams according to Timoshenko beam formulation. The BPE method was applied to the blade section FE model built of combination of shell and solid elements by Berring and Knudsen (2006). The results of both bend-twist coupling analysis method and the BPE method for the original blade section are shown in Fig. 5.9, and for the modified blade section – in Fig. 5.10.

is used for building of full Timoshenko 6x6 stiffness matrices for cross-sections along a wind turbine blade without using a beam theory. Instead, a detailed 3D FE model of the blade built of shell finite elements was developed and the stiffness matrices were calculated based on the response of the blade model to six unique load cases.

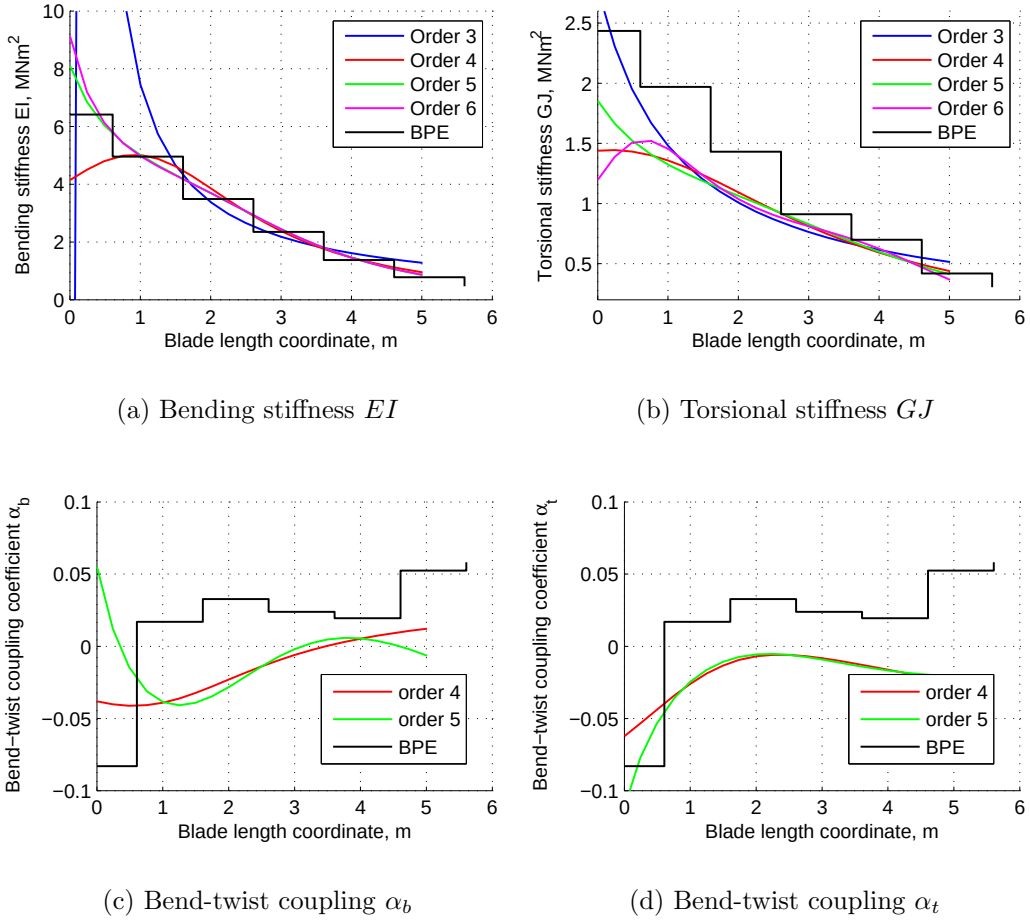

(a) Bending stiffness EI

(b) Torsional stiffness GJ

(c) Bend-twist coupling α_b

(d) Bend-twist coupling α_t

Figure 5.9: Bending stiffness EI (a), torsional stiffness GJ (b) and bend-twist coupling coefficients $\alpha_{b,t}$ (c, d) calculated based on results of FE model of the original blade section using simple bend-twist coupling analysis method and BPE method.

End effects are presented in the results of the simple bend-twist coupling analysis method for all considered polynomial order sets. The part of the blade section close to the clamped end, ca. 1 m long, is significantly affected by the end effects, and thus is taken out of further considerations. The results of bending stiffness

for the blade section root part corresponding to the 3^{rd} order polynomial fitting (Fig. 5.9(a) and 5.10(a)) possess noticeable deviations from the results of higher order approaches. It is therefore most likely that the 3^{rd} order polynomial cannot correctly represent the blade section bending displacement distribution. Apart from these issues, no significant deviations between the results of all polynomial orders are observed, and thus, the 4^{th} order polynomial is believed enough to represent the blade section bending response.

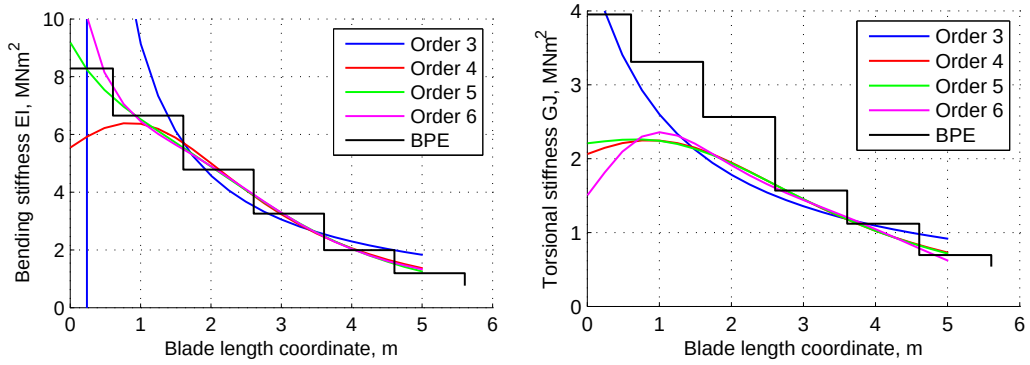

(a) Bending stiffness EI

(b) Torsional stiffness GJ

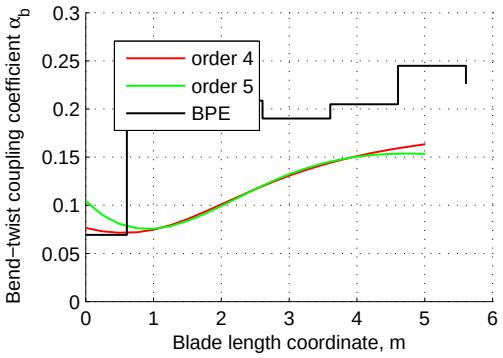

(c) Bend-twist coupling α_b

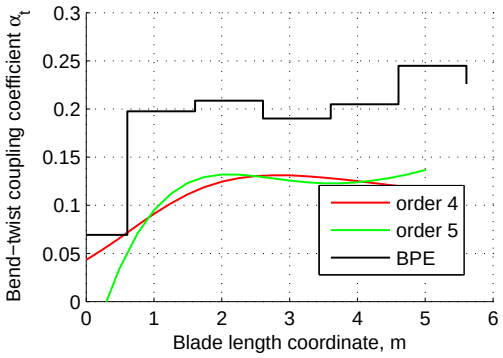

(d) Bend-twist coupling α_t

Figure 5.10: Bending stiffness EI (a), torsional stiffness GJ (b) and bend-twist coupling coefficients $\alpha_{b,t}$ (c, d) calculated based on results of FE model of the modified blade section using simple bend-twist coupling analysis method and BPE method.

The results of the bending stiffnesses obtained by the developed simple bend-twist coupling analysis method are in general very close to the results of the BPE

method for both original and modified blade sections, see Figs. 5.9 and 5.10. As expected, the blade section torsional stiffnesses obtained by the FE model built of shell elements with nodal offsets, are underpredicted, which corresponds well to the results of BPE method. Due to the problem of the torsional stiffness underprediction, large discrepancies are present in the results of coupling coefficients obtained by the two methods, see Figs. 5.9(c), 5.9(d), 5.10(c) and 5.10(d).

In spite of the accuracy problems of the FE models built of shell elements with nodal offsets, it is possible to study the variations of such parameters as bending stiffness, torsional stiffness and bend-twist coupling coefficient along the original and modified blade sections using the simple bend-twist coupling analysis method. The method provided evaluation of these parameters for both blade section configurations and demonstrated increased bend-twist coupling in the modified blade section in comparison to its original configuration.

5.7 Conclusions

A simple bend-twist coupling analysis method for experimental and numerical investigations on the bend-twist coupling effects in beam structures was developed. A 2x2 cross-section stiffness matrix formulation that incorporates only bending stiffness, torsional stiffness and bend-twist coupling coefficient was adopted in the method. As a result, responses of a beam in two load cases, bending and torsion were required for estimation of the cross-section stiffness matrix elements.

The analysis method can be applied to the results from detailed 3D FE analysis of a composite beam, where the beam structure is modeled using shell and/or solid finite elements. One of the advantages of the method is that it can also be applied to the experimentally obtained beam response, e.g. using DIC measurements techniques. Additionally, the bend-twist coupling analysis method can be used for study of local effects in beams such as e.g. increase in torsional stiffness due to warping restrains at the clamped beam end, or to study the variations of bending and torsion stiffnesses as well as bend-twist coupling coefficient in beams of non-uniform cross-sections.

The simple bend-twist coupling analysis method was verified against the results of two cross-sectional analysis codes, BECAS and VABS, in a benchmark problem of a bend-twist coupled solid composite beam. The beam bending stiffness calculated by the simplified analysis method agreed very well with the results of both codes (ca. 1% error). The results of torsional stiffness and bend-twist coupling coefficient

were predicted less accurately but were still in good agreement (ca. 7-8% error) with the results of the two codes. The observed error was accounted as acceptable for such simplified cross-section stiffness matrix formulation adopted in the bend-twist coupling analysis method.

The simple bend-twist coupling analysis method was applied to the results of the experiments performed recently on a set of composite beams. Variations of bending and torsional stiffnesses and bend-twist coupling along the beams of different configurations were evaluated, which facilitated more detailed analysis on the bend-twist coupling effects and the effects of warping restrains in the composite beams. Additionally, the bend-twist coupling analysis method was applied to the results of detailed FE models of composite beams. The utilization of the method aided more detailed validation of the numerical models against the experimental results, e.g. the problem of underprediction of beam torsional stiffness by FE models built of shell elements with nodal offsets was clearly demonstrated. The maximum bend-twist coupling coefficients for the considered beams were found as 0.3-0.4 for the 25° UD Box-beam configuration and 0.2-0.3 for the 25° UD I-beam configuration.

The analysis was also applied to the numerical results of the original and the modified wind turbine blade sections generated by FE models built of shell elements with nodal offsets. The acquired results were compared to the results of the BPE method applied to the results of FE models of the same blade section but built of combination of shell and solid finite elements. Very close prediction of blade bending stiffness variations by both methods and underprediction of the blade section torsional stiffness by the FE models built of shell elements with nodal offsets were demonstrated. Finally, noticeable bend-twist coupling in the modified configuration of the blade section was observed.

Chapter 6

Implementation of bend-twist coupling in a wind turbine blade

6.1 Introduction

A numerical study on implementation of the bend-twist coupling effects in a commercial wind turbine blade structure and on practical limits of the coupling magnitudes in the blade is presented in this chapter. The variations of the blade bending and torsional stiffnesses that occur due to the implementation of the bend-twist coupling are also of particular interest of this study.

Bend-twist coupling coefficient α defined by Lobitz and Veers (1998) is presently adopted as a measure of the bend-twist coupling in beam structures. Using this parameter, information on the bend-twist coupling magnitudes in beam structures of different geometries (from simple plates to real wind turbine blades) available in the literature is gathered to present a general trend of the coupling magnitudes in composite beam structures.

Further, the implementation of the bend-twist coupling in a commercial blade section is studied. It is done by selecting four cross-sections along the blade length and developing highly detailed finite element models of long uniform beams of the selected cross-sections. The evaluation of the beam bending and torsional stiffnesses and bend-twist coupling coefficient is done by using a simple bend-twist coupling analysis method. The alterations of these three parameters due to modifications of the cross-section layups are therefore studied.

Two approaches to modify the baseline wind turbine blade structure for implementation of the bend-twist coupled blade design are considered. The first approach concerns fiber biasing in all uni-directional layers of the blade load carrying spar flanges, so that all fibers of the UD layers are equally directed away from the blade longitudinal axis. The second approach concerns substituting the original glass-fiber reinforced plastics material of the spar flange UD layers with much stiffer carbon-fiber reinforced plastics material which at the same time possess higher orthotropy.

6.2 Bend-twist coupling in beam structures

The main objective of the present study is to investigate the levels of the bend-twist coupling (BTC) feasible to achieve in modern wind turbine blades. To review the methods of the BTC implementation, provide expectations regarding possible magnitudes of the coupling in composite beam structures of different configurations and to gather information about the amount of BTC feasible to achieve in beam structures, a literature survey is carried out.

To compare the results of different studies available in the literature, the coupling coefficient α defined by Lobitz and Veers (1998) and closely examined in the previous chapter is chosen as a unique measure of bend-twist coupling. The coefficient is defined through a simplified relation between the generalized bending and torsion moments M and T applied to a cross-section and its bending and twist responses κ_b and κ_t, by mean of bending stiffness EI, torsional stiffness GJ and bend-twist coupling coefficient K:

$$\begin{bmatrix} M \\ T \end{bmatrix} = \begin{bmatrix} EI & -K \\ -K & GJ \end{bmatrix} \begin{bmatrix} \kappa_b \\ \kappa_t \end{bmatrix} \tag{6.1}$$

The normalized bend-twist coupling coefficient is then defined as:

$$\alpha = \frac{K}{\sqrt{EIGJ}}; \qquad -1 < \alpha < 1 \tag{6.2}$$

First, Ong and Tsai (1999) analytically evaluated bend-twist coupling for a simple laminate plate using the classical laminate theory. It was found that maximal value of the BTC coefficient highly depends on material properties and is 0.5 for a glass-fiber reinforced plastic (GFRP) and of 0.8 for a carbon fiber reinforced

plastic (CFRP). Further, a composite D-spar configuration was investigated during the same study, where the results of numerical parametric study revealed the BTC coefficient values of ca. 0.4 for GFRP and ca. 0.6 for CFRP and hybrid (GFRP+CFPR) D-spars.

In the experimental investigations performed on composite beams (see Chapter 5), where the BTC effects were implemented by variation of fiber directions in UD materials of the beam flanges, the BTC coefficient appeared highest as ca. 0.3-0.4 for the 25° UD Box-beam configuration while it was of ca. 0.2-0.3 for the 25° UD I-beam configuration.

Locke and Hidalgo (2002) studied BTC in double-cell tapered wind turbine spar using single-cell thin-walled anisotropic beam theory extended to two-cell beams. The spar was made of two single-cell spars, manufactured using braided hybrid (56% carbon and 44% glass fibers) composite meaterial. The results for the BTC coefficient of the spar structure varyied from 0.23 at the tip to 0.45 at the root of the spar.

Kooijman (1996) performed analytical evaluation of BTC magnitudes in thin-walled single-cell monocoque composite blades. The blades were considered to be of several airfoils (18-21% in thickness), and made from UD carbon laminates, biased cross-ply carbon laminates or biased cross-ply hybrid (carbon+glass) laminates. When the BTC coefficients are calculated based on the results of his work, their maximal values generally vary from 0.6 to 0.7.

Griffin (2002) used FE models built of shell elements without nodal offsets for a parametric study on a 35m test wind turbine blade representative of commercial blades. The cross-section designs for a 30% thick airfoil were modeled as 20m cantilevered beams of constant cross-sections. The evaluated BTC coupling coefficients were in the range of 0.14-0.31 for a number of considered material sets. For the final design of the blade the BTC coefficient was varying from 0.19 at the 8.75m radial position to 0.27 at the 26.25m radial position.

Lin and Lai (2010) in their study on the bend-twist elastic coupling adopted a combined analytical and finite element beam model and evaluated the bend-twist coupling coefficient along the 5 meter wind turbine blade developed by Habali and Saleh (2000). The blade spar was made of either GFRP, CFRP or hybrid (GFRP+CFRP) materials. The coupling was introduced into the blade structure by changing the fiber orientation to 20° off-axis orientation in a part of the blade spar. The obtained values for the bend-twist coupling coefficient were found to be of 0.2 for the GFRP blade configuration, 0.3 for the CFRP configuration, and up

to 0.55 for the hybrid configuration. Maximal values in each of the configurations were registered for the airfoil thicknesses of 22%-25%.

Recently Capellaro and Kuhn (2010) used the variational asymptotical beam sectional analysis (VABS) by Yu et al. (2002) to evaluate BTC coefficient in the same simple composite plates as Ong and Tsai (1999) and achieved generally the same results for both GFRP and CFRP plates. For a simple composite section more representative of a blade section, value of 0.12 for the glass-fiber configuration and 0.17 for the carbon-fiber configuration were obtained. Further, several cross-sections of a 63 meter blade of the 5 MW Upwind wind turbine were studied. With the UD material changed from GFRP to CFRP, maximal BTC coefficient was achieved as 0.25 for the cross-section at radial position 44 meter with 18% thickness airfoil. For the cross-section at radial position of 60 meter with same airfoil, maximum BTC coefficient value was significantly less – only about 0.1. For the cross-section at a radial position of 11 meter with much thicker airfoil the maximal BTC coupling was of 0.15.

Summarizing the results of the literature review, it is clear that value of the BTC coefficient highly depends on the materials used in the structure. Composite materials with higher orthotropy rates, like carbon fiber reinforced plastics in comparison to glass fiber reinforced plastics, provide higher values of the BTC coefficient and can be recommended not only to achieve higher bend-twist coupling magnitudes but also to provide higher bending and torsional stiffnesses of the structures, which are typical requirements for the wind turbine blade designs.

It is observed that maximal values of the BTC coefficient are generally decreasing from simple beam structures, like elongated laminated plates, towards commercial wind turbine blade profiles. An evident reason for that is the complication of the wind turbine blade structure due to a number of design requirements, e.g. required airfoil, minimal bending stiffness, resistance to buckling and so on.

For the case of the blade design with a load carrying spar, the implementation of BTC is often done by redirecting the fibers of the UD layers in the spar flanges, or by redirecting the fibers of the UD and $\pm 45^\circ$ biax materials directly in the outer shell of the blade. The magnitudes of BTC coefficients for the composite structures, representatives of real wind turbine blade designs, are found varying in the range of 0.2 - 0.4 depending on the utilized materials.

6.3 Study on a commercial wind turbine blade structure

To evaluate the magnitudes of BTC that are feasible to achieve in a commercial wind turbine blade structure and to study variations of the blade bending and torsional stiffnesses due to the implementation of BTC, a numerical investigation is presently performed. The original blade section provided by Vestas Wind Systems A/S and considered earlier in the experimental and numerical investigations presented in Chapters 2 and 3 is selected as a baseline wind turbine blade structure for the present study.

The blade section has a load carrying spar along its entire length and represents a tapered and slightly pretwisted non-uniform composite beam. GFRP materials are mainly used in the blade structure. Significant amount of GFRP UD layers are present in the spar flanges, while biax ($\pm 45°$) and triax ($-45°/0°/+45°$) layers of GFRP are extensively used in the blade outer aerodynamic shell. Foam is used as core for sandwich components in both leading and trailing edges and partially in the spar webs.

Two ply drops are present along the blade section length and therefore three representative layups and four cross-section are distinguished, see Fig. 6.1. The differences between the three layups are in the UD GFRP layer thicknesses in the spar flanges due to the mentioned ply drops. Additionally, foam core is present in the spar webs near the blade section root (layup 1). The layups of the spar top flange area are indicated in Fig. 6.2. The four cross-sections selected along the blade section are designated as CS1..CS4. The cross-section shapes are represented by airfoils with 21, 19, 17 and 16% relative thickness accordingly, see Fig. 6.3.

The four following cross-section configurations are considered in the present study: CS1 with layup 1, CS2 with layup 1, CS3 with layup 2 and CS4 with layup 3. To evaluate the BTC magnitudes possible to achieve for these configurations, detailed 3D FE models are developed for long uniform beams of the selected cross-sections. The beam responses to bending and torsion loads are obtained by using FE models. Further, the simple bend-twist coupling analysis method presented in Chapter 5 is applied to the numerical results for evaluation of bending and torsional stiffnesses and BTC coefficients for the four beams of the selected cross-sections.

Two methods to introduce bend-twist coupling into the blade section structure are presently considered. The first method concerns variation of fiber directions in the original UD GFRP material of the load carrying spar flanges within the range of

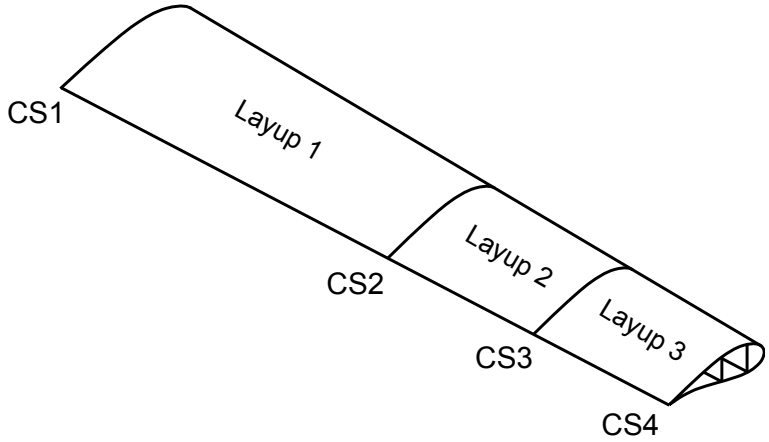

Figure 6.1: Layup arrengement in the blade section with selected cross-sections.

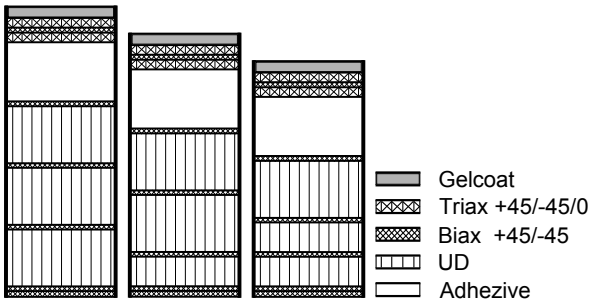

Figure 6.2: Layups at the load carrying spar top flange area. In proportions. From left to right: layup 1, layup 2, layup 3.

$-25.. + 25°$. 5° step is chosen for the fiber direction variation as the one which is believed to be realistic to implement in practice. The load carrying spar layup is kept symmetrical in this case.

Orientating the fibers away from the longitudinal axis in the original layup will inevitably lead to decrease in the blade bending stiffness. This effect was clearly visible on the composite beams studied in Chapter 4. Hence, the second method for the implementation of BTC into the blade section implies substitution of the UD GFRP in the spar flanges by much stiffer UD CFRP material and variation of the carbon fiber directions the same range as in the first method. The substitution of the original GFRP by CFRP is expected to compensate for the losses in the blade bending stiffness due to the fiber biasing and also to generate higher BTC effects due to stronger anisotropy of CFRP. Properties of the GFRP and CFRP materials are given in Table 6.1.

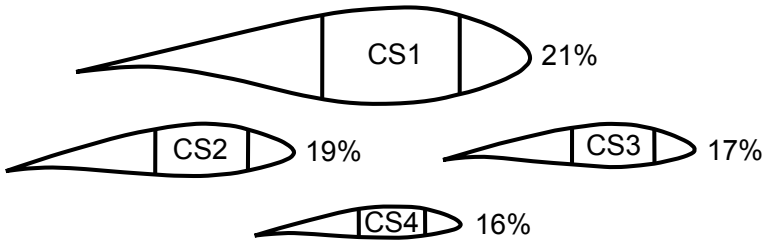

Figure 6.3: Schematic view of the cross-sections selected in the blade section with indicated airfoil thicknesses.

Table 6.1: Mechanical properties of GFRP and CFRP materials.

Parameter	GFRP	CFRP
E_{11}	39.9 GPa	105 GPa
E_{22}	11.6 GPa	6.82 GPa
G_{12}	4.44 GPa	3.32 GPa
ν	0.303	0.280

6.3.1 FE models

Detailed 3D FE models are developed in ANSYS v.11 for uniform beams of each of the four chosen cross-section configurations. To avoid the problem of inaccurate torsional stiffness prediction when nodal offsets are used in shell finite elements (see Laird et al. (2005)), the models are built of layered shell elements SHELL181 without nodal offsets. Note, that no play-drops are presented in the developed models as the modeled beams are uniform, and thus the problem with inaccurate prediction of beam bending stiffness when rigid elements are used to account for the ply-drops along the beam is avoided, see Branner et al. (2007), Chapter 3 for more details.

Meshing parameters for the FE models are taken in accordance to the convergence study performed on the blade section FE models during the earlier numerical investigations (see Chapter 3). Each of the FE models have 100 elements along the beam length and thus the nodal deformation results for 100 cross-sections along the beam can be extracted. The beams are modeled as fully clamped at one end, and loaded at the free end by creating rigid sections (CERIG command in ANSYS) for better load distribution and to avoid large local deformations at the loaded ends. Two load cases, bending and torsion are applied to the models to generate the beam responses required for application of the simple bend-twist coupling analysis method. Magnitudes of the applied moments are carefully chosen for each beam configuration, so that no large deformations ($> 5^\circ$ in bending rotations and $> 5^\circ$

Table 6.2: Moments applied to four beam configurations.

Configuration	Bending moment, kNm	Torque,kNm
CS1 + layup 1	20	20
CS2 + layup 1	5	5
CS3 + layup 2	2.5	2.5
CS4 + layup 3	1	1

in twist) occur in the loaded beams, see Table 6.2.

To exclude the end effects generated by clamped boundary conditions and by the simple bend-twist coupling analysis method, free warping conditions corresponding to Saint Venant's torsion are ensured in the middle part of the beams by increasing the length of the beams to 10 meter.

Discontinuities between the adjacent shell elements inevitably take place in the FE models due to variation of wall thicknesses along the chosen cross-sections and utilization of only mid-thickness nodal positions in the shell finite elements. Placement of shell elements in the case of the 21% thick cross-section configuration is presented in Fig. 6.4(a). Here, the shell elements are placed along the solid lines and the discontinuities are marked by circles. The layup visualization is shown in Fig. 6.4(b). To solve the problem of discontinuities, rigid beam elements MPC184 are used to create rigid connections between the separated adjacent shell elements. Each of the beam cross-sections in all developed FE models containes 20 rigid elements.

6.3.2 Application of BTC analysis method

FE analysis provides the beam responses to bending and torsion. Bending displacement and twist response in bending load case for the beam with 21% thick airfoil cross-section of the original layup is presented in Fig. 6.5. As it is seen in the graph of the beam twist distribution, there are pronounced effects of the clamped boundary condition at the beam root and the effect of rigid section implementation at the beam tip.

Following the recommendations drawn in the previous Chapter 5, where the simple bend-twist coupling analysis method is presented, as the result of FE models are considered free of measurement noise, the end effects in the beam response demonstrated above can be accurately enough represented by simply using high

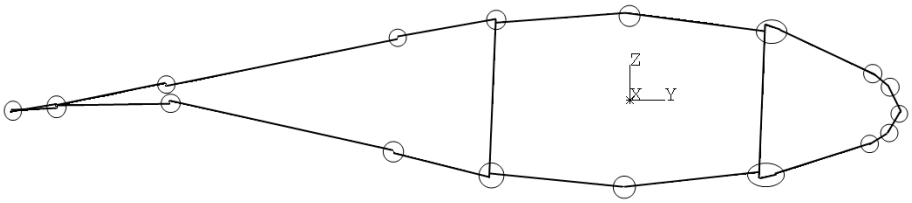

(a) Shell element placement

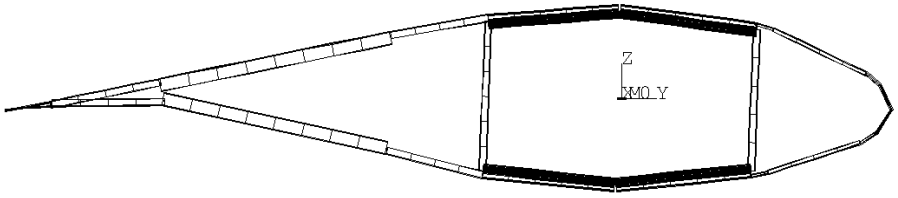

(b) Layup visualization

Figure 6.4: Shell element placement (1) and layup visualization (b) for the FE model of beam with 21% thick airfoil cross-section. Rigid elements are marked by circles.

order polynomials for fitting into the bending displacement and twist angle distributions. Therefore, for 100 cross-sections extracted along the beams, a 40^{th} order polynomial is selected for the beam bending displacement representation and the 39^{th} order polynomial is selected for the beam twist representation.

Edge effects are clearly present in the distributions of bending stiffness, torsional stiffness and bend-twist coupling coefficient, see Fig. 6.6. At the same time, in the middle part of the beam, from position 3.5 m to position 6.5 m, the results are not affected by the edge effects and are constant. Hence, bending and torsional stiffnesses as well as BTC coefficient for the studied beam configuration are determined as average values of their distributions in the range of 3.5 - 6.5 meter. This evaluation procedure is found valid for all the beam configurations and their modifications, considered in the present study.

Thus, by varying the fiber directions in either GFRP or CFRP UD layers of the carrying spar flange for all the four chosen cross-section configurations, and by utilizing the simplified bend-twist coupling analysis method, the variations of bending

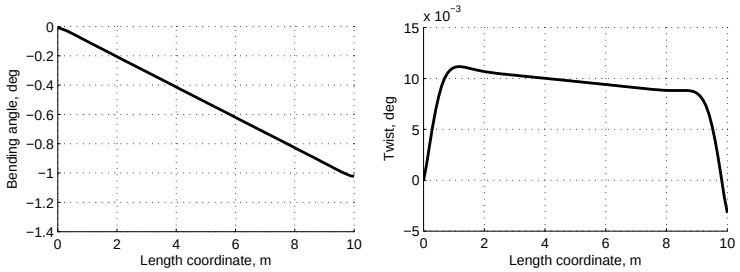

(a) Bending angle (b) Twist

Figure 6.5: End effects in bending angles (a) and twist angles (b) for bending of the beam with 21% thick airfoil section with original layup.

and torsional stiffnesses together with the variations of BTC coefficients are obtained.

6.4 Results and discussion

The results of the simple bend-twist coupling analysis method, applied to the responses of the four beams generated by the developed FE models, are presented in form of bending stiffness EI, torsional stiffness GJ and bend-twist coupling coefficient α as functions of the fiber direction in the GFRP and CFRP UD layers of the load carrying spar flanges. The variations of the stiffnesses are given in per cents to the stiffnesses of the corresponding baseline configurations, that is 0° UD GFRP layers in the load carrying spar flanges. The results for the GFRP spar configurations are shown in Fig. 6.7 and for the CFRP configurations – in Fig. 6.8.

As seen in Fig. 6.7(a), bending stiffnesses of all the four cross-sections decrease with biasing the glass-fibers in the spar flanges from the blade longitudinal axis. The trends are symmetrical with respect to positive and negative fiber directions. Significant drop rates (up to 1.7 per cent per degree) are observed at the fiber angles close to 15°-25° and much lower rates at lower fiber angles. Note, that thinner airfoils possess slightly lower bending stiffness drop rates.

The variations of torsional stiffnesses for the GFRP configurations (see Fig. 6.7(b)) also have clear symmetrical trends with respect to positive and negative fiber directions. In contrast to the bending stiffness variations, torsional stiffnesses

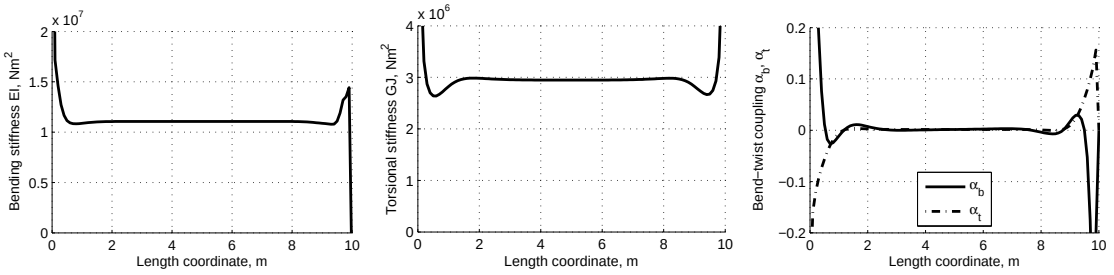

(a) Bending stiffness (b) Torsional stiffness (c) Bend-twist coupling coefficient

Figure 6.6: Distribution of bending stiffness (a), torsional stiffness (b) and bend-twist coupling coefficient (c) along the beam with 21% thick airfoil section with original layup.

tend to grow with the fibers in the UD layers of the spar flanges biasing more from the longitudinal axis. The growth rates are the highest at higher fiber angles and reach 0.6-1.0 per cent per degree. At lower fiber angles, all the torsional stiffness sensitivities approach zero. Notice, that thinner airfoils possess higher sensitivities of the torsional stiffnesses with respect to the fiber directions.

Bend-twist coupling coefficients for the GFRP configurations possess the maximal values of ca. 0.2 for the fibers biased 25° away from the original direction – along the blade pitch axis, see Fig. 6.7(c). The maximal values do not differ significantly among the airfoil thicknesses. Fastest growth rates, up to 14.3e-3 units per degree, are observed at the lowest fiber angles, while lowest rates are observed at the fiber angles near 25° where the coupling coefficients are at their maximums. It is evident that the largest effects of fiber biasing in the UD GFRP layers of the spar flanges take place at the lowest fiber angles, where BTC coefficients are most sensitive and bending stiffnesses are least sensitive to the fiber angle variations.

Similar results are obtained for the cross-section configurations where UD CFRP layers are considered in the spar flanges, see Fig. 6.8. The variations of both stiffnesses in the plots are given with respect to the original GFRP configurations – 0% values correspond to the baseline GFRP configurations. The main differences are in higher bending and torsional stiffnesses due to stiff carbon fibers. Maximal bending stiffness sensitivities are up to 8 per cent per degree at ±10° fiber directions; maximal torsional stiffness sensitivities are up to 2.5 per cent per degree at ±10° fiber directions. Highest bend-twist coupling coefficients of up to 0.4 are achieved at fiber angles of ca. ±20°. Additionally, larger differences are found

between the results for different airfoils – thinner airfoils have higher sensitivities of the coupling coefficients with respect to the fiber direction variation.

The maximal values for the BTC coefficients in the GFRP spar configurations are about 0.2, and the maximal values for the CFRP spar configurations are two times higher, up to 0.4, due to higher level anisotropy of the carbon-fiber material. These results correspond well to the expectations and the results available in literature and thus, they indicate that there are potential practical limits for the bend-twist coupling coefficients in wind turbine blade structures designed with load carrying box-spars made of certain materials.

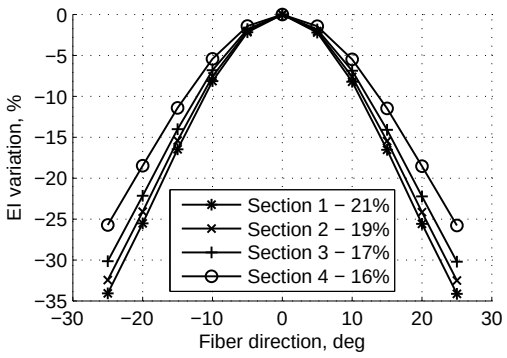

(a) Bending stiffness

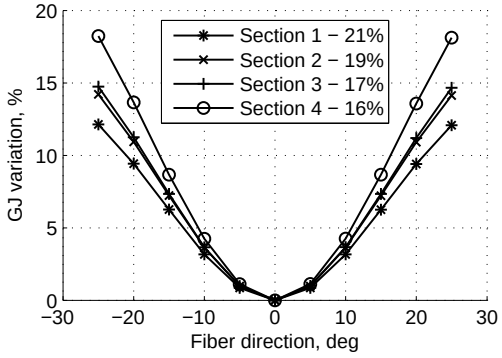

(b) Torsional stiffness

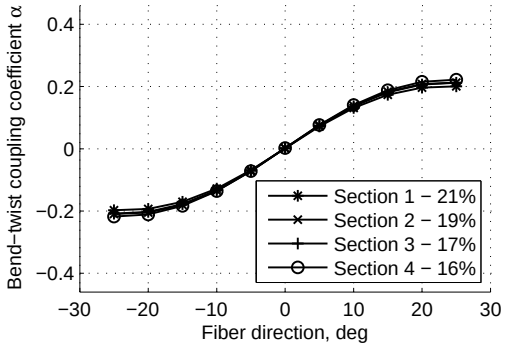

(c) Bend-twist coupling

Figure 6.7: Variation of bending stiffness (a), torsional stiffness (b) and bend-twist coupling (c) for the sections with GFRP UD material in the spar flanges versus variation of the UD fiber direction

The variation of bending stiffness, as one of the most important parameters of

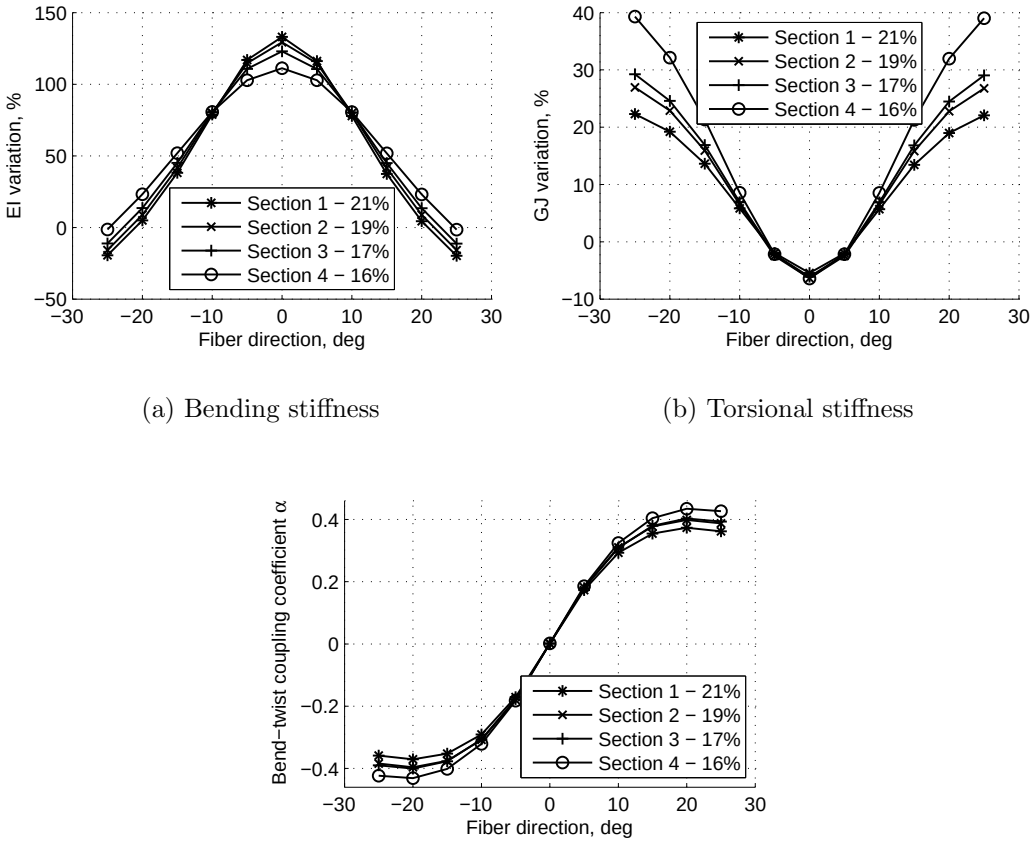

(a) Bending stiffness

(b) Torsional stiffness

(c) Bend-twist coupling

Figure 6.8: Variation of major parameters for the sections with CFRP UD material in the spar flanges versus variation of the UD fiber direction

a wind turbine blade structure due to the fiber biasing in the spar flanges has been demonstrated. CFRP material in almost all the considered fiber direction configurations provide higher bending stiffnesses than the original GFRP material. Thereby, CFRP can be recommended to be used for effective introduction of the BTC into the blade structures. However, a well known trade off here is a much higher price of the carbon-fiber materials. To limit the cost rise due to utilization of more expensive CFRP instead of GFRP, BTC can be implemented only in a part of a blade structure (e.g. in thinner airfoils away from thick blade root, which are found to be more sensitive to the fiber direction variations), similar approach is undertaken by Lin and Lai (2010) and by Berry and Ashwill (2007).

The results of the analysis also demonstrate the sensitivities of BTC coefficients

and bending and torsional stiffnesses with respect to the fiber directions in the spar flanges. This can be used for evaluations of the bend-twist coupling in design of coupled wind turbine blades. For example, in a case with only GFRP considered as a material for the carrying spar, the cost of implementation of BTC in terms of reduction of the blade bending stiffness can be determined. The most effective way of introduction of limited amount of the coupling is seen in using low fiber biasing angles due to minimal reduction of the blade bending stiffness and maximal increase rates for the BTC coefficient at smaller fiber biasing angles.

6.5 Conclusions

In the present study a literature survey on bend-twist coupling magnitudes in composite beam structures was carried out, where it was demonstrated that maximal values of the bend-twist coupling coefficients strongly depend on the material properties and generally decrease from simple beam structures, like elongated laminated plates, towards commercial wind turbine blade profiles.

To investigate the levels of the bend-twist coupling effects feasible to achieve in modern wind turbine blade strucutres, four representative cross-sections of a commercial wind turbine blade were studied by developing highly detailed FE models of long uniform beams of the considered cross-sections. By utilizing the simple bend-twist coupling analysis method, such parameters as bending and torsional stiffnesses as well as bend-twist coupling coefficient were determined as functions of the fiber directions in the UD GFRP or CFRP layers of the load carrying spar flanges and discussed.

The maximal absolute values of the BTC coefficients achieved by modifying the commercial wind turbine blade structure were found to be of 0.2 for the pure GFRP configuration and of 0.4 in case of substitution of the original GFRP UD material in the load carrying spar flanges by CFRP. For the maximal BTC configurations, the fibers in the spar flanges had to be biased from the longitudinal (blade pitch) axis by 25° in the GFRP and by 20° in the CFRP configurations. The obtained results correlated well with the results available in the literature, which lead to a conclusion that there are potential limits for the BTC coefficients practically achieved for the wind turbine blade structures with load carrying box-spars made of certain materials.

The sensitivities of bending stiffness, torsional stiffness and bend-twist coupling coefficient with respect to the fiber directions in the UD layers of the spar flanges

were studied for all the selected cross-section configurations. In general, near-zero sensitivities of bending and torsional stiffnesses and highest sensitivities of BTC coefficient were found at low fiber direction angles. Maximal bending stiffness drop rates were found for all the GFRP cross-section configurations at fiber directions near $15° - 25°$. Maximal torsional stiffness growth rates for all the GFRP configurations were found at the same fiber directions. For the CFRP configurations the highest rates were found at $10°$ fiber direction for both bending and torsional stiffnesses.

It was demonstrated that for optimal introduction of bend-twist coupling to the pure GFRP spar configurations of wind turbine blades, low magnitude fiber biasing can be recommended due to lower bending stiffness drop rates and higher BTC coefficient growth rates at small fiber biasing angles. It was also found that higher coupling coefficients can be generally achieved for the cross-sections of thinner airfoils.

This page is intentionally left blank.

Chapter 7

Conclusions and future work

7.1 Conclusions

The PhD project started with an experimental investigation on the bend-twist coupling effects in a modified commercial wind turbine blade section in **Chapter 2**. The blade section being a non-homogeneous composite beam was found to be a complex problem for a pure experimental study and certain assumptions were adopted to simplify the investigation methods. The bend-twist coupling effects in the blade section modified as an attempt to implement bend-twist coupling in it, were demonstrated as bending deflection of the spar center line with a torsional moment applied at the tip of the clamped blade section.

An advanced hydraulic system was successfully utilized in the experimental investigation to accurately apply all the considered load cases. The blade section response was measured using digital image correlation technique that provided very accurate full 3D displacement measurements over the top surface of the blade section. A DIC data processing method was developed to extract the blade section bending and twist response in form of lengthwise distributions of the blade bending displacements and twist angles. This experimental study provided a good foundation for further experiments performed on composite beams in terms of expertise in load application and the DIC measurement technique.

Development of detailed 3D FE models of modern composite wind turbine blade structures was addressed in **Chapter 3**. Three common approaches for development of detailed 3D FE models of modern wind turbine blades were considered: FE models built of shell elements with nodal offsets, FE models built of shell elements

without nodal offsets (nodes placed at the shell mid-thickness positions) and FE models built of combination of shell and solid elements. The experimental results for the tested commercial wind turbine blade section were used for validation of the developed FE models using all three approaches.

It was demonstrated, that the FE model built of shell elements with nodal offsets was the fastest/cheapest to develop but inaccurately predicted the blade twist response with 20%-30% tip twist errors. The FE model built of shell elements without nodal offsets required more effors in developement due to large amount of rigid elements to be introduced in the shell mid-surface discontinuities, and was inaccurate in prediction of the blade bending response due to rigid elements introduced into the model to represent material ply-drops. The FE model built of combination of shell and solid elements demonstrated the most accurate results, but required non-trivial modifications of the material properties and the mesh to provide connections between the shell and the solid finite elements.

Chapter 4 concerns more detailed investigation carried out on performance of FE models built of shell elements. A set of uniform composite beams of open (I-shaped) and closed (box-shaped) cross-sections with implemented bend-twist coupling of different magnitudes was selected to provide experimental results for validation of the FE models. An advanced setup to test the beams, where loads are applied to the beam specimens by mean of two compact servo-hydraulic actuators and the beam response is measured using two DIC systems. Particular attention was paid to the warping restrain effects in the composite beams.

The results of the study demonstrated very good accuracy of the FE models built of continuum shell elements and the FE models built of shell elements without nodal offsets. Therefore, these two approaches were recommended for development of accurate FE models of composite shell structures with bend-twist coupling effects, such as e.g. coupled wind turbine blades. The FE models built of shell elements with offsets demonstrated very low accuracy in prediction of the box-beam twist responses (up to 100% tip twist errors), but quite high accuracy in case of the open cross-section I-beam configurations. The warping deformations in the composite beams predicted by all the FE models generally well correlated to the warping deformations measured experimentally using a DIC system.

Chapter 5 describes a simple bend-twist coupling analysis method that was developed for investigations on the bend-twist coupling effects in beam structures. A 2x2 cross-section stiffness matrix formulation that incorporates only bending stiffness, torsional stiffness and bend-twist coupling coefficient is adopted in the method. One of the advantages of the method is in possibility to apply it both to the numerical results obtained by developing a detailed FE model of a beam (e.g.

using shell elements) and to the experimental results obtained by DIC measurements performed on a beam specimen in testing.

The results of the developed method were compared to the results of BECAS and VABS beam cross-section analysis tools for a benchmark case of bend-twist coupled solid composite beam. It was demonstrated that the method provides a good evaluation of the beam bending and torsional stiffnesses and the bend-twist coupling coefficient.

Further, the method was applied to the results of the FE analyses performed earlier on a set of composite beams with bend-twist coupling effects. It was as well applied to the experimental data on the composite beams, generated for validation of the developed beam FE models. It was demonstrated, that the method provides a very good visualization of the problem of inaccurate torsion stiffness prediction by the FE models built of shell elements with nodal offsets. The effects of warping restrains in the composite beams of open cross-sections were also clearly observed in form of local variations of the beam torsional stiffnesses. Magnitudes of the bend-twist coupling effects in the composite beams were evaluated using the normalized bend-twist coupling coefficient α introduced in the simple bend-twist coupling analysis method. The coupling magnitudes of 0.3-0.4 were found for the Box-beam configurations and of 0.2-0.3 for the I-beam configurations.

Finally, variations of bending and torsional stiffnesses of the studied earlier wind turbine blade, evaluated by application of the developed method to the results of the blade FE model build of shell elements with nodal offsets were compared to the corresponding variations, obtained by application of the BPE method to the results of the blade FE model built of combination of shell and solid elements. A very good correlation between the variations of the blade bending stiffnesses was obtained. The other parameters demonstrated significant differences due to the accuracy problem of the FE model built of shell elements with nodal offsets.

Chapter 6 started with a literature survey to gather available information on bend-twist coupling magnitudes feasible to achieve in beams of different configurations. It was demonstrated that maximal values of the bend-twist coupling coefficients, in terms of the adopted earlier normalized coefficient, strongly depend on the material properties and generally decrease from simple beam structures, like elongated laminated plates (values of up to 0.8), towards commercial wind turbine blade profiles (0.2-0.4).

Further, the values of maximal bend-twist coupling coefficients for the studied earlier wind turbine blade section were numerically investigated. The investigation was performed by developing of detailed 3D FE models built of shell elements

without nodal offsets for uniform composite beams of four representative cross-sections selected along the original blade section. Magnitudes of the bend-twist coupling coefficients for these cross-sections were evaluated using the developed simple bend-twist coupling analysis method. By varying fiber directions in the UD layers of the blade spar flanges, it was found that the maximal bend-twist coupling coefficient for the original GFRP blade design was of 0.2 with the fibers in the spar flanges biased by 25° away from the blade pitch axis. It was also demonstrated that if the original GFRP UD layers of the spar flanges are substituted for CFRP material, then the maximal bend-twist coupling coefficient rises up to 0.4 when the fibers are biased by 20° away from the blade pitch axis. The obtained results well corresponded to the data gathered during the literature survey. This lead to a conclusion that there might be potential limits for the bend-twist coupling coefficients for wind turbine blade structures, and the magnitudes of the limits strongly depend on the materials used in the structures.

Additionally, the variations of bending and torsional stiffnesses caused by implementation of the bend-twist coupling were obtained by using the developed simple bend-twist coupling analysis method. It is beleived that these results can be used for a preliminary design of future large bend-twist coupled wind turbine blades.

7.2 Future work

There are several things that seem worthy for the author to be performed as a continuation of the present study:

- It is of high interest to use the presently developed simple bend-twist coupling analysis for experimental evaluation of the distribution of bending and torsional stiffnesses as well as the bend-twist coupling coefficient along the modified wind turbine blade section closely studied in the present project. To do that, bending load case is to be applied to the blade section and its deformation is to be measured using a DIC system. The obtained experimental results can be used for additional validation of the blade section FE models, the same way as it was done for the composite beams.
- According to the results of the experiments on composite beams, there was a problem with a parasitic torque applied in bending load case due to shortcomings of the present load application method. Thus, it is of particular interest to perform a new set of bending tests on the same composite beams using an improved load application method, which would ensure absence of the parasitic torque.

- A new test setup can be proposed for a new set of static experiments on composite beams. The main goals of the new test setup would be to provide a better control on warping restrains at the beam clamped end (allowing either fully restrained or free warping conditions) and possibility for testing considerably longer beams to reduce the effect of boundary conditions. This can be done by designing an advanced beam clamping rig, and using a system of cables and dead weights as a load application system, thus no testing machine and hydraulics would be nececcary. Using the same measurement and data processing methods one would be able to provide a clear experimental evidence of the warping restrains and accurate evaluation of its effect in form of variation of beam torsional stiffness.

- The simple bend-twist coupling analysis method can be improved by including a third deformation mode into its formulations. It can be e.g. beam extension or beam bending in the second principal direction. This would require application of a third load case (tension or bending in the second principal direction accordingly) to the studied beam specimen or its FE model. Yet, it is believed, that the coupling between the two original deformation modes and the added one would typically be weak, the improvement would allow to evaluate an additional beam property such as extensional stiffness, or the bending stiffness in the second principal direction.

- It is also of high interest to try to extract additional deformation modes for cross-sections of thin walled beams from the DIC measurements. The extra modes can be, for instance, transverse shear deformations. This would allow to improve the simple bend-twist coupling analysis method even further by including shear deformation modes into the cross-section stiffness matrix formulation, and thus to come closer to the more general Timoshenko beam formulation.

This page is intentionally left blank.

References

Berring, P., Branner, K., Berggreen, C. and Knudsen, H. (2007), Torsional performance of wind turbine blades part I: experimental investigation, in *Proceedings of the 16th International Conference on Composite Materials, ICCM-16 - "A Giant Step Towards Environmental Awareness: From Green Composites to Aerospace", July, 2007*, Kyoto, Japan.

Berring, P. and Knudsen, H. (2006), *Torsional Performance of Large Wind Turbine Blades - Experimental and Numerical Analysis*, Master's thesis, Department of Mechanical Engineering, Technical University of Denmark.

Berry, D. and Ashwill, T. (2007), Design of 9-Meter Carbon-Fiberglass Prototype Blades: CX-100 and TX-100, Technical Report SAND2007-0201, Sandia National Laboratories, Albuquerque, NM.

Blasques, J. P. and Lazarov, B. (2011), BECAS - A beam cross-section analysis tool for anisotropic and inhomogeneous sections of arbitrary geometry. RISØ-R 1785, Technical report, Risø National Lab, Technical University of Denmark.

Branner, K., Berring, P., Berggreen, C. and Knudsen, H. (2007), Torsional performance of wind turbine blades part II: numerical validation, in *Proceedings of the 16th International Conference on Composite Materials, ICCM-16 - "A Giant Step Towards Environmental Awareness: From Green Composites to Aerospace", July, 2007*, Kyoto, Japan.

Brøndsted, P., Lilholt, H. and Lystrup, A. (2005), Composite meaterials for wind power turbine blades, *Annual Review of Materials Research*, 35(1):505–538.

Buhl, J., Marshall, L. and Manjock, A. (2006), A comparison of wind turbine aeroelastic codes used for certification, *Collection of Technical Papers - 44th AIAA Aerospace Sciences Meeting*, 13:9456–9469.

Burton, T. (2011), *Wind energy handbook*, John Wiley & Sons, 2nd edition, ISBN 0470699752.

Capellaro, M. and Kuhn, M. (2010), Boundaries of bend twist coupling, in *Proceedings of TORQUE 2010: The Science of Making Torque from Wind, June 28-30, 2010*, Crete, Greece.

Chandra, R. and Chopra, I. (1991), Experimental and theoretical analysis of composite I-beams with elastic couplings, *AIAA Journal*, 29(12):2197–2206.

Chandra, R. and Chopra, I. (1992), Structural response of composite beams and blades with elastic couplings, *Composites Engineering*, 2(5-7):347–374.

Chandra, R., Stemple, A. D. and Chopra, I. (1990), Thin-walled composite beams under bending, torsional, and extensional loads, *Aircraft*, 27(7):619–626.

Choi, I. and Horgan, C. O. (1977), Saint-Venant's principle and end effects in anisotropic elasticity, *Jouranl of Applied Mechanics*, 44(3):424–430.

Dimitrov, N. (2008), *Methods for Analysing Torsion Stifness of Wind Turbine Blades*, Master's thesis, Department of Mechanical Engineering, Technical University of Denmark.

DNV/Risø(2002), *Guidelines for design of wind turbines*, Det Norske Veritas (DNV) and Risø National Laboratory Wind Energy Department, ISBN 8755028705.

Dufort, L., Grediac, M. and Surrel, Y. (2001), Experimental evidence of the cross-section warping in short composite beams under three point bending, *Composite Structures*, 51(1):37–47.

Fedorov, V. A., Dimitrov, N., Berggreen, C., Krenk, S., Branner, K. and Berring, P. (2009), Investigation of structural behavior due to bend-twist couplings in wind turbine blades, in *Proceedings of the 17th International Conference of Composite Materials (ICCM), July, 27-30, 2009*, Edinburgh, UK.

de Goeij, W. C., van Tooren, M. J. L. and Beukers, A. (1999), Implementation of bending-torsion coupling in the design of a wind-turbine rotor-blade, *Applied Energy*, 63(3):191–207.

GOM (2008), *ARAMIS User Manual - Software, ARAMIS v6.1*, GOM mbH, Braunschweig, Germany.

Greenhalgh, E. S. and Pastore, C. M. (1993), A continuous-fiber composite wing Box-beam exhibiting twist-bend coupling, *Composites Engineering*, 3(7-8):691–697.

Griffin, D. (2002), Evaluation of Design Concepts for Adaptive Wind Turbine Blades, Technical Report SAND2002-2424, Sandia National Laboratories, Albuquerque, NM.

GWEC (2011), GWEC - Global Wind 2010 Report, Technical report, Global Wind Energy Council, Brussels, Belgium.

Habali, S. M. and Saleh, I. A. (2000), Local design, testing and manufacturing of small mixed airfoil wind turbine blades of glass fiber reinforced plastics. Part I: Design of the blade and root, *Energy Conversion and Management*, 41(3):249–280.

Hansen, M. H. (2007), Aeroelastic instability problems for wind turbines, *Wind Energy*, 10(6):551577.

Hansen, M. O. L. (2008), *Aerodynamics of wind turbines*, Earthscan, 2nd edition, ISBN 1844074382.

Hodges, D. H. (2006), *Nonlinear Composite Beam Theory*, American Institute of Aeronautics and Astronautics.

Jones, R. M. (1999), *Mechanics Of Composite Materials, Second Edition*, Taylor & Francis, ISBN 156032712X.

Jung, S. N., Nagaraj, V. T. and I., C. (1999), Assessment of composite rotor blade modeling techniques, *Journal of The Americal Helicopter Society*, 44(3):188–205.

Kooijman, H. J. T. (1996), Bending-Torsion Coupling of a Wind Turbine Rotor Blade, Technical Report ECN-I–96-060, Netherlands Energy Research Foundation ECN, Petten.

Kosmatka, J. B. (1994), General behavior and shear center location of prismatic anisotropic beams via power series, *International Journal of Solids and Structures*, 31(3):417–439.

Laird, D. L., Montoya, F. C. and Malcolm, D. J. (2005), Finite element modeling of wind turbine blades, in *Proceedings of the AIAA/ASME Wind Energy Symposium, 10–13 January 2005*, pp. 9–17, Reno, Nevada.

Lee, A. T. and Flay, R. G. J. (2000), Compliant blades for passive power control of wind turbines, *Wind Engineering*, 24(1):3–11.

Lin, H. J. and Lai, W. M. (2010), A study of elastic coupling to the wind turbine blade by combined analytical and finite element beam model, *Journal of Composite Materials*, 44(23):2643–2665.

Lobitz, D. W. (2004), Aeroelastic stability predictions for a MW-sized blade, *Wind Energy*, 7(3):211–224.

Lobitz, D. W. and Veers, P. S. (1998), Aeroelastic behavior of twist-coupled HAWT blades, in *Proceedings of the AIAA/ASME Wind Energy Symposium, 12–15 January 1998*, Reno, Nevada.

Lobitz, D. W. and Veers, P. S. (2003), Load mitigation with bending/twist-coupled blades on rotors using modern control strategies, *Wind Energy*, 6(2):105–117.

Lobitz, D. W., Veers, P. S., Eisler, G. R., Laino, D. J., Migliore, P. G. and Bir, G. (2001), The Use of Twist-Coupled Blades to Enchance the Performance of Horizontal Axis Wind Turbines, Technical Report SAND2001-1003, Sandia National Laboratories, Albuquerque, NM.

Lobitz, D. W., Veers, P. S. and Migliore, P. G. (1996), Enhanced performance of HAWTs using adaptive blades, in *Proceedings of the Wind Energy 96, ASME Wind Energy Symposium, Jan. 29 - Feb. 2, 1996*, Houston.

Locke, J. and Hidalgo, I. C. (2002), The Implementation of Braided Composite Materials in the Design of a Bend-Twist Coupled Blade, Technical Report SAND2002-2425, Sandia National Laboratories, Albuquerque, NM.

Malcolm, D. J. and Laird, D. L. (2003), Modeling of blades as equivalent beams for aeroelastic analysis, in *Proceedings of the AIAA/ASME Wind Energy Symposium, 6–9 January 2003*, pp. 293–303, Reno, Nevada.

Malcolm, D. J. and Laird, D. L. (2005), Identification and use of blade physical properties, in *Proceedings of the AIAA/ASME Wind Energy Symposium, 10–13 January 2005*, pp. 330–347, Reno, Nevada.

Malcolm, D. J. and Laird, D. L. (2007), Extraction of equivalent beam properties from blade models, *Wind Energy*, 10(2):135–157.

Ong, C. H. and Tsai, S. W. (1999), Design, Manufacture and Testing of a Bend-Twist D-Spar, Technical Report SAND99-1324, Sandia National Laboratories, Albuquerque, NM.

Pollock, G. D., Zak, A. R., Hilton, H. H. and Ahmad, M. F. (1995), Shear center for elastic thin-walled composite beams, *Structural Engineering and Mechanics*, 3(1):91–103.

Rasmussen, F., Hansen, M. H., Thomsen, K., Larsen, T. J., Bertagnolio, F., Johansen, J., Madsen, H. A., Bak, C. and Hansen, A. M. (2003), Present Status of Aeroelasticity of Wind Turbines, *Wind Energy*, 6(3):213–228, ISSN 10954244, 10991824.

Schepers, J. G., Heidra, J., Thomsen, K., Larsen, T. J., Foussekis, D., Smith, R. R., Kraan, I., Visser, B., Oye, S., Ganander, H., Carlen, I., Belessis, M., Voutsinas, S. and Drost, L. (2001), Verification of european wind turbine design codes, in *Proceedings of the European Wind Energy Conference*, Copenhagen, Denmark.

Song, O. and Librescu, L. (1993), Free vibrations of anisotropic composite thin-walled beams of closed cross-section contour, *Journal of Sound and Vibration*, 167(1):129–147.

Vlasov, V. Z. (1961), *Thin-walled elastic beams*, Springfield, Va. : National Technical Information Service, 2nd edition.

Volovoi, V. V., Hodges, D. H., Cesnik, C. E. S. and Popescu, B. (2001), Assessment of beam modeling methods for rotor blade applications, *Mathematical and Computer Modelling*, 33(10-11):1099–1112, ISSN 08957177, 18729479.

WWEA (2012), World Market recovers and sets a new record: 42 GW of new capacity in 2011, total at 239 GW, `http://www.wwindea.org/home/index.php?option=com_content&task=view&id=345&Itemid=43`, [Online; accessed 25-March-2012].

Yu, W., Hodges, D. H., Volovoi, V. and Cesnik, C. E. S. (2002), On Timoshenko-like modeling of initially curved and twisted composite beams, *International Journal of Solids and Structures*, 39(19):5101–5121.

Zenkert, D. and Battley, M. (2006), *Foundations of fibre composites / notes for the course: Composite lightweight structures*, Technical University of Denmark, 2nd edition.

This page is intentionally left blank.

Appendix A

Vestas blade section

According to the agreement with Vestas Wind Systems A/S the content of this appendix is available only for censors.

This page is intentionally left blank.

Appendix B

Configuration of composite beams

Geometry and material properties for composite beams are presented below.

$L =$ 765 mm - Working beam length

$W =$ 100 mm - Beam width

$H =$ 40 mm - Beam height

$L_0 =$ 970 mm - Total beam length

$L_{bc} =$ 100 mm - Length of the clamped part

$L_{arm} =$ 170 mm - Distance between the clamps on the beam

$W_{sw} =$ 30 mm - Width of the shear web flange

$T_{fl} =$ 3.5 mm - Flange thickness

$T_{sw} =$ 2.5 mm - Shear web thickness

$T_{ad} =$ 1.5 mm - Adhesive layer thickness

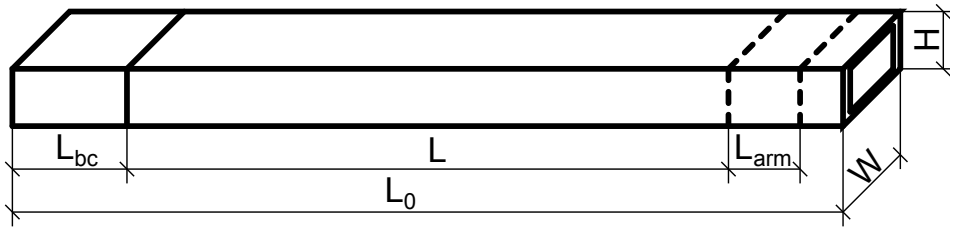

Figure B.1: General view of composite beam

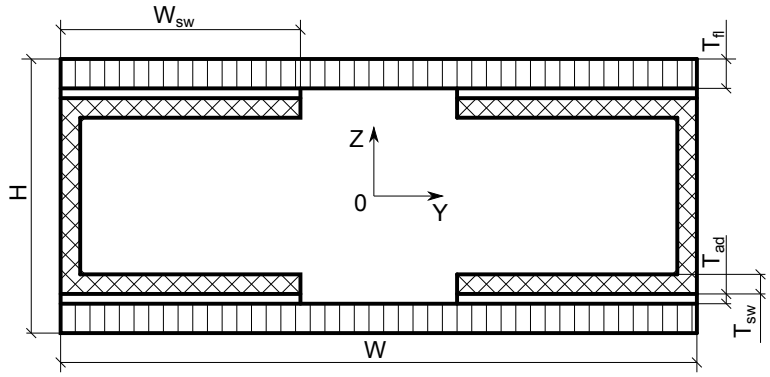

Figure B.2: Geometry of box cross-section

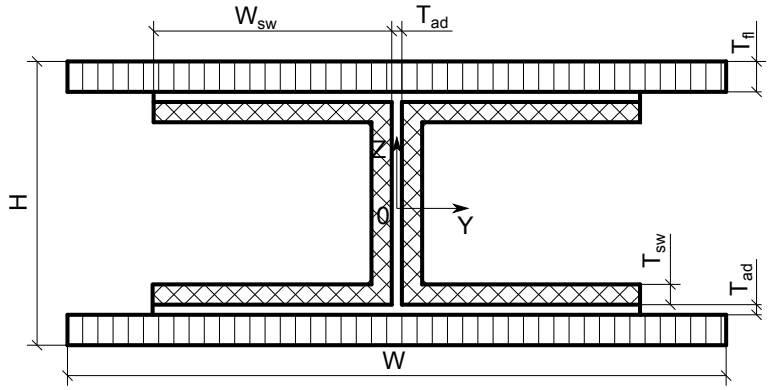

Figure B.3: Geometry of I cross-section

Appendix C

Material data for composite beams

A series of material tests are perfomed for determination of the material data for the composite beams. The following elastic constants are obtained:

- E-modulus of unidirectional GFRP material in the fiber direction
- E-modulus of biax GFRP material
- In-plane shear modulus of unidirectional GFRP material
- In-plane shear modulus of biax GFRP material

For E-modulus determination, two coupons of each material are tested, see Figure C.1. The tests are carried out on a 100kN Instron testing machine. One strain gage aligned with longitudinal axis is aplied on each specimen for strain measurements. The measured strains and forces, applied to the specimens are recorded with a rate of 1 reading per second during loading. Only the initial linear responses of the specimens are used for the E-modulus calculations. The test configuration is chosen to be as close as possible to the ASTM standard D3039 with only few deviations from it, mainly related to the coupon geometries. The coupons are cut out of leftovers after the beam length adjustments, and therefore are of short length.

For shear modulus determination, a number of coupons are tested (see Figure C.2). The tests were carried out on a 100kN MTS testing maching using the Isopescu

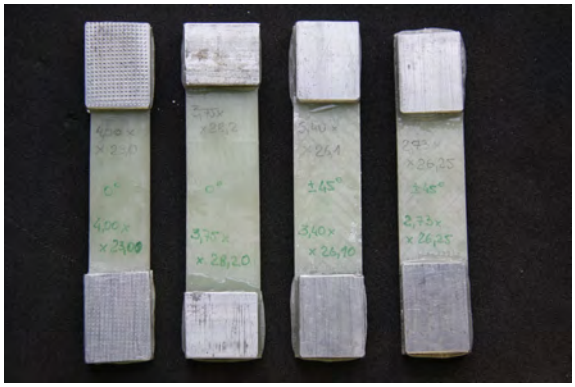

Figure C.1: Coupons for E-modulus material tests.

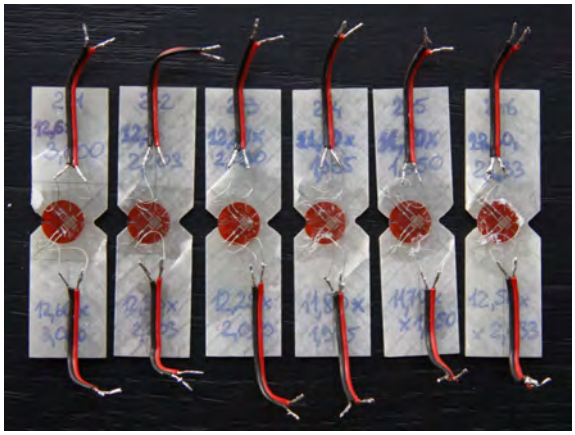

Figure C.2: Coupons for G-modulus material tests

test rig. Two strain gauges directed $+45°$ and $-45°$ with respect to the coupon longitudinal axis are appliedonto each of the tested coupons. The measured strains and forces, applied to the specimens are recorded with a rate of 1 record per second while the specimens being loaded. Only the initial linear responses of the specimens are used for the shear modulus calculations. The test configuration is chosen to be as close as possible to the ASTM standard D5379 with only small deviations from it mainly related to coupon geometries. The results of the material tests for each coupon, as well as the calculated average parameters are listed in Table C.1.

Several attemts to obtain E-modulus for the GFRP material in matrix principal direction are undertaken with rather doubtful success due to very low strength and high brittleness of the tested material in the matrix direction. Therefore E-modulus for the UD laminate in matrix direction is taken as 8.00 GPa according to the average value of the GFRP materials provided by the manufacturer.

	Test #	E_{11}, GPa	E_{11AVG}, GPa	G_{12}, GPa	G_{12AVG}, GPa
UD	1	42.410	42.680	5.900	4.960
	2	42.950		4.010	
Biax	1	9.710	9.220	10.030	10.500
	2	8.730		10.950	
	3	NA		10.090	
	4	NA		10.300	
	6	NA		11.110	

Table C.1: Results of material tests for GFRP materials of composite beams.

Parameter	UD flange	Biax	Adhezive
E_{11}, GPa	42.68	9.22	4.56
E_{22}, GPa	8.00	9.22	-
E_{33}, GPa	8.00	7.00	-
G_{12}, GPa	4.96	10.50	-
G_{13}, GPa	4.96	10.50	-
G_{23}, GPa	3.00	5.00	-
ν_{12}	0.26	0.26	0.3
ν_{13}	0.26	0.26	-
ν_{23}	0.26	0.26	-

Table C.2: Material properties used in FE models of composite beams

The rest of the material data (such as Poisson's ratios, out-of-plane Young's modulus E_{33} and other) are not determined by mean of material tests. Instead, these constants are taken from the datasheet provided by the material supplier. The material data used in the FE models are gathered in Table C.2.